Title	Measurement of the γ-decay Probability of the Hoyle State Using the Combination of Si Detector and ROSPHERE
Author(s)	坂梨，公亮
Citation	大阪大学，2025，博士論文
Version Type	VoR
URL	https://doi.org/10.18910/101906
rights	
Note	

Measurement of the γ-decay Probability of the Hoyle State Using the Combination of Si Detector and ROSPHERE

Kosuke Sakanashi

January 23, 2025

Contents

Abstract

The triple-alpha reaction is one of the most important processes in the nucleosynthesis. In this reaction, an α particle is captured by the 2α resonance of ^{8}Be, and form a 3α cluster state with weakly bound α particles. Most of the 3α resonance states decay to three α particles, but a tiny fraction of them decays to the ground state in ^{12}C via radiative processes of γ decay or $e^{+}e^{-}$ pair emission. Therefore, the γ-decay probability is an important parameter that directly determines the amount of ^{12}C produced in the nucleosynthesis. Several measurements of γ-decay probability were performed by 1976, and the γ-decay probability $\Gamma_{\gamma}/\Gamma = 4.09(10) \times 10^{-4}$ [1] from the Hoyle state has been widely accepted.

Recently, a striking result of the radiative decay-decay probability of the Hoyle state was reported from a measurement of the two γ rays from the cascade decay of the Hoyle state. The new value of $\Gamma_{\gamma}/\Gamma = 6.2(6) \times 10^{-4}$ [2] is 50% higher than the literature value in Ref. [1]. Most of the old data were taken by measuring ^{12}C nuclei surviving after the radiative decay of the Hoyle state. The authors of Ref. [2] claimed that such measurement might not be appropriate and the discrepancy between the new and old results should be due to the different experimental methods. In order to solve this puzzle, it is necessary to measure surviving ^{12}C nuclei and γ rays at the same time.

The aim of this research is to solve the recently reported discrepancy in the γ-decay probability of the Hoyle state. In this study, we conducted the first experiment combining the ^{12}C-detection method and the γ-detection method. We populated the Hoyle state in ^{12}C by the α+^{12}C scattering using an α particle beam at $E_{\text{beam}} = 25$ MeV at the tandem accelerator facility of Horia Hulubei National Institute for R&D in Physics and Nuclear Engineering, Romania (IFIN-HH), and emitted charged particles were detected by a

DSSD and γ rays by the ROSPHERE detector array [**?**]. This method enabled the $\alpha+^{12}\mathrm{C}+\gamma$ triple-coincidence measurement, and successfully determined the γ-decay probability of the Hoyle state as $\Gamma_\gamma/\Gamma = 4.00(27)\times10^{-4}$.

Various measurement have been employed to solve the puzzle of the γ-decay probability of the Hoyle state [3–7], and all these studies excepted Ref. [4] yielded results consistent with the previous literature value adapted in Ref. [1], but contradicts the new value by Kibedi *et al.* [2]. Moreover, our measurement using a novel approach also yielded results supporting the previous literature value. Therefore, we concluded that the puzzle on the γ-decay probability of the Hoyle state is now finally solved, and the previous literature value can be reliably used in the study of nucleosynthesis in the universe.

Chapter 1

Introduction

1.1 Stellar Evolution and Nucleosynthesis

How did the world we live in come into existence? Exploring the origin of the elements that make up the countless stars in the universe, the materials that form the Earth, and even our own bodies has long been a fundamental question for humanity. The key to unraveling this mystery lies in the process of nucleosynthesis, which occurs during cosmic phenomena such as stellar evolution and supernova explosions. In 1920, British astronomer Arthur Eddington first suggested that the energy source of the Sun could be the fusion of hydrogen. Later, in 1939, Hans Bethe demonstrated that elements are produced in stars through nuclear reactions and proposed the proton-proton chain reaction and the CNO cycle, thereby establishing the understanding that nuclear fusion reactions are the source of stellar power.

In this chapter, we will explain the mechanisms of nucleosynthesis driven by nuclear fusion reactions, tracing the process of stellar evolution.

1.1.1 Big Bang Nucleosynthesis

Nucleosynthesis in the early universe is explained by the theory of Big Bang Nucleosynthesis (BBN) [8]. This theory describes the process by which light elements such as hydrogen, helium, and lithium were formed through nuclear reactions that began just a few minutes after the birth of the universe. The idea that nuclear reactions are not only a source of stellar energy but also play an important role in nucleosynthesis was first proposed by George Gamow and Ralph Alfer in 1948 [9]. Although the assumption that nucleosynthesis progresses via neutron capture reactions was incorrect, it was groundbreaking as the first theoretical study linking cosmology and nucleosynthesis. Subsequent studies have improved the BBN model and made it consistent with observations of primitive elements.

According to the Big Bang theory, the universe initially existed in a state of extremely high temperature and density, and reached its present state through continuous expansion and cooling. Immediately after the birth of the universe, the thermal energy E was extremely high so that even strongly interacting elementary particle, quark and gluon, interacted weakly due to asymptotic freedom, and the universe is filled with quark-gluon plasma. As the universe expanded and cooled, quarks and gluons were confined in protons and neutrons. At $t = 1$ second, the thermal energy E exceeded the mass-energy difference between neutrons and protons $(m_n - m_p)c^2 = 1.24$ MeV, and statistical equilibrium was maintained by $\beta^{\pm}$ decays and their inverse processes. At $t = 2$ seconds, the thermal energy E decreased further ($T = 10^{10}$ K) and the proton and neutron were released from the equilibrium. These protons and neutrons could combine to form deuteron. However, at this stage, the equilibrium was maintained between the deuterons and proton-neutron pairs because deuterons were disintegrated by high-energy photons. Therefore, nucleosynthesis was suppressed until the temperature decreased sufficiently.

After $t = 3$ minutes, the thermal energy decreased to about 0.1 MeV, allowing deuterons to exist stably, and nuclear reactions began. The deuterons continuously captured protons and neutrons, producing ^{3}H, ^{3}He, and ^{4}He (α particles). However, there is no bound state of the nucleus with mass number $A = 5$, and ^{8}Be formed by fusion of two α particles is extremely short-lived and decays back to the two α particles. As a result, nucleosynthesis was stuck at this stage, and only a small amount of $A = 7$ nuclei were produced by reactions involving ^{3}H, ^{3}He, and ^{4}He, in addition to light nuclei up to ^{4}He. The fact is that these bottlenecks in the BBN nucleosynthesis, known as the "$A = 5$ and 8 bottlenecks", was one of the mysteries of astrophysics in the first half of the 20th century.

After $t = 20$ minutes, nucleosynthesis stopped because there was insufficient energy to continue the nuclear reaction. At this point, the universe consisted mostly of proton and α particles, with only a few other nuclei produced up to $A = 7$.

1.1.2 Nucleosynthesis in Stars

The next phase of nucleosynthesis began several hundred million years after the BBN. The light elements produced in the BBN, primarily hydrogen and helium, gradually gathered together due to gravity, and formed gas clouds. As these gas clouds underwent gravitational contraction, they heated up and reached a temperature sufficient for a fusion reaction. For stars with masses greater than $0.1\,M_{\odot}$, the central temperature reached about $10^7\,\mathrm{K}$ and hydrogen burning began.

The hydrogen burning occurs mainly through the proton-proton chain reactions and the CNO cycle, in which hydrogen nuclei are fused into helium. The energy released in this process increases the internal pressure, temporarily halting gravitational contraction and stabilizing the star as a main-sequence star. This stable phase continues until the hydrogen in the core is depleted.

At the end of the main-sequence phase, nuclear fusion ceases as the core runs out of hydrogen, and the energy supply is cut off. As a result, the core begins to contract under its own gravity. The contraction increases the core's temperature, and if the star is heavier than 0.5 $M_{\odot}$, the temperature rises to about $10^8\,\mathrm{K}$, triggering the next stage of nuclear fusion: helium burning. In helium burning, the triple-alpha process fuses three helium nuclei into carbon. During the helium burning, as $^{12}\mathrm{C}$ accumulates in the core, it captures an α particle to produce $^{16}\mathrm{O}$. On the other hand, If the star is lighter than 0.5 $M_{\odot}$, its core temperature does not reach 10^8 K, preventing nuclear fusion and resulting in the formation of a white dwarf. However, it is believed that white dwarfs composed of helium do not exist in the present universe because stars with such low mass would have lifetimes longer than the current age of the universe.

After helium in the core runs out due to the triple-alpha reaction, the core begins to contract again. However, if star is lighter than about 8 $M_{\odot}$, its core is supported by electron degeneracy pressure and does not reach the temperature required to ignite carbon-carbon fusion (carbon burning). As a result, the outer layers, which contain synthesized carbon and oxygen, are ejected, leaving behind a white dwarf composed of carbon and oxygen.

On the other hand, massive stars heavier than 8 $M_{\odot}$ proceed to subsequent stages of evolution, which involve the burning of heavier elements such as carbon and oxygen. If the stars are sufficiently massive, they eventually reach to the synthesis of elements up to iron. However, since iron cannot release energy through nuclear fusion, it marks the end of the stellar fusion process. As a result, gravitational contraction accelerates, leading to a supernova explosion. During the explosion, elements heavier than iron are produced via the *r*-process, and the outer layers of the star are ejected into space. The materials ejected by supernova explosions enrich the interstellar medium, where they contribute to the formation of the next generation of stars and planets.

1.1.3 Heavy Element Nucleosynthesis

Supernova Nucleosynthesis

Supernova explosions occur during the final stages of the evolution of massive stars heavier than $8\,M_{\odot}$. During the gravitational collapse of the stellar core, an extremely high-temperature and high-density environment is created, triggering a supernova explosion where elements heavier than iron are synthesized. The extreme physical conditions in supernovae enable nucleosynthesis processes that do not occur during normal stellar evolution.

Approximately half of elements heavier than iron are synthesized through the rapid neutron-capture process, known as the *r*-process. In the *r*-process, intense neutron flux leads to the rapid successive capture of neutrons by nuclei, forming neutron-rich unstable nuclei. These nuclei capture additional neutrons before undergoing β decay, resulting in the formation of extremely neutron-rich unstable isotopes. Subsequently, these unstable nuclei undergo a series of β decays, producing heavy elements such as gold (Au) and uranium (U). The *r*-process is the primary mechanism explaining the cosmic origin of many heavy elements in mid-shell regions between neutron magic numbers. Recent observations, such as the neutron star merger event GW170817 [10], have confirmed its occurrence.

On the other hand, proton-rich nuclei (called *p*-nuclei) are synthesized through the rapid proton capture process, known as the *rp*-process. In this process, nuclei rapidly capture protons under extremely high proton flux conditions, repeatedly undergoing β^+ decay and proton capture to increase their mass. However, the *rp*-process is limited by α decay, preventing the synthesis of nuclei heavier than ^{104}Te.

Furthermore, the *p*-process can also occur through photodisintegration reactions (γ, n) involving neutron-rich nuclei initially produced in the r-process, leading to the synthesis of p-nuclei heavier than $A = 104$. In the extreme environments of supernova explosions, there multiple nucleosynthesis processes can occur simultaneously, leading to the production of a wide variety of elements.

s-process

The slow neutron capture process (s-process) is another primary nucleosynthesis mechanism for synthesizing elements heavier than iron. This process occurs mainly during the asymptotic giant branch (AGB) phase of stellar evolution, within the helium-burning layers of red giant stars. A important feature of the s-process is that the timescale for neutron capture is much longer than the timescale for β decay. This allows nuclei to evolve along the neutron-rich side of the ”valley of stability” up to ^{208}Pb.

In the s-process, neutrons are primarily supplied by the (α, n) reactions of ^{13}C and ^{22}Ne. The neutron flux produced by these reactions is relatively low, and the stable conditions inside the star enable a stepwise capture of neutrons by nuclei. When a nucleus captures a neutron and becomes unstable, it undergoes β decay, increasing its proton number and transforming into a heavier element. The s-process begins with seed nuclei, primarily ^{56}Fe, which capture neutrons successively to produce elements up to ^{208}Pb. This series of reactions efficiently produces stable heavy elements around the neutron magic numbers. The s-process accounts for approximately 50% of the elements heavier than iron observed in the universe. Therefore, the neutron capture cross-sections of stable isotopes involved in the s-process have been systematically studied [11].

1.2 Triple-alpha Reaction

The triple-alpha reaction plays an important role in nucleosynthesis because it is the only process that can produce ^{12}C from light elements beyond the $A = 5$ and 8 bottlenecks. Because the triple-alpha reaction is a three-body reaction, it proceeds much more slowly than many other fusion reactions. Therefore, the triple alpha reaction is an important factor in determining the overall speed of heavy element synthesis in stars.

As proposed by Salpeter in 1952 [12], the triple-alpha reaction is described by a two-step nuclear reaction. First, two α particles fuse to form the ^{8}Be resonance state. Although ^{8}Be has an extremely short lifetime of 10^{-16} seconds, it can occasionally capture a third α particle before decaying back into two α particles, leading to the formation of the 3α resonance state as an excited state of ^{12}C. Most of these ^{12}C resonance states decay back to the original three alpha particles. However, with a slight probability, the excited ^{12}C nucleus de-excites to its ground state, resulting in the production of stable ^{12}C.

At typical stellar temperatures of 10^{8} K, the triple-alpha reaction proceeds mainly through the Hoyle state, the 0_2^+ state at $E_x = 7.65$ MeV of ^{12}C. The Hoyle state lies only 0.28 MeV above the 3α breakup threshold, making it critical for enhancing the reaction rate in stellar interiors. Furthermore, in extremely high-temperature environments exceeding 10^{9} K, recent studies have reported the importance of higher-lying states such as the 2_2^+ and 3_1^- states, which also contribute significantly to the nucleosynthesis in the universe [3, 13].

1.3 Hoyle State

The triple-alpha reaction in stellar interiors is significantly enhanced by a resonance reaction. In this context, Fred Hoyle predicted the existence of a resonance state in ^{12}C at an energy level suitable for promoting the triple-alpha reaction reaction, which was later experimentally confirmed [14, 15]. The prediction and discovery of this state was considered a significant achievement in both astrophysics and nuclear physics, and was later named the “Hoyle state” [16].

1.3.1 Historical Background

The process of ^{12}C production via the triple-alpha reaction had been discussed and theoretically calculated even before Hoyle’s prediction of the resonance state [17]. However, stellar model calculations at that time revealed that the triple-alpha reaction was an extremely rare process, and astrophysicists to propose various theoretical hypotheses to resolve this issue.

In 1953, Fred Hoyle explored the significance of resonance reactions in nucleosynthesis from carbon to nickel, and predicted the existence of a resonance state near the alpha-particle decay threshold of ^{12}C [15]. Furthermore, in 1957, Hoyle and Schwarzschild conducted calculations of stellar evolution from the main sequence to the red giant phase based on the triple-alpha reaction rates known at the time [18]. This paper systematically demonstrated the process of heavy element synthesis within stars by comparing theoretical predictions with experimental results. However, these calculations indicated that the ^{12}C produced by the triple-alpha reaction would rapidly convert into ^{16}O, leaving little ^{12}C remaining in the stellar core. To address this issue, Hoyle argued that the production rate of ^{12}C through the triple-alpha reaction needed to be at least comparable to or greater than the rate of ^{12}C consumption via alpha capture leading to ^{16}O formation. This calculations supported his earlier prediction for the resonance state [15].

On the other hand, a great deal of work was done by nuclear physicists on the energy levels of ^{12}C. Their main interest was whether $A = 4N$ nuclei show an α cluster structure. It had long been known that the alpha particle has the highest binding energy, and other $A = 4N$ nuclei were also known to have similarly high binding energies. Thus, a key question was whether these nuclei were composed of equal numbers of protons and neutrons or multiple alpha clusters. In particular, the detailed energy level structure of ^{12}C was investigated to determine whether its excited state could be described as a resonance state consisting of three alpha particles. In 1953, the same year Hoyle made his prediction, Wenzel *et al.* reported the observation of a resonance state at 7.68 MeV in ^{12}C using the $^{14}\mathrm{N}(d,\alpha)^{12}\mathrm{C}$ reaction [14]. Further investigations involving gamma-ray coincidence measurements [19] provided a detailed determination of the energy level structure of ^{12}C, including the Hoyle state. Moreover, the angular distributions of differential cross sections obtained by electron inelastic scattering [20] were analyzed, suggesting that the spin and parity of the Hoyle state were 0^+. Around the same period, Millar *et al.* used nuclear emulsions to observe the motion of ^{8}Be emitted from the photodisintegration of ^{12}C, reporting a lifetime of $(5 \pm 1) \times 10^{-14}$ s. This lifetime was found to be approximately 10^6 times longer than the typical crossing time of ^{8}Be and an alpha particle, confirming that the second step of the triple-alpha reaction could sufficiently occur [21].

These series of studies provide strong evidence for the existence of the

Hoyle state and its important contribution to the triple alpha reaction, and are widely accepted as major achievements in both nuclear physics and astrophysics [16].

1.3.2 Decay Width of the Hoyle State

The level scheme of ^{12}C currently known is shown in Fig. 1.3.1. The Hoyle state (E_x = 7.65 MeV) lies 0.28 MeV above the ^{8}Be + α threshold, which corresponds to the peak of the Gamow window at a typical stellar temperature of 2.5×10^8 K [22]. At higher temperatures exceeding 10^9 K, the Gamow window shifts to higher energies, making higher excited states, such as the 3_1^- state shown in Fig. 1.3.1, more significant. Almost all of the Hoyle state undergoes α decay. However, it also exhibits rare electromagnetic decay modes, including γ decay ($0_2^+ \to 2_1^+ \to 0_1^+$) and positron-electron (e^+e^-) pair decay ($0_2^+ \to 0_1^+$). The reaction rate of the triple-α process, $\langle \rho v \rangle$, can be expressed using the decay widths and the resonance energy E_r of the Hoyle state [23] as :

$$\langle \rho v \rangle \propto \frac{\Gamma_\alpha \Gamma_{\mathrm{rad}}}{\Gamma} \times T_9^{-3/2} \exp\left(\frac{-11.605 E_r}{T_9} \right). \tag{1.1}$$

Here, Γ, Γ_α, and $\Gamma_{\mathrm{rad}}(= \Gamma_\gamma + \Gamma_{e^+e^-})$ represent the total width, α decay width, and radiative decay width of the Hoyle state, respectively, where Γ_γ and $\Gamma_{e^+e^-}$ denote the γ decay width and the e^+e^-–pair decay width. Since the radiative decay of the Hoyle state is extremely rare, it can be approximated that $\Gamma \approx \Gamma_\alpha$, indicating that the reaction rate $\langle \rho v \rangle$ is highly sensitive to Γ_{rad}.

Direct experimental measurement of Γ_{rad} is challenging. Therefore, it has been determined by measuring each parameter in Eq. (1.3).

$$\begin{aligned} \Gamma_{\mathrm{rad}} &= \left[\frac{\Gamma_{\mathrm{rad}}}{\Gamma} \right] \times \left[\frac{\Gamma}{\Gamma_{e^+e^-}} \right] \times \left[\Gamma_{e^+e^-} \right], & (1.2) \\ &= \left[\frac{\Gamma_\gamma}{\Gamma} \right] \times \left[\frac{\Gamma}{\Gamma_{e^+e^-}} \right] \times \left[\Gamma_{e^+e^-} \right] + \left[\Gamma_{e^+e^-} \right]. & (1.3) \end{aligned}$$

Here, $\Gamma_{\mathrm{rad}}/\Gamma$ represents the radiative-decay probability of the Hoyle state, while $\Gamma/\Gamma_{e^+e^-}$ denotes the e^+e^-–pair decay probability.

The value of Γ_γ/Γ was extensively measured between the 1960s and 1970s

[24–31], and a recommended value of $\Gamma_\gamma/\Gamma = 4.09(11) \times 10^{-4}$ is provided by the experimental compilation [1]. Details of the measurement methods are described in Sec. 1.4.

During the same period, $\Gamma/\Gamma_{e^+e^-}$ was determined by measuring the e^+e^- pairs emitted from the Hoyle state using a magnetic pair spectrometer and scintillation detectors [32–34]. Currently, a weighted average of three independent results give a recommended value of $\Gamma_{e^+e^-}/\Gamma = 6.7(6) \times 10^{-6}$ [1].

The decay width $\Gamma_{e^+e^-}$ has been estimated using the ratio of the elastic to inelastic form factors obtained from electron scattering measurements of ^{12}C, a method initially proposed by Crannell *et al.* [35]. Multiple measurements have been reported using this technique [36–38]. The most recent measurement in 2010 reported a value of $\Gamma_{e^+e^-} = 62.3(20)\,\mu$eV [39], which has been recommended in [1].

Using these results, the radiative decay width has been calculated as $\Gamma_{\rm rad} = 3.87(39)$ meV, which is widely accepted today. The 10% uncertainty in $\Gamma_{\rm rad}$ is primarily due to discrepancies among the individual measurements of $\Gamma_{e^+e^-}/\Gamma$.

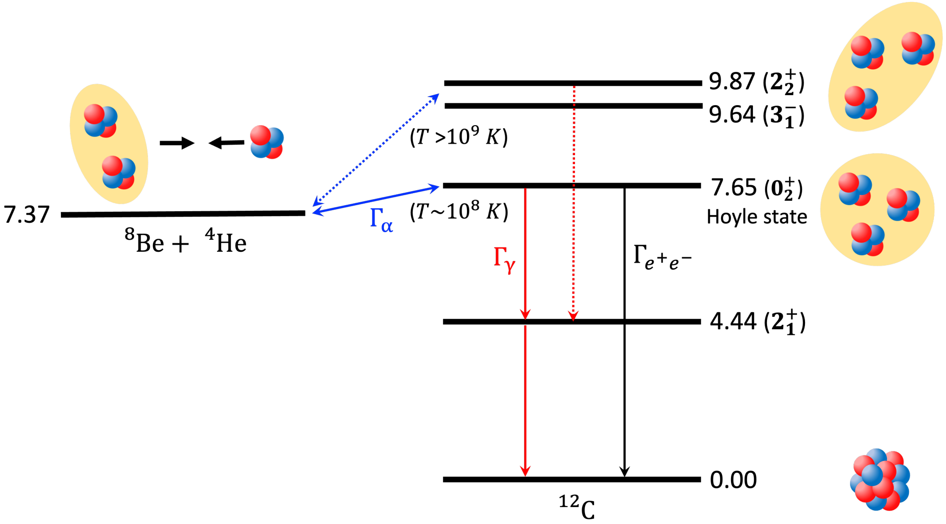

Figure 1.3.1: Level diagram of ^{12}C

1.4 γ-decay Probability of Hoyle State

1.4.1 Research Method

Once the existence of the Hoyle state was experimentally confirmed, the γ decay probability Γ_γ/Γ actively measured, as it is a critical parameter governing the reaction rate of the triple-alpha process. The γ decay of the Hoyle state can be identified by detecting either the two emitted γ rays or the surviving ^{12}C nucleus.

γ-Detection Method

The γ-decay probability of the Hoyle state measured using the γ-detection method is given as :

$$\left(\frac{\Gamma_\gamma}{\Gamma}\right)^{7.65} = \frac{N_{020}^{7.65}}{N_{\mathrm{singles}}^{7.65} \times \epsilon_{3.21} \times W_{020}^{7.65} \times \epsilon_{4.44}}. \tag{1.4}$$

Here, $N_{\mathrm{singles}}^{7.65}$ represents the total number of Hoyle states populated, $N_{020}^{7.65}$ denotes the number of the γ-decay events where the two γ rays were detected in coincidence, ϵ is the detection efficiency for the 4.44-MeV and 3.21-MeV γ rays, and $W_{020}^{7.65}$ is the correction factor for the angular correlation coefficient for the two γ rays.

In 1961, Alburger *et al.* experimentally measured the γ-decay probability Γ_γ/Γ for the first time [24]. They populated the Hoyle state using the $^{10}\mathrm{Be}(^{3}\mathrm{He},\mathrm{p})^{12}\mathrm{C}$ reaction and performed proton–γ–γ coincidence measurements by detecting protons with a CsI detector and γ rays with two NaI detectors. Although they reported the γ-decay probability as $3.3(9)10^{-4}$, its systematic uncertainty is as high as about 30%. Their measurements suffered from significant systematic uncertainities due to contamination of the excitation-energy spectrum from ^{11}B in the target and the correction factor for the angular correlation between the two γ rays $W_{020}^{7.65}$ was not taken into account.

The second measurement using the γ-detection method was conducted in 1976 by Obst *et al.* [31]. They populated the Hoyle state using the $^{12}\mathrm{C}(\mathrm{p},\mathrm{p}')^{12}\mathrm{C}$ reaction and performed proton–γ–γ coincidence measurements by detecting protons with a Si detector and γ rays with four NaI detectors. Additionally, they measured the cascade γ decay ($0_2^+ \to 2_1^+ \to 0_1^+$) from the

4.98-MeV excited state of ^{28}Si using the same detection system. Since this excited state decays by sequentially emitting two γ rays of 3.20 MeV and 1.78 MeV with nearly 100% probability, the relationship described in Eq. (1.5) was obtained.

$$\left(\frac{\Gamma_\gamma}{\Gamma}\right)^{4.98} = 1 = \frac{N^{4.98}_{020}}{N^{4.98}_{\text{singles}} \times \epsilon_{1.78} \times W^{4.98}_{020} \times \epsilon_{3.20}}. \tag{1.5}$$

By taking the ratio of Eq. (1.4) to Eq. (1.5), the γ-decay probability Γ_γ/Γ can be expressed in the simplified form shown in Eq. (1.6).

$$\left(\frac{\Gamma_\gamma}{\Gamma}\right)^{7.65} = \frac{N^{7.65}_{020}}{N^{4.98}_{020}} \times \frac{N^{4.98}_{\text{singles}}}{N^{7.65}_{\text{singles}}} \times \frac{\epsilon_{1.78}}{\epsilon_{4.44}} \times \frac{\epsilon_{3.20}}{\epsilon_{3.21}} \times \frac{W^{4.98}_{020}}{W^{7.65}_{020}}. \tag{1.6}$$

Here, since $\epsilon_{3.20}/\epsilon_{3.21} \approx 1$, the gamma-ray detection efficiency for these energies does not need to be determined. Similarly, as $W^{4.98}_{020}/W^{7.65}_{020} \approx 1$, the correction factor for the angular correlation between the two γ rays can also be neglected. Thus, the advantage of this approach is that the detection efficiencies only for the 1.78-MeV and 4.44-MeV γ rays are required to calculate the γ-decay probability of the Hoyle state. This method has been adopted in subsequent measurements using the γ-detection method.

^{12}C-detection method

The radiative-decay probability of the Hoyle state measured using the ^{12}C-detection method is given by Eq. (1.7).

$$\left(\frac{\Gamma_{\text{rad}}}{\Gamma}\right)^{7.65} = \frac{N^{7.65}_{^{12}\text{C}}}{N^{7.65}_{\text{singles}} \times \epsilon}. \tag{1.7}$$

Here, $N^{7.65}_{\text{single}}$ represents the yield of the Hoyle states, $N^{7.65}_{^{12}\text{C}}$ denotes the number of radiative decays where a surviving ^{12}C was detected in coincidence, ϵ is the coincidence detection efficiency for the scattered particle and surviving ^{12}C. In general, compared to the γ-detection method, this method detects only charged particles, resulting in higher detection efficiency. Therefore, a lot of measurements using the ^{12}C-detection method were conducted in

1960s and 1970s [25–30].

A difficulty of this method is the treatment of significant background caused by 3α-decay events of ^{12}C and neutron emission events from ^{13}C contaminants in $^{\mathrm{nat}}$C target. In 1960s, two experiments were conducted using the ^{12}C-detection method [25, 26]. They populated the Hoyle state using the $^{14}\mathrm{N}(\mathrm{d}, \alpha)^{12}\mathrm{C}$ and $^{10}\mathrm{B}(^{3}\mathrm{He}, \mathrm{p})^{12}\mathrm{C}$ reactions respectively, and both the scattered particle and the surviving ^{12}C were detected with Si detectors. To reduce the background from 3α decay, the surviving ^{12}C was momentum-analyzed by the magnetic spectrometer before detecting. Although both experiments successfully eliminated most of the α-particle background using momentum analysis and ToF measurements, background events of ^{11}B and ^{13}C due to target contamination remained. The excited state of ^{13}C at $E_x = 7.67$ MeV decays by neutron emission, transforming into ^{12}C, which can be detected in coincidence with the scattered particle. The kinematics of this state are very similar to those of the Hoyle state, and the angular resolution of these experiments was insufficient to separate them. As a result, the measurement of $N^{7.65}_{^{12}\mathrm{C}}$ suffered from significant systematic uncertainties.

In the measurements conducted during the 1970s, the $^{12}\mathrm{C}(\mathrm{p}, \mathrm{p}')^{12}\mathrm{C}$ and $^{12}\mathrm{C}(\alpha, \alpha')^{12}\mathrm{C}$ reactions were used [27,28,30]. The scattered particle and the surviving ^{12}C were detected using Si detectors. Compared to Ref. [25, 26], the angular resolution was improved by positioning the detectors further from the target. As a result, although the ^{13}C background could not be completely eliminated, the high signal-to-noise ratio (S/N) allowed for precise measurements.

It should be noted that the ^{12}C detection method provides the radiative-decay probability while the γ-ray detection method directly gives the γ-decay probability. The radiative-decay probability is the sum of the e^+e^- pair-production-decay probability and γ-decay probabilities as $\Gamma_{\mathrm{rad}}/\Gamma = \Gamma_{e^+e^-}/\Gamma + \Gamma_\gamma/\Gamma$. The e^+e^- pair-production-decay probability was recently reported as $\Gamma_{e^+e^-}/\Gamma = 8.2(5) \times 10^{-6}$ [40] whereas $\Gamma_{e^+e^-}/\Gamma = 6.7(6) \times 10^{-6}$ was adopted in the previous compilation [1]. The weighted averaged value between these two values of $\Gamma_{e^+e^-}/\Gamma = 7.6(4) \times 10^{-6}$ was used to deduce Γ_γ/Γ from $\Gamma_{\mathrm{rad}}/\Gamma$ in this work.

Summary of the Previous Measurements

A summary of the previous experimental results is presented in Fig. 1.4.1. In the 1960s, the first measurements of the γ-decay probability Γ_γ/Γ were affected by significant experimental uncertainties due to several technical difficulties. However, by the 1970s, improvements in measurement techniques allowed for more precise determinations of Γ_γ/Γ, yielding consistent results with each other. Therefore, the recommended value of $\Gamma_\gamma/\Gamma = 4.09(11)\times10^{-4}$ provided by the experimental compilation [1] has been widely accepted.

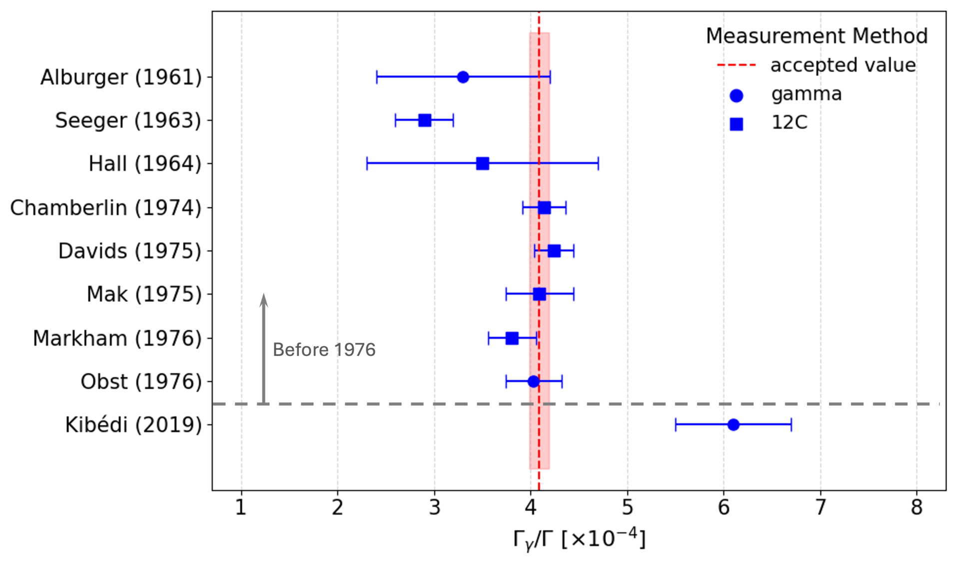

Figure 1.4.1: Summary of the measured Γ_γ/Γ values in 1960s and 1970s. In addition, new striking data by kibedi ware also plotted.

1.4.2 Recent Measurements

Recently, the radiative decay probability was re-measured by Kibédi *et al.* using the detection of two γ rays from the cascade decay of the Hoyle state populated by the $^{12}\mathrm{C}(\mathrm{p},\mathrm{p}')^{12}\mathrm{C}$ reaction [2]. The newly reported value of $\Gamma_\gamma/\Gamma = 6.1(6)\times10^{-4}$ is approximately 50% higher than the literature value from Ref. [1]. They employed the same experimental and analytical techniques as Obst *et al.* [31], with improved gamma-ray detection efficiency and energy resolution compared to previous experiments. The reason for the significant discrepancy in the measured Γ_γ/Γ remains unclear. Kibédi *et al.*

claimed that the ^{12}C-detection method might not be suitable for determining the γ-decay probability, as high counting rates could introduce accidental coincidences from the 3α decay, complicating coincidence measurements.

1.4.3 Aim of This Research

The purpose of this research is to solve the recently reported discrepancy in the γ-decay probability of the Hoyle state. Previous studies employed the two completely different methods, suggesting systematic differences between the two methods might arise.

In this study, we will conduct the first experiment combining the ^{12}C-detection method using a Si detector and the γ-detection method using the ROSPHERE gamma-ray spectroscopy array. To address the statistical limitation of the γ-detection method, the Si detector will be placed closer to the target to increase the yield. Although placing the Si detector closer to target will prevent the use of the ToF method, coincidence measurements with the γ rays are expected to effectively suppress background events from 3α decay and ^{13}C contaminants. Additionally, the use of a DC beam is expected to suppress accidental coincidence events, addressing the issue highlighted in Ref. [2].

This novel approach, which directly compares the systematic differences between the two detection methods, aims to conclusively solve the puzzle about the γ-decay probability of the Hoyle state.

Chapter 2

Development of PSD method with Si detector

2.1 Aim of Research

In nuclear experiments, the identification of emitted particles is an essential process. Currently, two methods are widely used for the identification of charged particles: the E-ΔE method and the Time-of-Flight (ToF) method. The E-ΔE method involves injecting charged particles into both a transmission and a non-transmission detector, and identifying particles by using energy correlations in both detectors. While this method provides good particle identification capability for particles that can penetrate the first detector, it can not be applied to low-energy particles that can not penetrate the first detector. In the measurement of nuclear reactions related to astrophysical phenomena, it is necessary to discriminate low-energy protons and α particles from other particles. For example, a 3 MeV α particle penetrates to a depth of only about 12 µm in Si. It is challenging to prepare a large-area detector thin enough for such low-energy particles to pass through. On the other hand, the ToF method determines particle mass by using a correlation between the detected energy and the time it takes for a particle to travel from the reaction point to the detector. However, to achieve high particle identification (PID) resolution with the ToF method, it is necessary to have a sufficiently large distance between the target and the detector. In such cases, the solid angle of the detector is significantly reduced, making it difficult to apply this method to experiments with limited statistics. Therefore, conventional particle identification methods pose challenges when attempting to detect and identify low-energy charged particles with a large solid angle, which makes it difficult to conduct certain physics experiments.

To overcome the limitations of conventional PID methods, this research focuses on particle identification based on waveform analysis using Si detectors. In this method, differences in the signal waveforms output from the detector are used to identify the type of particles. In recent years, several studies have demonstrated the usefulness of particle identification using energy and waveform information measured by detectors [41–44]. Additionally, the advancement of digitizing modules and DAQ systems has made it easier to implement waveform analysis methods in nuclear experiments Given this background, waveform analysis methods may offer a novel solution to challenges previously considered difficult to address with conventional methods.

The aim of this study is to explore experimental setups that achieve optimal particle identification performance and validate waveform analysis methods as a basis for applying these techniques in future experiments.

2.2 Principle of Si Detectors

2.2.1 Properties of Semiconductors

In materials with a crystal structure, the energy levels that electrons can occupy form a band structure consisting of three regions: the valence band, the forbidden band, and the conduction band. The valence band refers to energy levels where electrons are tightly bound to specific crystal sites, while the conduction band refers to energy levels where electrons can move freely through the crystal. The energy gap where no electrons exist between these two bands is called the forbidden band. Semiconductors have a narrow forbidden band width of about 1 eV, allowing electrons to be easily excited to free electrons, which makes them useful as radiation detectors.

Doping impurities to a semiconductor alters its energy band structure. When a pentavalent impurity is doped to tetravalent Si, one extra electron is introduced, forming impurity levels near the conduction band within the forbidden band, which raises the Fermi level of the semiconductor. Conversely, when a trivalent impurity is doped, one electron in the valence band is missing, forming impurity levels near the valence band within the forbidden band, which decrease the Fermi level of the semiconductor. Semiconductors doped with pentavalent and trivalent impurities are referred to as N-type semiconductors and P-type semiconductors, respectively.

2.2.2 PN Junction

When a P-type semiconductor and an N-type semiconductor are joined, holes move to the N-type semiconductor, and electrons move to the P-type semiconductor. This movement of carriers continues until the Fermi levels of the P-type and N-type semiconductors are aligned at the junction interface. Due to this charge movement, the N-type semiconductor becomes positively charged, and the P-type semiconductor becomes negatively charged. As a result, a contact potential V_c develops across the PN junction, forming a depletion layer where no free carriers exist (upper left of Fig. 2.2.1). When radiation enters this region, electrons are excited from the valence band to the conduction band, generating electron-hole pairs that can be read out by the electric field. Applying a reverse bias voltage to the PN junction causes the carriers to overcome the potential barrier at the junction and recombine, which extends the depletion layer (right of Fig. 2.2.1). The voltage at which the entire detector becomes a depletion layer is called the full-depletion voltage. At this voltage, the entire detector becomes a sensitive region, allowing accurate readout of the energy of the incident radiation.

2.2.3 Structure of Si Semiconductor Detectors

Simply pressing a P-type semiconductor and an N-type semiconductor together does not work effectively because the junction interface will have gaps larger than the lattice spacing. In general, Si semiconductor detectors are constructed by doping an N-type (or P-type) bulk semiconductor with a high concentration of P-type (or N-type) impurities. The doped surface is referred to as the Junction surface, and the opposite surface is called the Ohmic surface. When electrons move toward the P-type side forming a depletion layer, the carriers distribute deep into the bulk side becuse the bulk side has a low concentration of carriers. As a result, the spatial charge $\rho(x)$, potential $\phi(x)$, and electric field $E(x)$ distributions along the depth of an Si detector are represented as shown in Fig. 2.2.1, forming a non-uniform electric field within the detector.

When a charged particle enters a fully depleted Si detector, electron-hole

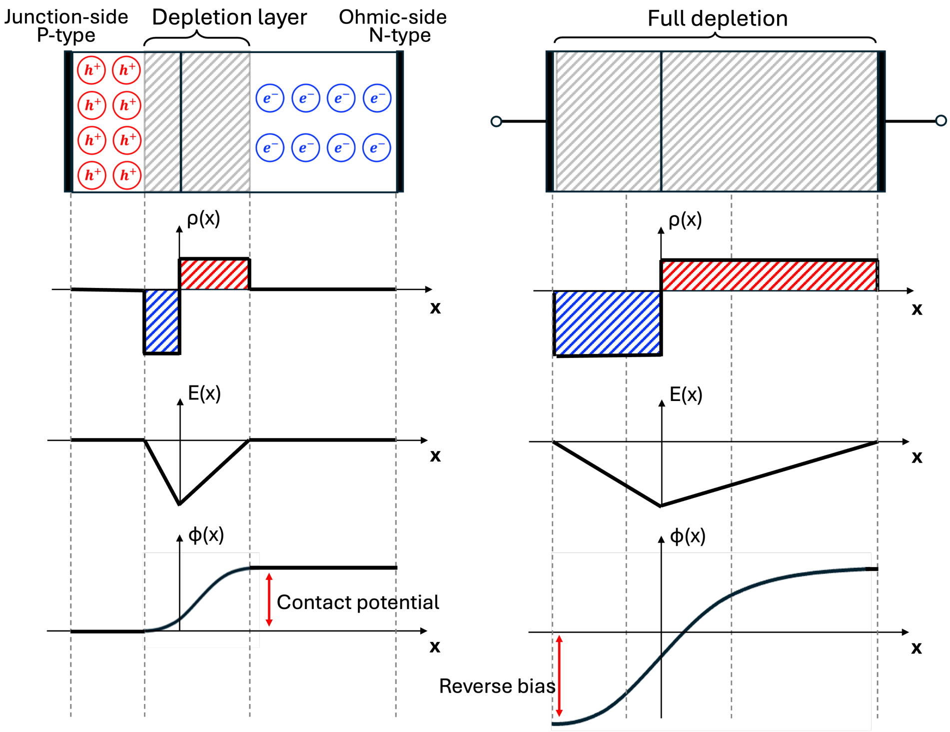

Figure 2.2.1: Spatial charge distribution $\rho(x)$, electric field $E(x)$, and potential distribution $\phi(x)$ along the depth of an Si detector. The left diagram shows a P-type impurity doped into an N-type bulk semiconductor. The right diagram illustrates the expansion of the depletion layer when a reverse bias voltage is applied.

pairs are generated along its trajectory. Due to the internal electric field, the electrons and holes move to the electrode, and the signals are read out. At this time, the energy loss of the charged particle follows the Bragg curve, reaching a maximum just before the particle comes to stop. Therefore, the output signal waveform of the Si detector is strongly correlated with the magnitude of the electric field near the stopping position of the particle. Since the electric field near the Junction surface is stronger compared to the Ohmic surface, charge readout is faster, resulting in superior time resolution. For this reason, conventional experiments using Si detectors generally inject particles from the Junction surface. On the other hand, it is expected that the waveform differences between particle types will be more significant at the Ohmic surface due to the smaller internal electric field. In the following chapters, the Junction surface will be referred to as the Front surface, and the Ohmic surface will be referred to as the Rear surface.

2.3 Study of Waveform Characteristics of Si Detector

As the first stage in the development of a Pulse Shape Disctimination (PSD) method based on waveform analysis, we investigated the waveform characteristics of the Si detector. The experiment was conducted using the tandem electrostatic accelerator at Kobe University, where waveforms of 3 MeV protons (p), deuterons (d), and α particles were obtained. By comparing the different types of Si detectors, particle incidence surface, and preamplifier combinations, we explored the optimal experimental setup for achieving effective particle identification.

2.3.1 Test Experiment

The experiment was carried out from October 26 to November 1, 2020, at the p45 beamline of the Kobe University tandem electrostatic accelerator facility. In this experiment, a tandem Van de Graaff electrostatic accelerator with a maximum terminal voltage of 1.7 MV was used to irradiate a target with 3.03 MeV p and d beams. A 0.17 µm gold foil was used as the target, and scattered particles were detected by the Si detector via Rutherford scattering. Additionally, a triple-mixed α source owned by Research

Center for Nuclear Physics (RCNP) was placed at the target position, and the emitted α particles were directly incident on the Si detector for detection. The α particles emitted from ^{148}Gd in the triple-mixed source have an energy of 3.182 MeV, which is approximately equal to the energies of the p and d beams accelerated by the tandem electrostatic accelerator. The Si detector was placed at 180 mm from the target and at an angle of 30 degrees relative to the beam axis. The output signals from the detector were amplified by two charge-integrating preamplifiers, and waveforms were recorded using CAEN V1730SB 500 MS/s flash digitizers. To generate triggers, the signal from the Rear surface was split into two and input into the MSCF-16. By adjusting the Constant Fraction Discriminator (CFD) threshold in the MSCF-16, triggers were set to be generated when one or more particles with energies above 1 MeV were detected. When a trigger signal was input to the V1730SB, waveform data for all channels were recorded over a period of 8 µs.

To achieve optimal particle identification performance, measurements were conducted by varying the particle incidence surface (Front, Rear), the type of Si detector (Nomal and NTD), and the type of preamplifier (MPR-16, A1442B). The particle identification performance for each combination was compared. Table 2.1 shows the four experimental setup combinations.

Table 2.1: Experimental setup combinations which used the test experiment

	Incident side	Si type	Preamplifier
(a)	Rear	NTD-Si	A1442B
(b)	Front	NTD-Si	A1442B
(c)	Rear	Normal-Si	A1442B
(d)	Rear	NTD-Si	MPR-16

2.3.2 NTD–Si

Neutron Transmutation Doping (NTD) is a method for producing N-type semiconductors by placing a Si single crystal in a nuclear reactor and irradiating it with neutrons for a specific period. Natural Si single crystals consist of three isotopes: ^{28}Si (92.23% natural abundance), ^{29}Si (4.67%), and ^{30}Si (3.10%). When neutrons irradiate this crystal, the ^{30}Si$(\mathrm{n},\gamma)^{31}$Si$(\beta)^{31}$P reaction produces ^{31}P within the crystal, uniformly doping the crystal with ^{31}P, an N-type impurity. The N-type semiconductor material produced by this method is called NTD–Si and exhibits a crystal uniformity that cannot be achieved by conventional impurity-doping methods. Non-uniformity of N-type impurities can distort the electric field distribution within the detector and potentially affect the output waveforms. Therefore, in this experiment, we compared the performance of NTD-type and Normal-type Si detectors of the same design and evaluated the usefulness of NTD-Si in waveform analysis.

Figure 2.3.1 shows a schematic diagram of the MMM-design double-sided Si strip detectors used for PSD testing, manufactured by Micron Semiconductor Ltd. The readout electrodes are divided into 16 arc-shaped strips on the Front surface and 8 radial strips on the Rear surface. The perimeter of the detector is surrounded by a thin electrode called a guard ring. In the below discussion, the largest strip on the Front surface is referred to as Ch 0, and the smallest strip as Ch 15. On the Rear surface, the strip closest to the bonding wire of the guard ring is referred to as Ch 0, and the farthest strip as Ch 7.

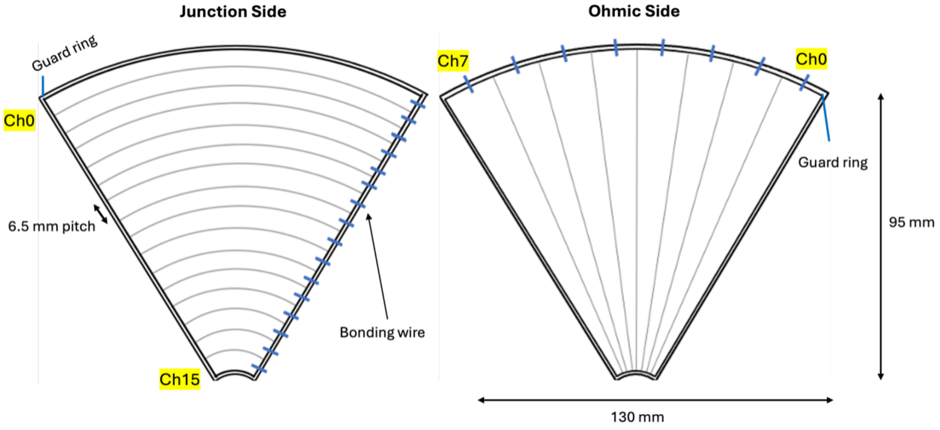

Figure 2.3.1: Schematic diagram of the Si detector. The Junction surface (left) is divided into 16 arc-shaped strips, and the Rear surface (right) is divided into 8 radial strips.

2.3.3 Preamplifier

In this experiment, two types of charge-integrating preamplifiers were used: the MPR-16 manufactured by Mesytec and the A1442B manufactured by

CAEN. The specifications of the preamplifiers used for the measurements are shown in Table 2.2. The gain of the preamplifiers was set to 160 mV/MeV and 100 mV/MeV, respectively, and signals from both surfaces of the Si detector were input. The bias voltage for the Si detector was applied to the detector surface via the preamplifier, while the rear surface of the detector was grounded by shorting the voltage input terminal of the preamplifier to 50 Ω.

Table 2.2: Specifications of the two preamplifiers used in the measurements.

	Mesytec MPR-16	CAEN A1442B
Output amplitude	0 to ± 4 V	0 to ± 4.5 V
Gain	160 mV/MeV	100 mV/MeV
Polarity	inverted	not inverted
Number of channels	16	32
Rise time	12 ns @ 0pF	<10 ns @ 0 pF
Decay time	25 μs	50 μs
Vias Voltage	± 400 V max	± 400 V max

2.4 Digital Signal Processing

2.4.1 Noise Filtering

Figure 2.4.1 shows the waveform of the α particle obtained from Ch 8 on the Front surface of the NTD–Si detector using the setup in Table 2.1(d), along with the histogram of the peak ADC values. The average signal level in the time window between 600 and 800 ns was defined as the baseline for each event, and the value corresponding to the maximum difference between the ADC channel and tje baseline was defined as the peak amplitude. Under these conditions, the energy resolution for the 3.18 MeV α particle from ^{148}Gd was 1.8% (sigma).

Next, we attempted to improve the energy resolution by introducing digital signal processing. In conventional experiments without waveform analysis, the Si detector signal is amplified by a preamplifier, and noise reduction is performed by selecting specific frequency bands using a CR–RC$^{\mathrm{n}}$ shaping circuit. In this study, a Finite Impulse Response (FIR) filter was introduced to implement the CR–RC$^{\mathrm{n}}$ circuit in software. The FIR

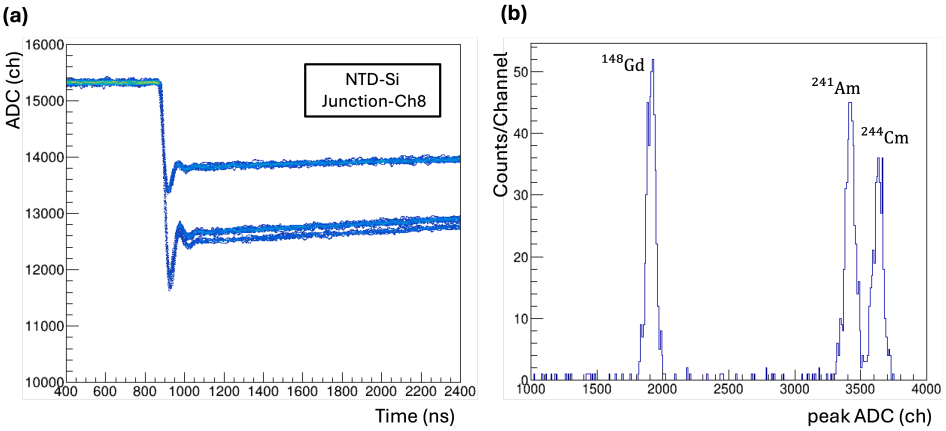

Figure 2.4.1: Signal waveform of Ch 8 on the Front surface of the Si detector amplified with the Mesytec MPR-16 (left) and the histogram of the peak ADC channels (right).

filter applies convolution to the input signal $x[n]$ with a filter length N to produce the output signal $y[n]$:

$$y[n] = \sum_{k=0}^{N} h[k]x[n-k] \tag{2.1}$$

Here, $h[k]$ represents the weights applied to each input signal, allowing for signal processing with specific frequency characteristics by appropriately setting these weights. The parameters necessary for filter design were obtained using a web-based digital filter design program developed by the Yamada Laboratory at the National Institute of Technology, Ishikawa College [45].

In this analysis, a high-pass filter (HPF) with a low cutoff frequency of 0.25 MHz and a low-pass filter (LPF) with a high cutoff frequency of 1.5 MHz were designed. Filtering was performed by applying the HPF once, followed by the LPF three times. The filter length was set to $N = 401$, and a Hamming window was used to adjust the frequency characteristics. The Hamming window is one of the window functions used in FIR filter design and enhances frequency resolution by emphasizing specific frequency regions.

Figure 2.4.2 shows the waveform and histogram of the peak ADC values after applying the filters to the signal shown in Figure 2.4.1. As a result, the energy resolution for the 3.18 MeV α particle from ^{148}Gd improved to

1.3% (sigma), demonstrating the effectiveness of digital signal processing for noise reduction.

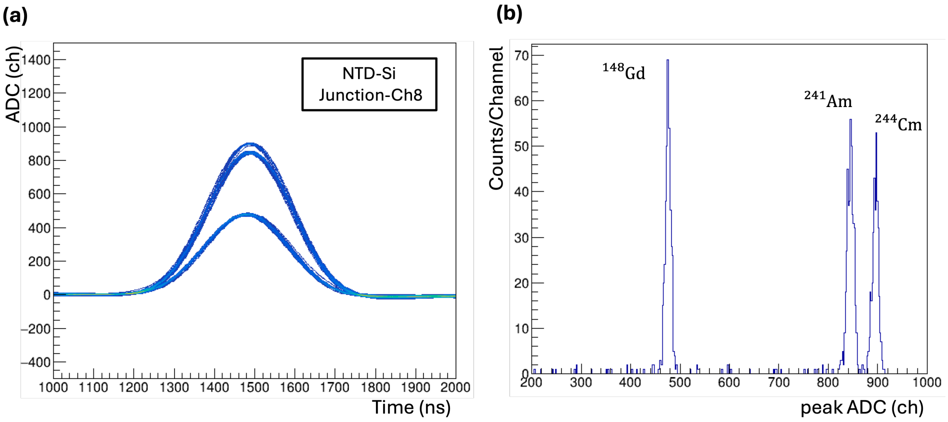

Figure 2.4.2: Waveform (left) and histogram of the peak ADC channels (right) after applying an HPF once and an LPF three times to the signal shown in Figure 2.4.1.

2.4.2 Development of PSD Method

In this experiment, since charge-integrating preamplifiers were used, the differential signal of the acquired waveform is expected to reflect the current signal of the Si detector. Therefore, waveform differentiation was performed using a triangle filter. The triangle filter is a differentiation filter expressed by the following equation, where the filter length L is used:

$$y_i = \frac{\left(\sum_{k=0}^{L-1} x_{i+k}\right) - \left(\sum_{k=-L}^{-1} x_{i+k}\right)}{L} \tag{2.2}$$

Here, L represents the filter length, which is a free parameter that can change the frequency characteristics of the digital filter. For subsequent analyses, $L = 20$ was used to calculate the PID parameter, the value that provides the best particle identification performance. In this analysis, waveform used in the calculation was normalized by its maximum amplitude, setting the signal baseline to 0 and the maximum value to 1.

Figure 2.4.3 shows the averaged differential waveforms for 5,000 events of p, d, and α particles obtained using the MPR-16 preamplifier. It was found that the amplitude and the rise time of the differential waveforms varied depending on the particle type. Therefore, the maximum amplitude of the signal was defined as $A_{\max}$ and used as the PID parameter for PSD.

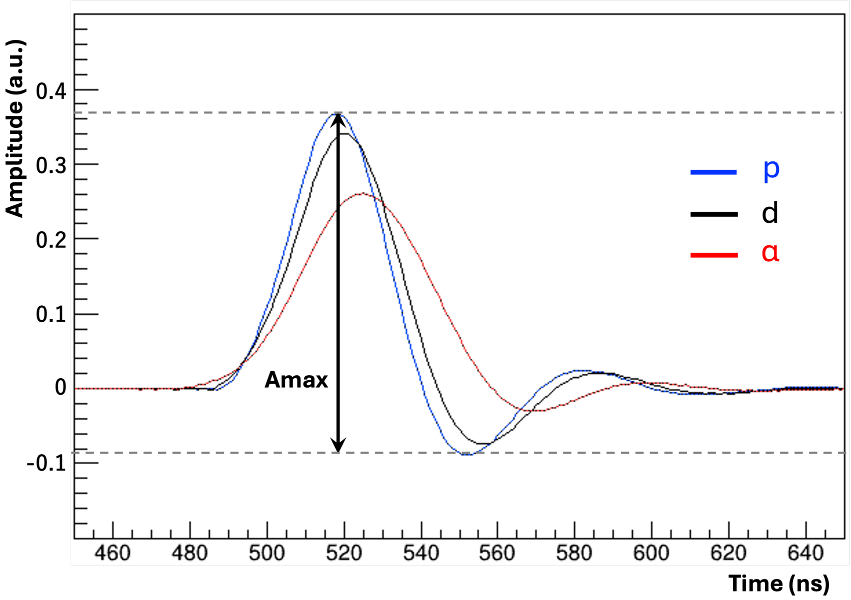

Figure 2.4.3: Averaged differential waveforms for p, d, and α particles obtained by applying a triangle filter to the acquired waveforms. The maximum amplitude $A_{\max}$ is defined as the PID parameter for PSD.

The separation power $R_{\mathrm{x/y}}$, a measure of PID capability, is defined as follows:

$$R_{\mathrm{x/y}} = \frac{|\mu_{\mathrm{x}} - \mu_{\mathrm{y}}|}{2(\sigma_{\mathrm{x}} + \sigma_{\mathrm{y}})} \tag{2.3}$$

Here, μ_{x} and σ_{x} represent the mean and standard deviation of the distribution of the PID parameter for each particle, which is obtained by fitting with a Gaussian function. When the separation power $R_{\mathrm{x/y}}$ equals 1, it means that approximately 97.7% of the particles are correctly identified if the two peaks of particle x and particle y follow Gaussian distributions and have equal counts. In the subsequent analyses, the separation power will be used to evaluate the PID performance for each setup and determine the optimal configuration.

2.5 Comparison of PSD Performance for Each Experimental Setup

Figure 2.5.1 shows the A_{max} distributions for p, d, and α particles obtained using the four setups listed in Table 2.3. Table 2.3 presents the separation power $R_{\mathrm{x/y}}$ calculated using Eq. (2.3). In the setup shown in Figure 2.5.1(a) as the basis for comparison, good separation was achieved between p/α and d/α particles with different atomic numbers Z. However, while some differences were observed in the A_{max} distributions for p and d particles, which have the same atomic number, good separation was not achieved.

Particle incidence surface

Regarding the particle incidence surface, comparing Figures 2.5.1(a) and (b) shows that when particles are incident on the Front surface, the differences in A_{max} values for each particle become smaller. When particles are incident on the Front surface, the electron-hole pairs generated by each particle experience a stronger electric field compared to the Rear surface, resulting in faster time response. However, due to the reduced impact of differences in stopping positions and electron-hole pair distributions on the rise time of the signal, waveform analysis is less effective in this case.

Type of Si detector

Regarding the type of Si detector, comparing Figures 2.5.1(a) and (c) reveals that when using Normal-Si, the variance of A_{max} increases, and sufficient separation is not achieved compared to NTD-Si. This is likely because Normal-Si has poorer crystal uniformity compared to NTD-Si, distorting the detector's electric field distribution and increasing variations in the output waveform.

Preamplifier

Regarding the preamplifier, comparing Figures 2.5.1(a) and (d) shows that the MPR-16 provides higher PID performance. This is likely because the MPR-16 has a wider frequency bandwidth compared to the A1442B. As shown in Figure 2.4.1(a), signals obtained using the MPR-16 exhibit a damped oscillation structure after the initial rise. This structure does not appear in the setup shown in Table 2.3(a), resulting in differences in $A_{\max}$ depending on the preamplifier used. Therefore, the wider frequency bandwidth of the MPR-16 makes it advantageous for waveform analysis.

In conclusion, setup (d) was confirmed to be optimal for particle discrimination using waveform analysis. Therefore, future experiments utilizing waveform analysis will performed with setup (d).

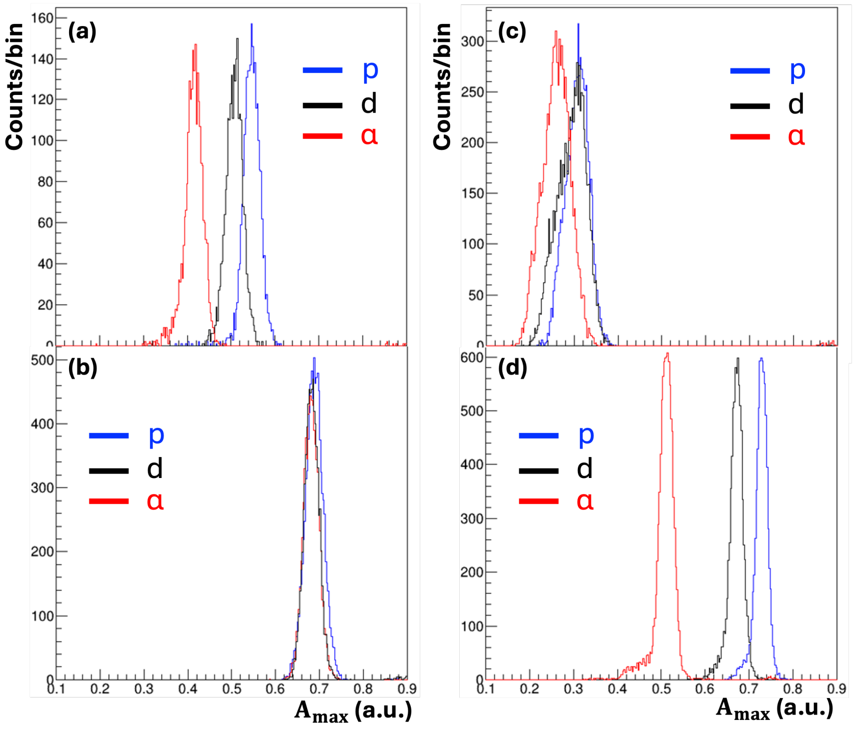

Figure 2.5.1: $A_{\max}$ Distributions of p, d, and α particles obtained from four setups shown in Table 2.1.

Table 2.3: $R_{x/y}$ obtained from four setups shown in Table 2.1.

	$R_{p/\alpha}$	$R_{d/\alpha}$	$R_{p/d}$
(a)	1.76	1.18	0.55
(b)	0.09	0.01	0.09
(c)	0.42	0.28	0.09
(d)	4.05	2.89	1.14

2.6 Evaluation of PSD Method for Low-Energy Particles

In the measurements conducted at the Kobe University tandem electrostatic accelerator facility, the optimal setup conditions for PSD were determined using 3 MeV p, d, and α particles. Subsequently, waveform information of charged particles with continuous energies below 6 MeV was acquired, and the PID capability was evaluated using the PSD method. In this measurement, p, d, t, and α particles with continuous energies emitted from the breakup reaction of ^{11}B + ^{12}C were detected by Si detectors, and waveforms were recorded.

2.6.1 Experimental Setup

The experiment was conducted from November 3 to November 18, 2020, in the 4th target room at the Cyclotron and Radioisotope Center (currently the Advanced Quantum Beam Science Center) of Tohoku University. An ^{11}B beam accelerated to 85.9 MeV by the AVF cyclotron was irradiated onto a ^{12}C target with a thickness of 0.97 mg/cm^2 installed in the scattering chamber.

Since the beam energy was sufficiently high compared to the decay thresholds of p, d, t, ^{3}He, and α particles in ^{12}C, various nuclear particles were emitted through the breakup reaction. Two Si detectors were stacked and placed behind the target to acquire the labels of the detected particles by applying the E–ΔE method. The second detector was an NTD-Si detector, similar to the one used in Sec. 2.3.1, while the first detector was also an NTD-Si detector with a thickness of 100 µm. The Si detectors were arranged so that the particles were incident from the rear surface. The output signals were amplified by the MPR-16 and sent to the V1730SB digitizer. A trigger was generated when a signal was detected on the rear surface of the second Si detector, and waveforms for each strip were recorded for 8 µs.

2.6.2 Analysis and Results

PID using the E–ΔE method was conducted for PSD. The energy correlation of particles measured on the front surface of the two Si detectors is shown in Fig. 2.6.1(a). According to the energy correlation of the two Si detectors, p, d, t, and α particles up to 30 MeV were detected by the second Si detector. On the left side of each structures, events where particles penetrated both Si detectors are distributed.

For subsequent analysis, PSD was performed for low-energy patricle below 6 MeV measured by the second Si detector to prevent contamination from penetrating events. To exclude accidental coincidences, conditions were applied to the energy and position of the detected particles. Specifically, signals were considered to originate from the same particle if the absolute difference between the energy measured on the front surface E_f and the rear surface E_r of each Si detector was within 0.5 MeV. Furthermore, particles whose detection positions did not match the geometric conditions of the experimental setup were removed. Fig. 2.6.1(b) shows the E–ΔE correlation of the two Si detectors after appropriate event selection. The lines in the figure represent PID functions created to align with the correlation curves for p, d, t, and α particles. Events were selected where the absolute difference between dE and the PID function was within 0.2 MeV, and the particles were labeled as p, d, t, and α accordingly.

Next, the PID parameter A_max was calculated from the signal waveforms obtained by the second Si detector using Eq. (2.2). The correlation between energy and A_max for Ch 8 of the second Si detector is shown in Fig. 2.6.2. Figure 2.6.3 shows the distribution of A_max and the average waveforms of each particle type at energies $E = 3.0$, 2.0, and 1.5 MeV for the Si detector. In the energy region below 6 MeV, the event count for d and t particles is fewer than 100 counts per 0.2 MeV, resulting in large statistical errors. Therefore, only the data for p and α particles were used to evaluate the separation performance.

At $E = 3.0$ MeV, a separation performance comparable to that in Fig. 2.5.1 was achieved. However, as the energy decreases, the separation performance degrades. In the energy region below 2 MeV, the peaks of p and α particles increasingly overlap, leading to a significant deterioration in separation power. In general, as particle energy decreases, the effect of noise increases and separation power decreases. Furthermore, the difference between the average waveforms of p and α particles decreases with decreasing energy. At $E = 1.5$ MeV, there is almost no discriminable difference between the waveforms of these particles. At lower particle energies, the difference in the range of each particle species in the Si detector is smaller, and consequently the difference in the electric field at the stop position is also smaller. For this reason, no difference in particle waveforms was observed at low energies. Therefore, for the experimental setup used in this study, it was concluded that PSD using the PID parameter A_{max} can accurately separate p and α particles down to an energy threshold of approximately 2 MeV.

2.7 Summary of PSD development

In this chapter, PSD method for Si detectors were developed as a new PID method to replace the E–ΔE and the time-of-flight (ToF) method. By exploring experimental setups with great PID capability for low-energy light particles, it was found that injecting particles from the rear surface of NTD-Si detectors is essential for PSD. Furthermore, it was determined that using a preamplifier with a wide frequency bandwidth and high sensitivity to differences in the current signals from the Si detector for each particle type is crucial.

In the experimental setup used in this study, sufficient separation of p and α particles was achieved down to 2 MeV. However, using a preamplifier with faster response characteristics could enable particle identification in lower energy regions, indicating that further development is necessary.

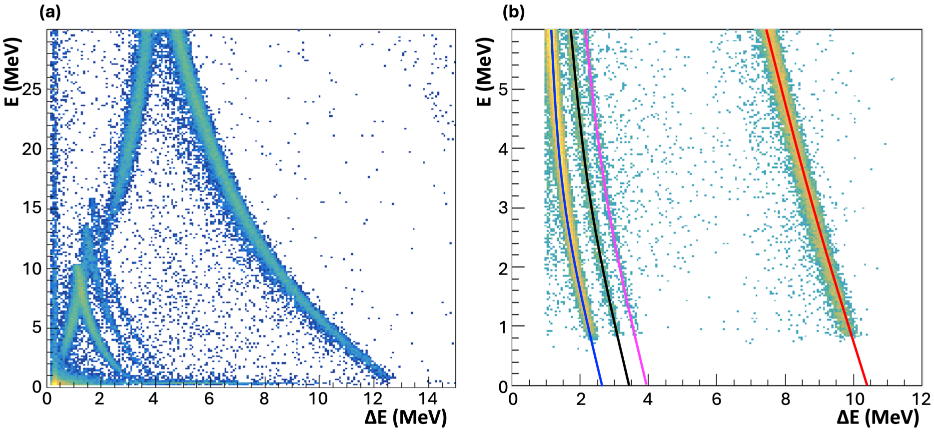

Figure 2.6.1: (a) Energy correlation measured at Ch 8 on the front surface of the two Si detectors. (b) Energy correlation after appropriate event selection. Events around each PID function are labeled as p, d, t, and α particles.

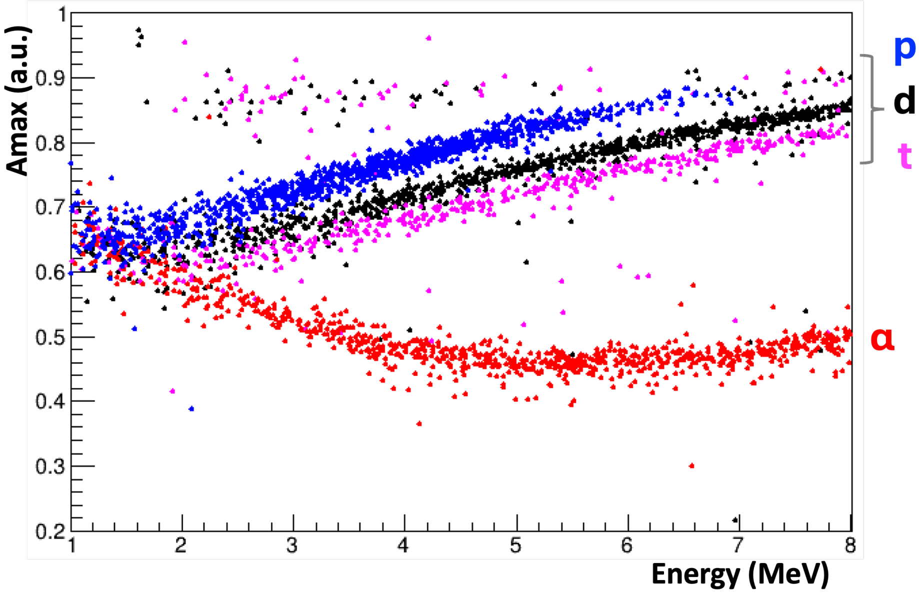

Figure 2.6.2: Correlation between energy and A_{max} in the second Si detector. The color of the dots corresponds to the colors of PID function shown in Fig. 2.6.1(b).

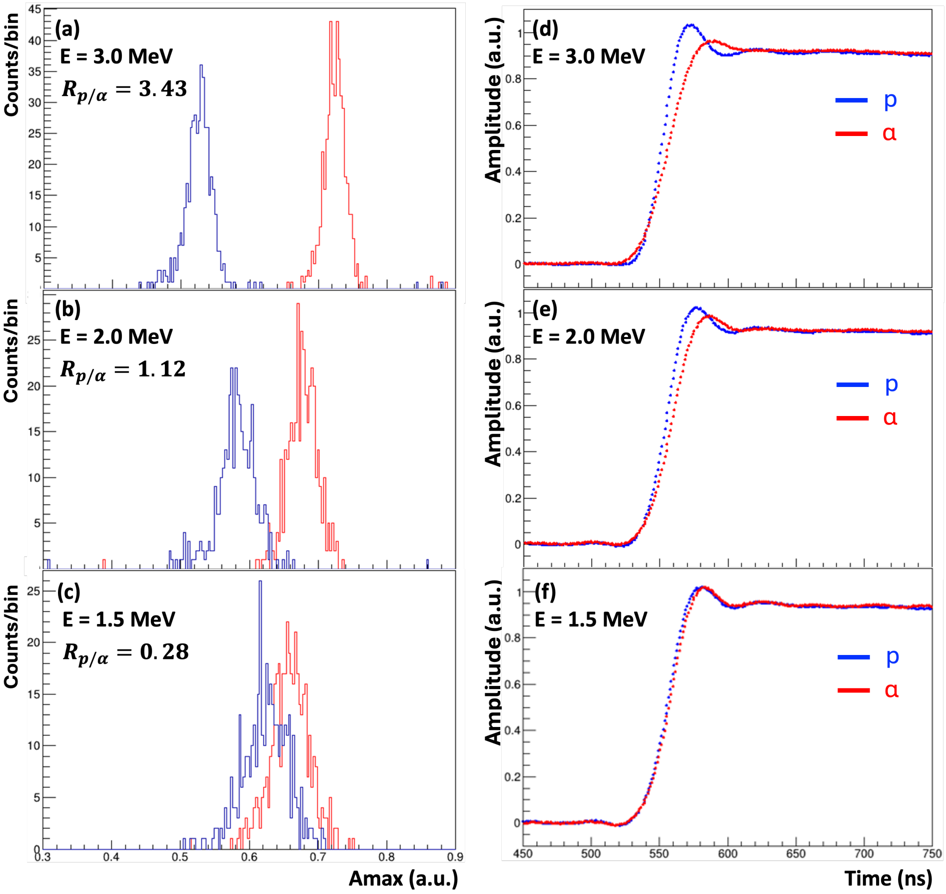

Figure 2.6.3: (a) the distribution of $A_{\max}$ and (b) the average waveforms of each particle type at energies $E = 3.0$, 2.0, and 1.5 MeV for the Si detector.

Chapter 3

Experiment

To determine the γ-decay probability from the Hoyle state, we conducted a coincidence measurement of scattered α particles, recoil ^{12}C, and decay γ-rays. A $^{4}\mathrm{He}^{2+}$ beam at 25.0 MeV was irradiated to a natural C target, and emitted charged particles were detected using a Si detector, while γ-rays were detected using the LaBr$_3$:Ce and CeBr$_3$ array (ROSPHERE). Signal waveforms from the Si detectors were acquired with digitizers, and particle identification was performed with the waveform analysis described in Chap. 2.

3.1 Facility and beamline

The experiment was conducted at the Horia Hulubei National Institute for R&D in Physics and Nuclear Engineering (IFIN-HH) in Romania [46]. Figure 3.1.1 shows the tandem accelerator facility at IFIN-HH. A negative ion beam extracted from the duoplasmatron ion source is accelerated by a terminal voltage of up to 9 MV applied to the high voltage terminal located at the center of the tandem accelerator. After conversion to positive ions via a charge stripper at the terminal, the beam is further accelerated. This beam is delivered to one of the seven beamlines following selection by an analyzing magnet. In this experiment, a $^{4}\mathrm{He}^{2+}$ beam at 25.0 MeV was extracted by applying a terminal voltage of 8.33 MV. The $^{4}\mathrm{He}^{2+}$ beam was transported to the scattering chamber on beamline 1, where the $^{12}\mathrm{C}(^{4}\mathrm{He},\alpha^{12}\mathrm{C}\gamma)$ reaction was measured using a detection system described later. Since the tandem accelerator produces a DC beam, a reduction of accidental coincidences is expected compared to measurements using RF accelerators.

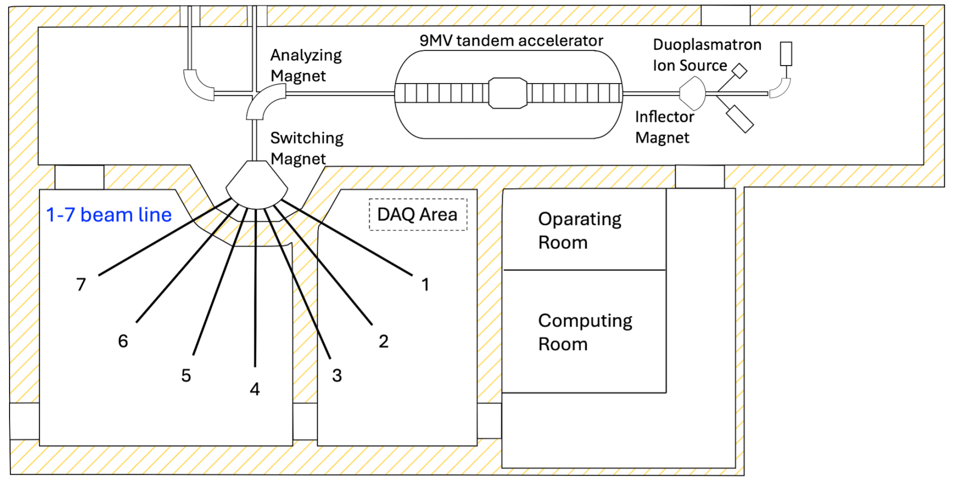

Figure 3.1.1: Schematic view of the tandem accelerator facility at IFIN-HH

3.2 Setup around Scattering chamber

Figure 3.2.1 provides an overview of the experimental setup. A $^4\mathrm{He}^{2+}$ beam at 25.0 MeV was irradiated to the $^{\mathrm{nat}}\mathrm{C}$ target, and emitted charged particles were detected using the Si detector, while γ-rays were detected using the $\mathrm{LaBr_3}$:Ce and $\mathrm{CeBr_3}$ array (ROSPHERE). The details of each component of the setup are described below.

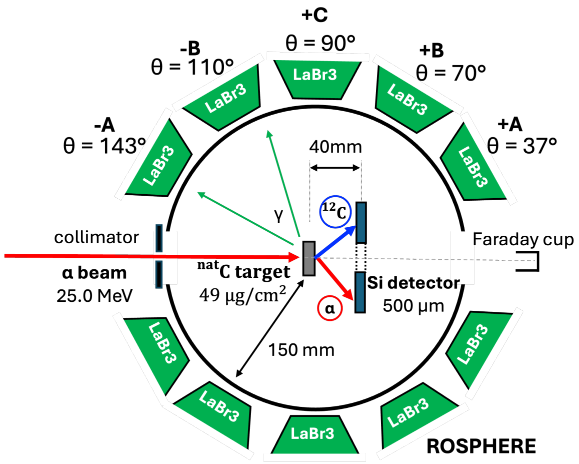

Figure 3.2.1: Overview of the experimental setup

3.2.1 Target

In this experiment, a target ladder as shown in Fig. 3.2.2 was prepared to allow for easy target changes during the beamtime. The ladder holds five target cells. Each cell is sized at 13 mm × 25 mm, with a 10 mm diameter hole at the center. For the primary measurements, a natural carbon ($^{\rm nat}$C) target with a thickness of 49 µg/cm^2 was employed. Since $^{\rm nat}$C contains approximately 1% of the ^{13}C isotope, a ^{13}C target with a thickness of 30 µg/cm^2 was used to subtract the ^{13}C background contributions. An empty cell (without a mounted target) was also employed to evaluate the background originating from sources other than the target. Furthermore, a plastic scintillator was mounted on the ladder as a viewer for beam tuning before and during beamlime.

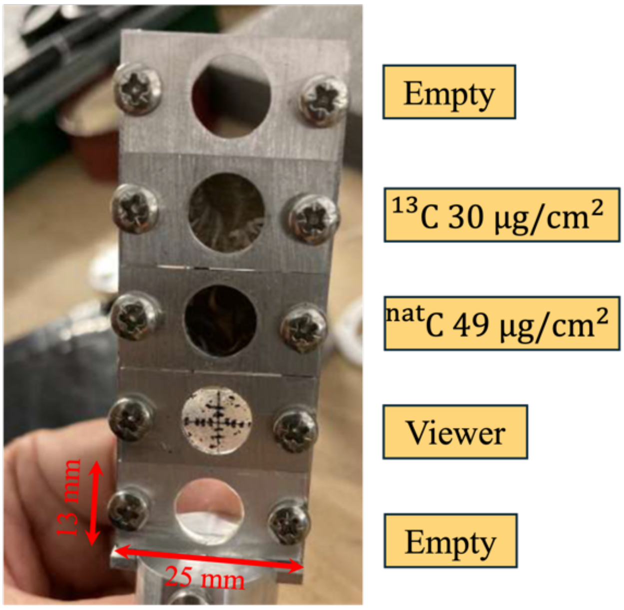

Figure 3.2.2: Target ladder used in the experiment. Measurements were conducted by switching between $^{\rm nat}$C, ^{13}C, and empty targets.

3.2.2 Si detector

Scattered α particle and recoil ^{12}C were measured with a ring-shaped double sided Si strip detector (DSSD) Design S1 by Micron Semiconductor Ltd. shown in Fig. 3.2.3. The inner and outer radii of the sensitive area are 24 mm and 48 mm, respectively, while the thickness is 500 µm. The junction side of the detector is divided into 4 sector-shape segments (segment 0–3) with a central angle of 90°, and each segment is divided into 16 arc-shaped strips with a pitch of 1.5 mm. On the other hand, the ohmic side is separated into 16 radial sectors. These radial sectors were treated as segment 4 in the analysis. The DSSD was placed at 40-mm downstream of the target covered $\theta_{\mathrm{lab}} = 31.0^\circ$–$50.2^\circ$ and its ohmic side faced the target for PSD. The arc-shaped strips on the junction side were connected to read-out connectors on the PCB board via narrow readout lines fabricated on wedge-shaped regions on the detector surface. Therefore, when charged particles hit the wedge-shaped regions, their positions cannot be measured correctly. This effect was accounted for in the detection efficiency simulations conducted in Chap. 4.

The leakage current of the DSSD was continuously monitored during beamtime. At the beginning of the beamtime, a voltage of +170 V was applied to the ohmic side of the DSSD, and the leakage current was approximately 5 µA. However, this current gradually increased to around 8 µA after the three-day measurement. This increase in leakage current caused a voltage drop due to the resistor inside the preamplifier, which reduced the effective voltage applied to the DSSD. To compensate for this, the applied voltage was increased to +180 V in the latter part of the beamtime. After that, the leakage current stabilized around 8 µA with small fluctuations.

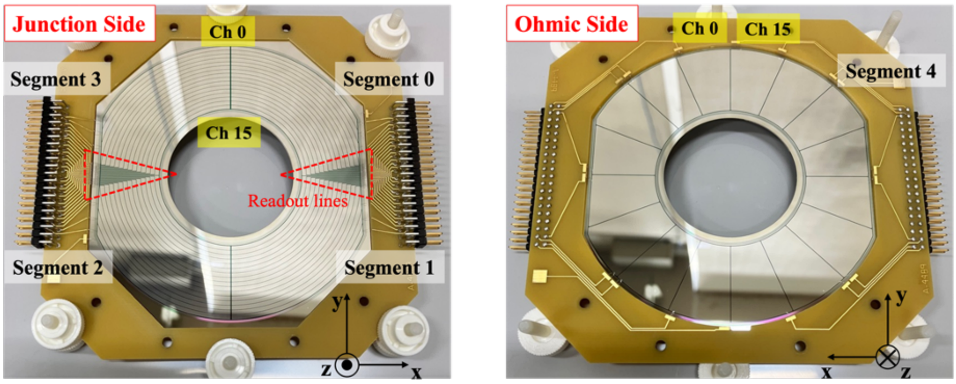

Figure 3.2.3: Schematic view of the DSSD Design S1. The segment and channel identification number of each strip was defined as shown in the figure.

3.2.3 ROSPHERE

The ROmanian array for SPetroscopy in HEavy ion REactions (ROSPHERE) [47] is the large γ-ray detectors array installed in Beamline 1 at the Tandem Accelerator Facility. ROSPHERE can be install up to 25 $\mathrm{LaBr_3}$:Ce and $\mathrm{CeBr_3}$ units. Figure 3.2.4 shows the structure of each units. This detector uses cylindrical $\mathrm{LaBr_3}$:Ce and $\mathrm{CeBr_3}$ crystals with a diameter of 76 mm and a height of 76 mm, coupled with PMTs manufactured by Hamamatsu. The crystals are shielded by two types of BGO detectors named Canberra and Ortec. These BGO consists eight BGO crystals, each connected to a PMT, but there readout lines are combined into one. The BGO shield works as a Compton suppressor to eliminate unwanted γ rays that are not fully absorbed by the $\mathrm{LaBr_3}$:Ce and $\mathrm{CeBr_3}$. Unfortunately, in this experiment, the energy threshold for the BGO signal was set at about 0.8 MeV, which prevented the detection of 511–keV γ rays emitted from electron-positron pair production by high-energy γ rays. Therefore, the BGO data was not used in this analysis.

14 $\mathrm{LaBr_3}$:Ce and 10 $\mathrm{CeBr_3}$ units were employed in the experiment. Table 3.2.3 shows the configuration of each unit used, and Figure 3.2.3 presents an overall view of ROSPHERE modeled with Autodesk Fusion 360. CAD files for all components used in ROSPHERE were prepared and used for simulation in Geant4 [48].

3.2.4 Scattering chamber

For this experiment, a scattering chamber was constructed using a cylindrical SUS frame with a width of 106 mm and a diameter of 220 mm, along with two hemispherical aluminum lids. Figure 3.2.6 shows an cross-sectional side view of the scattering chamber and equipment designed for this experiment. The scattering chamber was designed to be as compact as possible in order to increase the solid angle of ROSPHERE.

The $^4\mathrm{He}^{2+}$ beam was irradiated to the target through a cylindrical collimator with an aperture of 3 mm and a length of 83 mm, positioned upstream of the scattering chamber. To monitor the beam spot, a web camera was installed inside the scattering chamber. This setup enables real-time monitoring of the beam position on the viewer without opening the scattering chamber.

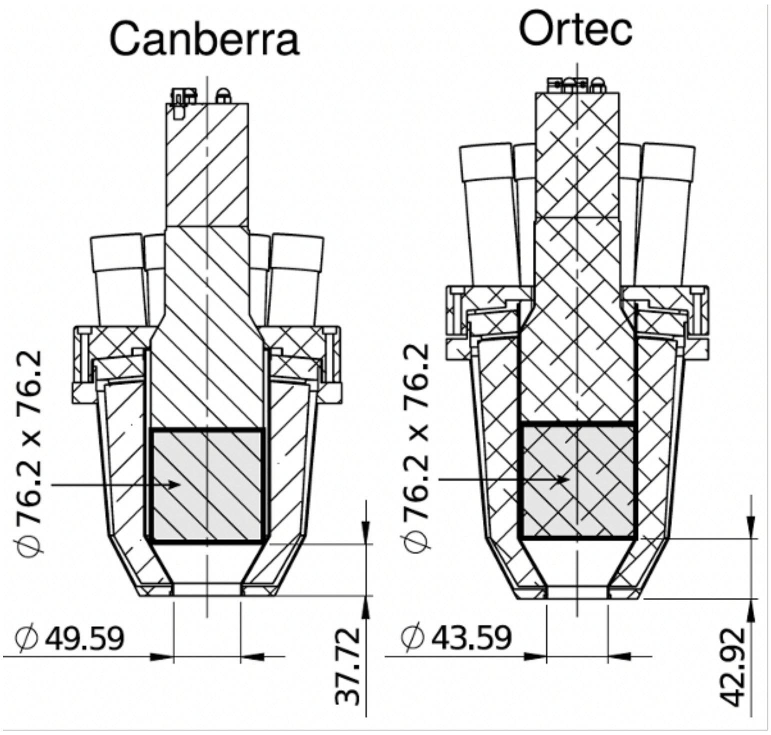

Figure 3.2.4: Schematic view of the detector units. $LaBr_3$:Ce and $CeBr_3$ crystals are covered by two types of BGO shields. Taken from Fig. 1 of Ref. [47].

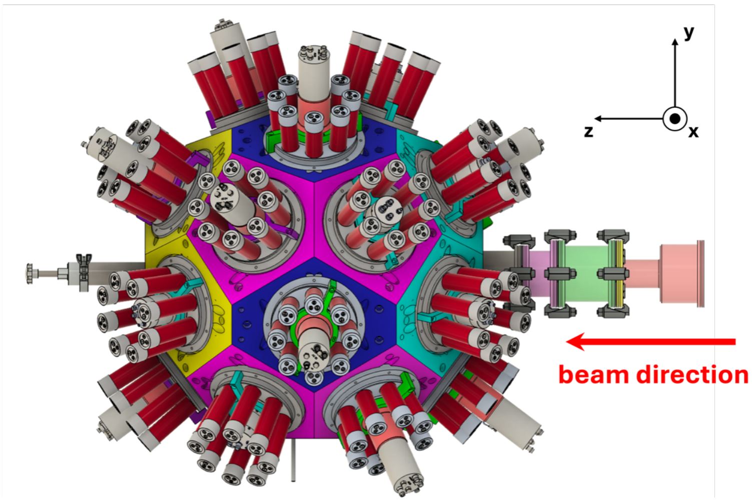

Figure 3.2.5: 3D model of the ROSPHERE assembly, created using Autodesk Fusion 360.

ID	Name	Type	BGO	θ (°)	ϕ (°)	$d_{t-\mathrm{det}}$ (mm)
1	+A1	$LaBr_3$:Ce	Ortec	37	0	174.7
2	+A2	$CeBr_3$	Ortec	37	72	174
3	+A3	$LaBr_3$:Ce	Canberra	37	144	202.5
4	+A4	$LaBr_3$:Ce	Ortec	37	216	174.7
5	+A5	$CeBr_3$	Ortec	37	288	174
6	+B1	$CeBr_3$	Ortec	70	36	181
7	+B2	$LaBr_3$:Ce	Canberra	70	108	209.5
8	+B3	$LaBr_3$:Ce	Ortec	70	180	181.7
9	+B4	$LaBr_3$:Ce	Ortec	70	252	181.7
10	+B5	$CeBr_3$	Ortec	70	324	181
12	C2	$LaBr_3$:Ce	Canberra	90	288	200.5
13	C3	$LaBr_3$:Ce	Canberra	90	216	200.5
14	C4	$LaBr_3$:Ce	Canberra	90	144	200.5
15	C5	$LaBr_3$:Ce	Ortec	90	72	171.7
16	-B1	$LaBr_3$:Ce	Canberra	110	36	209.5
17	-B2	$CeBr_3$	Ortec	110	108	181
18	-B3	$CeBr_3$	Ortec	110	180	181
19	-B4	$CeBr_3$	Ortec	110	252	181
20	-B5	$CeBr_3$	Ortec	110	324	209.5
21	-A1	$LaBr_3$:Ce	Canberra	143	0	202.5
22	-A2	$LaBr_3$:Ce	Canberra	143	288	174
23	-A3	$CeBr_3$	Ortec	143	216	174
24	-A4	$LaBr_3$:Ce	Canberra	143	144	202.5
25	-A5	$CeBr_3$	Ortec	143	72	174

Table 3.1: Configuration of $LaBr_3$:Ce and $CeBr_3$ units. Polar angle θ, azimuthal angle ϕ, and distance from target to detector $d_{\mathrm{t-det}}$ of each unit were also tabulated.

Additionally, a target moving device was installed at the bottom of the scattering chamber to adjust the target position. The target position in the scattering chamber can be seamlessly adjusted with the insertion rod attached to the target ladder. For installing this target moving device, one LaBr3 unit at the bottom of ROSPHERE (ID:11) was removed.

Two Faraday cups were installed downstream of the DSSD. The first is a cylindrical Faraday cup with a length of 328 mm and an inner diameter of 30 mm, and further downstream, there is a disk-shaped Faraday cup with a diameter of 7 mm.

Downstream of the DSSD, a cylindrical Faraday cup with a length of 328 mm and an inner diameter of 30 mm, as well as a circular Faraday cup with a diameter of 7 mm, were installed. These two Faraday cups were electrically connected and the beam current was readout as a single unit in this experiment. The readout beam current was input to a current integrator, digitized, and converted into NIM signals. Then, the NIM signals were counted to measure the total beam current.

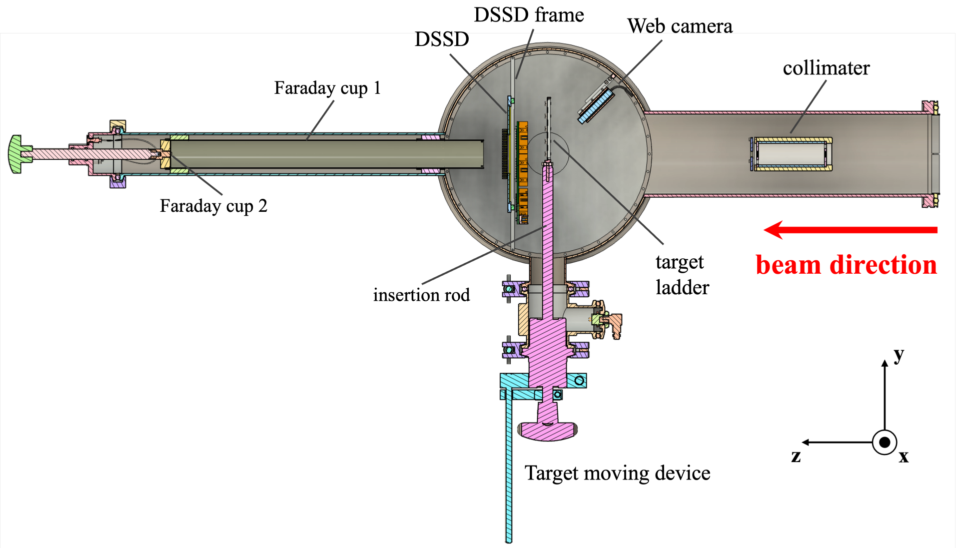

Figure 3.2.6: Cross-sectional side view of the scattering chamber and equipments.

3.3 Signal processing and data acquisition (DAQ) system

In this experiment, all data were acquired using flash digitizers only. Figure 3.3.1 shows a schematic diagram of the signal processing and DAQ system used in this experiment. Signals from the DSSD were amplified using Mesytec MPR-16 or MPR-32, and the differential signals from the preamplifier were converted into unipolar signals by Mesytec MDU-16. The unipolar signals were then input into channels 2 to 15 of six CAEN V1730SB 500 MS/s flash digitizers, and waveform data during 1,600 ns and timestamps were acquired using the DPP-PHA firmware commercially provided by CAEN. Meanwhile, the output signals from ROSPHERE were directly input into two V1730SBs, where the integral values of the waveforms and timestamps were recorded using the DPP-PSD firmware purchased from CAEN. Additionally, the NIM signals from the current integrator were input into the available channels of V1730SB.

The signal from segment 4 of the DSSD were splitted into two lines. One line is connected to V1730SB directly, and the other is to a Mesytec MSCF-16 module for generating time reference signals. MSCF-16 is a multi-channel shaping/timing amplifier with constant fraction discriminators. The threshold was set around 8 MeV to eliminate low-energy α particles emitted from the Hoyle state. Then, the 16 timing outputs were sent to a Programmable Logic Unit V2495, where the time reference signal was generated by combining the 16 timing signals through logical OR operation. The time reference signal was inputted to channel 0 (Ch 0) of each digitizer. In addition, the busy signals output from each digitizers for DSSD were input into V2495 for vetoing the time reference signal.

3.3.1 Data acuisition condition

DAQ for DSSD

Data size of the waveform data acquired by the digitizers is very large, which limits the event acquisition rate due to data transfer speed. To achieve high event acquitision rates in the experiment, it is necessary to reduce the data size per event. Although the DSSD has 80 strips, signals are only induced on several strips of them. Therefore, it is inefficient to acquire waveform data from all strips in response to one event.

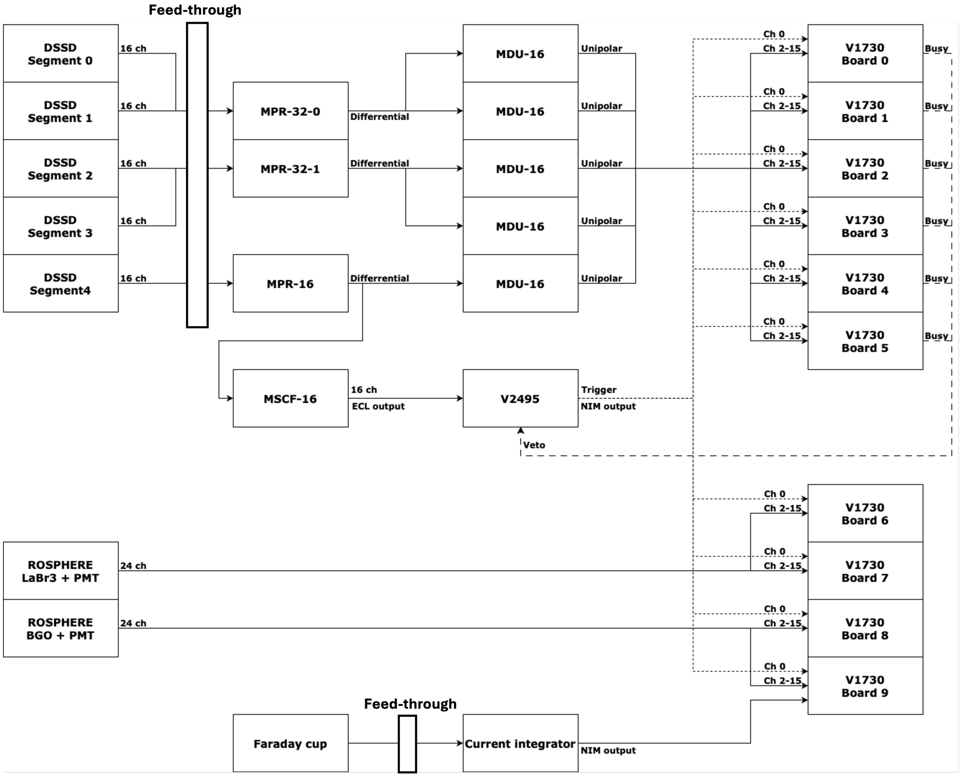

Figure 3.3.1: Schematic diagram of signal processing and DAQ system.

To solve this problem, self-trigger mode was implemented on the digitizers for the DSSD by the DPP-PHA firmware in this experiment. Each channel of the digitizer is equipped with a digital discriminator, which generates a self-trigger signal when the input signal exceeds a certain threshold value. The threshold value is remotely controlled, and set 0.5 MeV. When this self-trigger signal coincides with the time reference signal on Ch 0, the waveform of the corresponding channel was recorded. Coincidence window between Ch 0 and any channels was set within 2 µs.

In this configuration, when a particle of 8 MeV or higher was detected on the ohmic side, the waveform data of all channels where a particle of 0.5 MeV or higher hit were recorded.

DAQ for ROSPHERE

On the other hand, although self-trigger mode was also implemented on the digitizers for ROSPHERE, the coincidence requirement with Ch 0 was not applied. Consequently, all signals input to the DAQ for ROSPHERE, including the reference signal, were independently recorded for each channel. Synchronization of the acquired data between the DSSD and ROSPHERE could be confirmed by matching timestamps for the time reference signal input to Ch 0 (details are provided in Sec. 4.1). This asynchronous trigger system allows the spare channels on the digitizers to be used as scalers. The NIM signal from the current integrator was input into the digitizers and counted. The details of the firmware used in V1730SB are described in Appendix A.

3.4 Summary of the experiment

This experiment was conducted from May 22 to May 29, 2022, using ${}^{\mathrm{nat}}$C, ^{13}C, and empty targets. These targets were replaced in cycles of 6 hours, 1 hour, and 0.5 hours, respectively. Consequently, the total measurement time for the ${}^{\mathrm{nat}}$C target accumulated to 89 hours, with an average beam current of 1.1 pnA and an average DSSD event rate of 6 kHz. The average event rate for each $\mathrm{LaBr_3(Ce)}$ and $\mathrm{CeBr_3}$ detectors of ROSPHERE was 1.5 kHz.

The beam spot on the viewer was checked in each cycle to ensure beam spot stability. Figure 3.4.1 shows an image of the beam spot at the beginning of the experiment captured by the web camera. The beam spot displayed a rectangular shape about 2.5 mm in width and 1.5 mm in height. It was desirable for the beam spot size to be smaller than the 1.5 mm strip pitch of the DSSD, but due to the limited time available for beam tuning, a compromise had to be made. Therefore, the measurements were conducted while maintaining the spot shape and size of the beam spot throughout the beamtime.

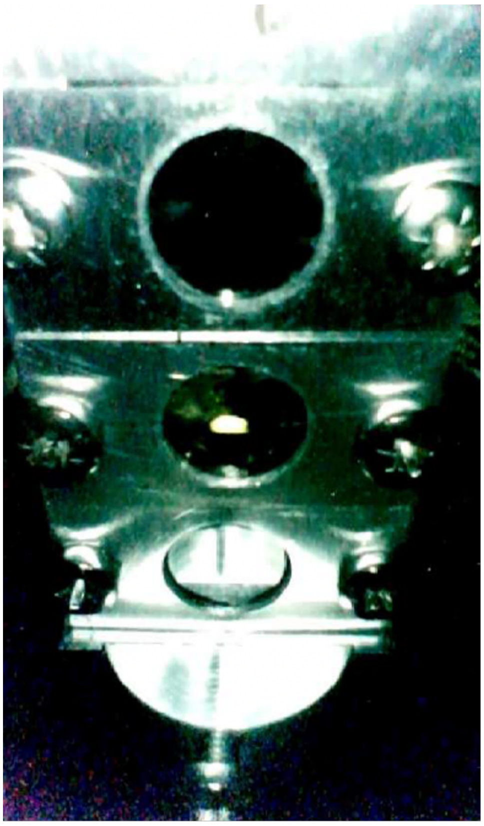

Figure 3.4.1: An image of the beam spot at the beginning of the experiment.

Chapter 4

Data analysis

As described in Sec. 3.3, signals from the DSSD and ROSPHERE were input into ten V1730SB modules, and the pulse height, waveform (only for the DSSD), and timestamp were recorded for each channel. Details of the firmware used in the V1730SB are described in Appendix A. Using the obtained information on energy, time, channel number, and waveform, coincidence events of scattered α particles and recoiled ^{12}C were selected, and the γ decay probability from the Hoyle state was determined using the ^{12}C-detection method. Furthermore, coincidence events of scattered α particles, recoiled ^{12}C, and γ rays were selected, and the γ decay probability from the Hoyle state was determined using the α+^{12}C+γ triple-coincidence method.

4.1 Event building

First, event building was performed using timestamps. In this experiment, time information was not acquired using a TDC. Instead, digital timing filter processing of the acquired signals was performed internally by the V1730SB, and the time information were output as timestamps. Therefore, all time information in this experiment was calculated using timestamps.

As described in Sec. 3.3.1, a common reference signal was input into Ch 0 of the V1730SB, and the coincidence of events among channels was selected using the timestamp difference t_{diff} between each channel and Ch 0. Figure 4.1.1 shows the time difference spectra of (a) the DSSD (Board 0–Ch 2) and the reference signal, and (b) the ROSPHERE (Board 6–Ch 2) and the reference signal. In Fig. 4.1.1(a), a peak due to true coincidence events is observed around 600 ns, with accidental coincidence events distributed around it. Events within 500 ns including this peak were built as the same event. On the other hand, in Fig. 4.1.1(b), a peak corresponding to true coincidence events was observed around −250 ns, and events within 300 ns including this peak were built. The triple peak structure observed here originates from differences in the types of particles incident on the DSSD.

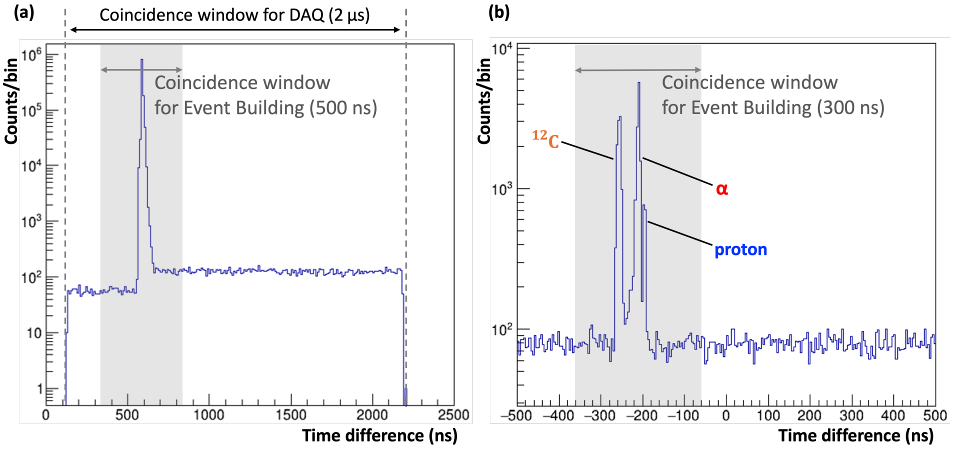

Figure 4.1.1: Time difference spectra of (a) the DSSD (Board 0–Ch 2) and the reference signal, and (b) the ROSPHERE (Board 6–Ch 2) and the reference signal

4.1.1 Time offset correction

It was found that the time information of the built data had different offsets for each channel. Figure 4.1.2(a) shows the distribution of the timestamp difference t_{diff} between all 64 strips on the junction side of the DSSD and the reference signal for particles with energies above the trigger threshold of 8 MeV. While the width of the distribution for each channel was around a few nanoseconds, the position of the distribution varied for each channel. Since the same reference signals were input into each board, the cause of the offset was assumed to exist in the digital signal processing of each channel. As the amplitude of this offset did not vary within a single run, time correction was performed assuming a constant delay for each channel. Figure 4.1.2(b) shows the t_{diff} distribution after correcting each channel so that the time corresponding to the peak became 0 ns. Since the amplitude of the offset varied randomly for each run, this time correction was applied to each run individually. As a result, the time resolution of the DSSD for particles above 8 MeV obtained in this experiment was 1.5 ns (sigma).

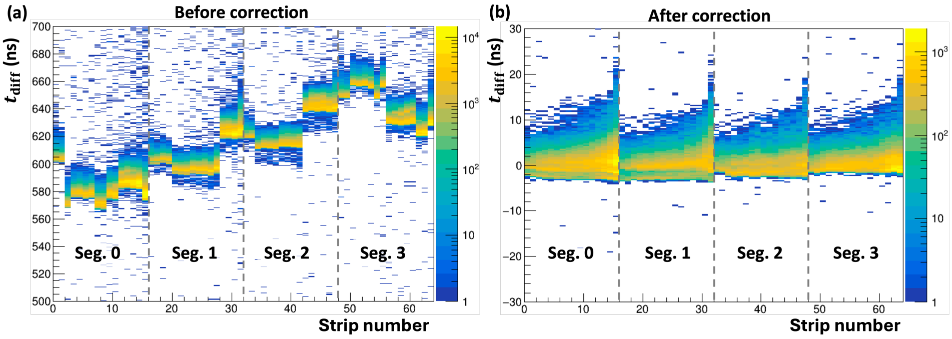

Figure 4.1.2: Distribution of the timestamp difference $t_{\rm diff}$ between all 64 strips on the junctionside of the DSSD and the reference signal. (a) Before offset correction, (b) After offset correction.

4.2 Data analysis of Si detector

4.2.1 Energy calibration

The energy calibration of the DSSD was performed using a triple mixed α source consisting of ^{239}Pu ($E_\alpha = 5.139$ MeV), ^{241}Am ($E_\alpha = 5.474$ MeV), and ^{244}Cm ($E_\alpha = 5.789$ MeV). The noise filtering process described in Sec. 2.4 was applied to the acquired waveforms, and the pulse height was used for energy calibration. Figure 4.2.1 shows the energy spectra of α particles emitted from the triple mixed α source measured using (a) all 64 strips on the junction side and (b) all 16 strips on the ohmic side of the DSSD. The energy resolution for the 5.139 MeV α particles emitted from ^{239}Pu was 16.9 keV on the junction side and 26.6 keV on the ohmic side. The energy resolution was worse on the ohmic side due to the larger sensitive area per channel and higher signal noise level compared to the junction side. During the experiment, the leakage current of the DSSD increased from approximately 5 µA to 8 µA by the middle of the beam time, leading to an adjustment of the bias voltage from 170 V to 180 V. Therefore, calibration data using the α source were acquired immediately after the beam time at both voltage settings.

A comparison of the pulse height of the ^{239}Pu α source in the two voltage settings showed that the gain shift of up to 7.1 keV.

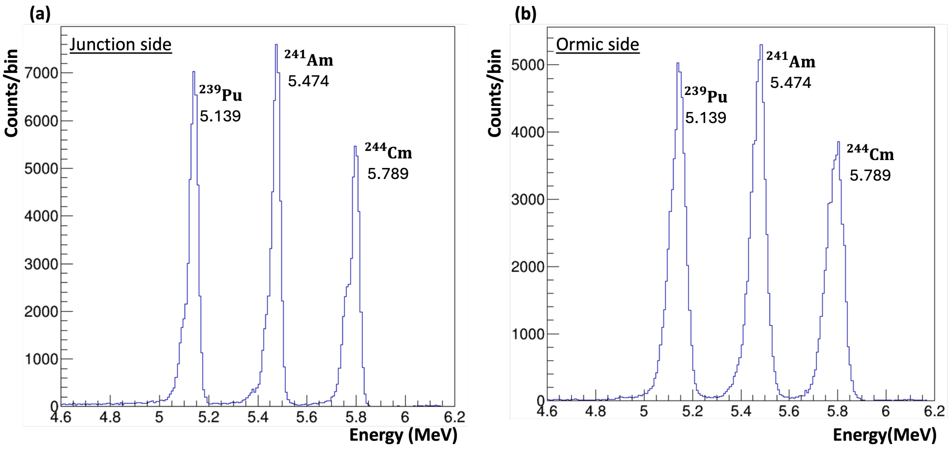

Figure 4.2.1: Energy spectra of α particles emitted from the triple mixed α source. (a) Sum of the 64 strips on the Junction side and (b) sum of the 16 strips on the ohmic side.

4.2.2 Determination of hit position

When a charged particle hit the DSSD, signals are induced on both the junction side and the ohmic side. By appropriately combining the signals from both sides, the detection position of the charged particle can be determined. The DSSD used in this experiment has the junction side divided into four fan-shaped segments with a central angle of 90 degrees. Each segment is further divided into 16 arc-shaped strips on the junction side and 4 strips on the ohmic side. Based on this structure, the hit position of the particle was determined by combining the signals from the junction and ohmic sides for each segment.

For a given segment, let N_{F} be the number of strips on the junction side where signals were induced, and $E_{\mathrm{F},i}$ be the energy obtained on the i-th strip ($1 \leq i \leq N_{\mathrm{F}}$). Similarly, let N_{R} be the number of strips on the ohmic side where signals were induced, and $E_{\mathrm{R},j}$ be the energy recorded on the j-th strip ($1 \leq j \leq N_{\mathrm{R}}$). The energies $E_{\mathrm{F},i}$ and $E_{\mathrm{R},j}$ are sorted in descending order. Since the ^{12}C(0_2^+) state excited by the ^{12}C(α, α' ^{12}C(0_2^+)) reaction almost entirely decays into three α particles [49–51], hit patterns with $N \leq 3$ were considered for the analysis. Figure 4.2.2 illustrates schematic examples of several hit patterns for segment 0. In the subsequent analysis, an event where N_F strips on the junction side and N_R strips on the ohmic side induced signals is referred to as an N_F–N_R event.

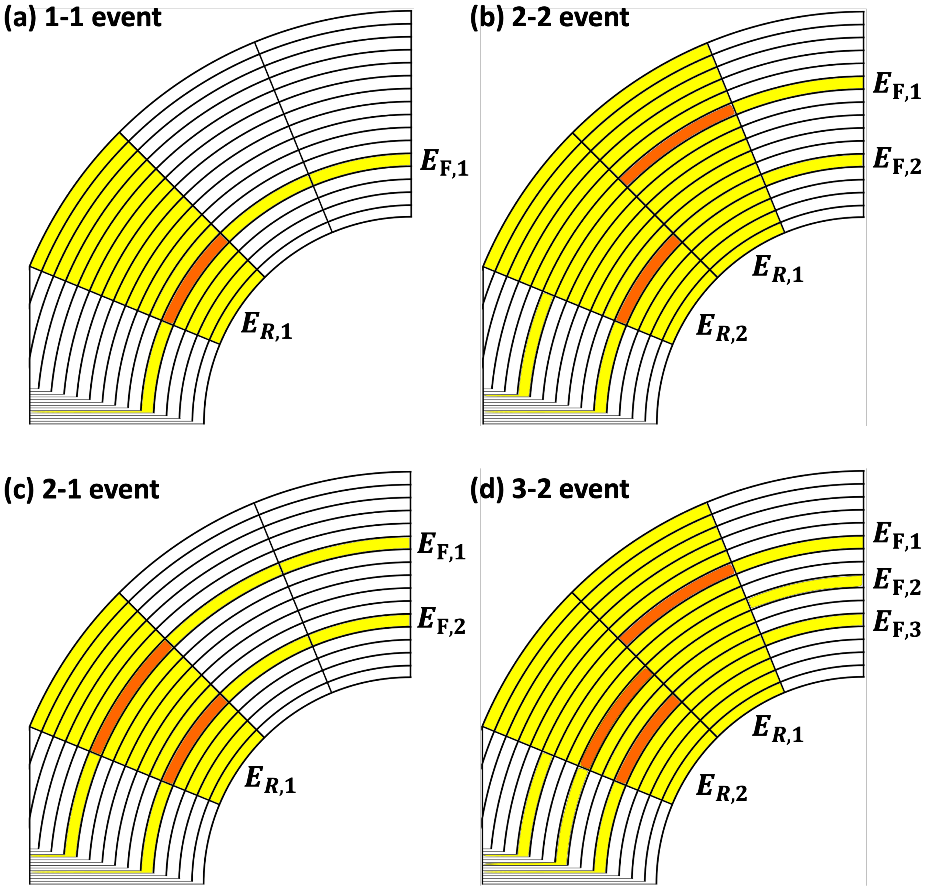

Figure 4.2.2: Examples of hit patterns when one or more particles entered segment 0. The pixels where particles hit and the strips where signals were induced are shown in orange and yellow, respectively.

1–1, 2–2, 3–3 event ($N_\mathrm{F}=N_\mathrm{R}$)

As shown in Figures 4.2.2(a) and (b), when the number of hit strips on the junction side and the ohmic side are equal, the N particles hit different strips. Under this condition, the energies detected on the junction and ohmic strips intersecting the pixel where the particle hit should match. Figure 4.2.3 shows the correlation of the energies detected on individual strips for (a) 1–1 events and (b) 2–2 and 3–3 events on the junction and ohmic sides. Since the energies $E_{\mathrm{F},i}$ and $E_{\mathrm{R},j}$ are sorted in descending order, the strips can be paired sequentially. In Fig. 4.2.3(a), a continuous distribution up to the beam energy of 25.0 MeV is observed, while in Fig. 4.2.3(b), many low-energy particles below 6 MeV are detected. These low-energy particles correspond to α particles originating from the α decay of the $^{12}\mathrm{C}(0_2^+)$ state. The coincidence condition was set as :

$$|E_{\mathrm{F},i} - E_{\mathrm{R},j}| < 0.3\,\mathrm{MeV}, \tag{4.1}$$

considering the energy resolution of the DSSD. This condition was applied to each of the N particles, and only events satisfying all conditions were selected. As a result, 1.9% of all 1–1 events and 6.1% of all 2–2 and 3–3 events were rejected.

The characteristic structure shown in the red box in Fig. 4.2.3(a) corresponds to events occurring only on Ch 0 and Ch 15 of each segment on the junction side. Since the DSSD used in this experiment did not have a guard ring, it is possible that a sufficient electric field was not formed at the edges of the detector, leading to incorrect energy readings for the particles. All these events were excluded from the data analysis by the condition described in Eq. (4.1).

2–1, 3–1, 1–2, 1–3 event

As shown in Fig. 4.2.2(c), when multiple particles hit a single strip on one side, the total energy on the junction side and the total energy on the ohmic side should match. Figure 4.2.3(c) shows the correlation between the total energy on the junction side and the total energy on the ohmic side for 2–1 and 3–1 events. Considering that the total energy on the junction side (or ohmic side) corresponds to the sum of the energies of multiple particles for 2–1 and 3–1 events (or 1–2 and 1–3 events), the coincidence condition was set as :

$$|\sum_{i=1}^{N_F} E_{\mathrm{F},i} - E_{\mathrm{R},1}| < 0.6\,\mathrm{MeV} \tag{4.2}$$

$$|E_{\mathrm{F},1} - \sum_{j=1}^{N_R} E_{\mathrm{R},j}| < 0.6\,\mathrm{MeV}. \tag{4.3}$$

As a result, 3.7% of the 2–1, 3–1, 1–2, and 1–3 events were excluded from the analysis.

In the case of 2–1 and 1–2 events, a continuous structure shown in the red box in Fig. 4.2.3(c) was observed in the energy range E = 16–18 MeV and 20–22 MeV, corresponding to the ground state and second excited state of ^{12}C. These events are considered to be misidentified as 2–1 or 1–2 events due to partial energy deposition in neighboring strips when particles hit near the boundary of each strip in the DSSD. Therefore, among the events satisfying the condition in Eq. (4.2), those in which signals were induced across neighboring strips on the junction side (or the rear side) and whose energy corresponded to the ground or excited states of ^{12}C were treated as single-particle events (1–1 events) in the subsequent analysis.

3–2, 2–3 event

As shown in Fig. 4.2.2(d), when three signals were detected on one side and two signals on the other side, multiple combinations of hit positions for the three particles were possible. Therefore, the energy ordering alone could not uniquely determine the combination of strips where the three particles hit.

As the initial coincidence condition, the total energy on the junction side and the total energy on the ohmic side were required to match. Figure 4.2.3(d) shows the correlation between the total energies on the junction and ohmic sides. The coincidence condition was set as :

$$|\sum_{i=1}^{N_F} E_{\mathrm{F},i} - \sum_{j=1}^{N_F} E_{\mathrm{R},j}| < 0.9\,\mathrm{MeV} \tag{4.4}$$

Among the three particles, one particle should be classified as a 1–1 event, while the remaining two particles should be classified as a 2–1 (or 1–2) event. The junction and ohmic hit strips were paired using the following procedure :

1. Select any one signal from the junction side and any one signal from the ohmic side, and apply the coincidence condition in Eq. (4.1).
2. Combine the remaining two signals on the junction (or ohmic) side with the remaining one signal on the ohmic (or junction) side, and apply the coincidence condition in Eq. (4.2) (or Eq. (4.3)).

Among the all six combinations of junction and ohmic strips, the one that satisfied both conditions was adopted. However, if multiple combinations satisfied the conditions, the event with the smallest energy difference on the left side of Eq. (4.2) was selected. As a result, 3.8% of the 3–2 and 2–3 events did not satisfy both conditions and were excluded from the analysis.

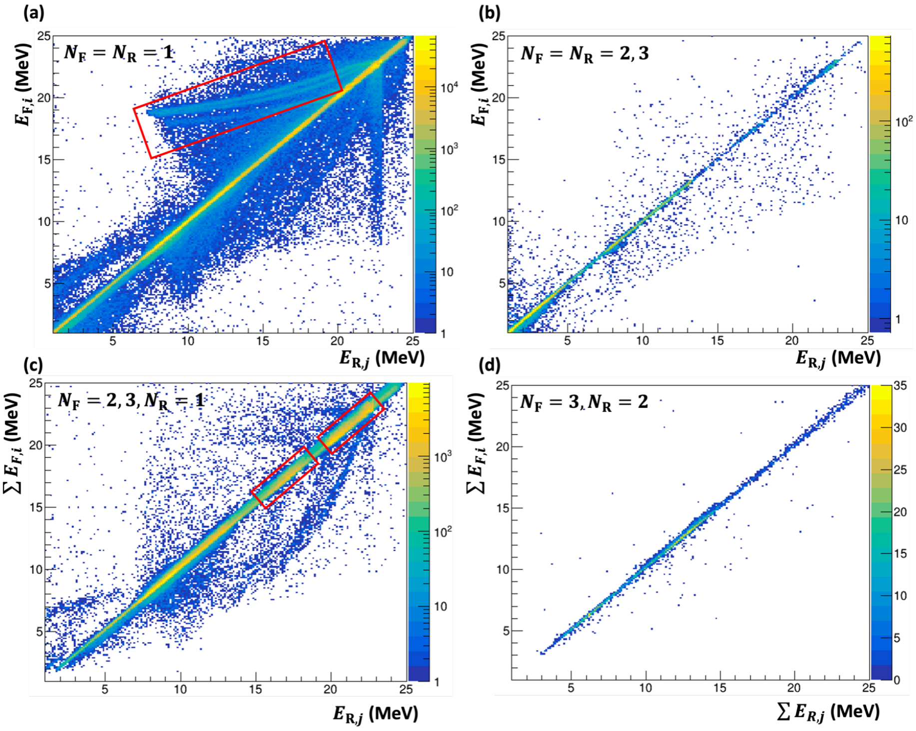

Figure 4.2.3: Energy correlations between the junction and ohmic sides for various hit patterns: (a) 1–1 event, (b) 2–2, 3–3 event, (c) 2–1, 3–1 event, (d) 3–2 event.

4.2.3 Particle identification with PSD

The waveforms output from the DSSD were recorded using a digitizer with a sampling rate of 500 MHz for a duration of 1600 ns. To perform particle identification, the identification parameter $A_{\max}$ was calculated from the acquired waveforms using the method described in Sec. 2.4. Figure 4.2.4 shows the correlation between the energy and $A_{\max}$ for Segment 0–Ch 8 on (a) the junction side and (b) the ohmic side. Similar structures were obtained on both sides, and the events inside the colored boxes were identified as protons and deuterons (blue), α particles (red), and ^{12}C (orange). However, previous studies have reported that even when using NTD-Si, it was impossible to distinguish α particles and ^{12}C below 6 MeV [52]. In the black box region of the figure, the discrimination between α particles and ^{12}C could not be achieved. The trigger threshold for this experiment is shown by the gray dashed line in Fig. 4.2.4(b). The CFD threshold of the MSCF-16 was set so that only α particles with energies above 8 MeV would trigger the data acquisition. However, due to waveform differences among particle types, the pulse height of the fast signal generated within the MSCF-16 varied, effectively shifting the trigger threshold depending on the particle type.

In the region above 8 MeV, a discrete structure originating from scattered α particles emitted from the target was observed, with the corresponding ^{12}C states indicated by the arrows in Fig. 4.2.4(b). The continuous locus in the higher A_{max} region above this discrete structure corresponds to background events caused by beam particles scattered by the upstream collimator. Although these background particles are also α particles, they hit the DSSD at a smaller angle than the scattered α particles from the target, resulting in shorter signal rise times and increased A_{max} values.

To select scattered α particles, PID functions represented by the red dashed lines in Fig. 4.2.4(a) were created for each strip and used in the coincidence analysis described in Sec. 4.4.3. The particles within the black box correspond to signals of the particles emitted from excited states of ^{12}C, and detected in coincidence when inelastically scattered α particles from the target triggered the data acquisition. Since the energy of α particles emitted from the excited states of ^{12}C and the ground state ^{12}C emitted after γ decay is below 6 MeV, the waveform analysis method used in this experiment could not distinguish between them. However PID functions represented by the black dashed lines in Fig. 4.2.4(a) were created for each strip to differentiate the ^{12}C and α particles from other particles, and used in the analysis described in Sec. 4.4.3.

As described in Sec. 3.2.2, the leakage current of the DSSD increased during the first half of the beam time, leading to an increase in the applied bias voltage during the latter half of the experiment. Since the waveform characteristics of each particle are changed by both the applied bias voltage and leakage current, the correlation between A_{max} and energy was monitored during the experiment to keep it as stable as possible by adjusting the bias voltage. In the offline analysis, a PID function was generated for each run to correct for the shift in A_{max} values, and the corrected A_{max} value was defined as A'_{max}.

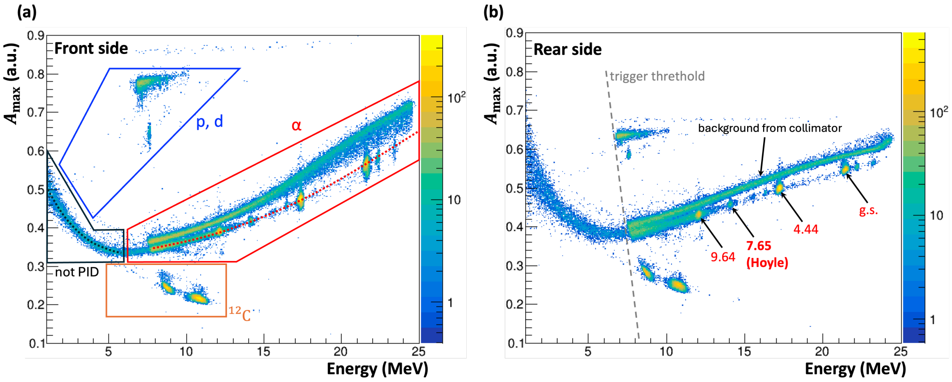

Figure 4.2.4: Correlation between A_{max} and energy on the (a) junction side and (b) ohmic side.

4.2.4 Energy spectrum obtained by DSSD

Figure 4.2.5(a) shows the energy spectrum obtained from all 16 strips of segment 0 for events identified as scattered α particles. Since the junction side of the DSSD is divided concentrically, the strip number on the horizontal axis corresponds to the scattering angle of the α particles. In the energy spectrum from Ch 8 shown in Fig. 4.2.5(b), peaks corresponding to scattered α particles from the ground and excited states of ^{12}C were observed. Additionally, multiple peak structures were observed, which are considered to correspond to scattering from ^{13}C, ^{16}O, and ^{27}Al. These impurities are suspected to have contributed to the spectrum due to the following reasons:

1. Scattering from the 1% ^{13}C contained in the $^{\mathrm{nat}}$C target.
2. Scattering from H_2O adsorbed on the surface of the $^{\mathrm{nat}}$C target.
3. Scattering from the edge of the target cell made of ^{27}Al due to the beam halo.

The $5/2^-$ state of ^{13}C (E_x = 7.67 MeV) and the 2^- state of ^{16}O (E_x = 8.87 MeV) have scattered α particle energies that are very close to the Hoyle state of ^{12}C at specific scattering angles, making it difficult to distinguish kinematically. Therefore, for the ^{13}C impurity, background subtraction was performed using the measurement from a ^{13}C target. For the ^{16}O impurity, coincidence events with recoil particles were selected, and background events were eliminated based on the energy of the recoil particle. Since the contribution from ^{27}Al impurities was minimal, it was not considered in the analysis. The details of the background event subtraction procedure are described in Sec. 4.4.3.

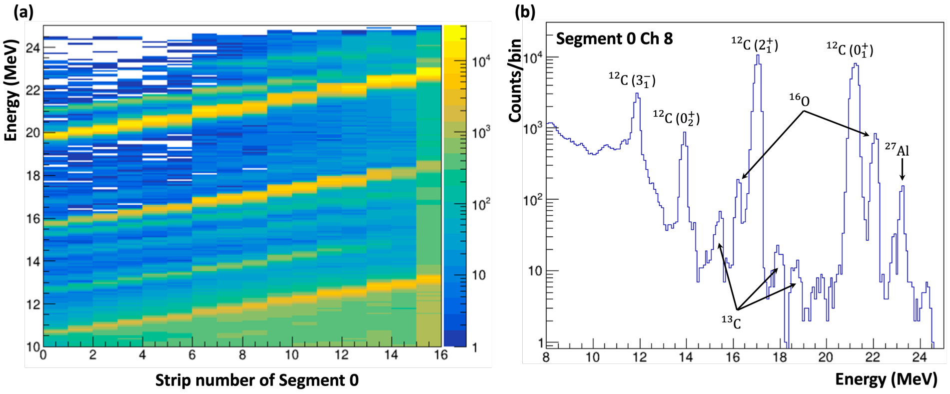

Figure 4.2.5: (a) Energy spectrum obtained from each strip of segment 0 and (b) energy spectrum obtained from Ch 8.

4.2.5 Correction of beam position on target

Based on the measured energies and hit positions of the scattered α particles, the excitation energy of the recoiled ^{12}C was calculated using the kinematics of α+^{12}C scattering. For this calculation, the energy measured on the junction side, which has relatively better energy resolution, was used. The particle's position was determined using the central coordinates of each matrix of the DSSD.

The excitation energy spectra obtained from each strip on the ohmic side are shown in Fig. 4.2.6(a). The peak energy varies across different strips, indicating a position-dependent effect. Since the strips on the ohmic side are divided radially, if the beam position on the target coincides with the center of the DSSD, the strips should be rotationally symmetric, and the excitation energies should match. However, the observed shifts in excitation energy suggest that the alignment between the beam axis and the DSSD was not perfectly accurate or that the beam position on the target shifted during the beam time.

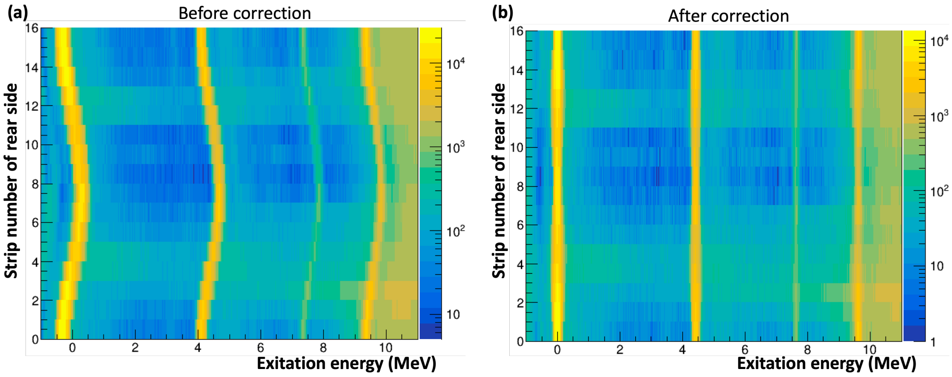

Figure 4.2.6: Excitation energy spectra obtained from each strip on the ohmic side (a) before and (b) after correcting the beam center position.

To determine the actual beam center position, a detailed analysis was conducted. Figure 4.2.7(a) shows a schematic view of the DSSD as seen from upstream of the beam. Assuming the center of the DSSD as the origin, the beam center position (x, y) was systematically shifted within the range of $x = -5.0$ to $+5.0$ mm and $y = -5.0$ to $+5.0$ mm with a step size of 0.1 mm. For each shift, the excitation energy of the ohmic side strips relative to junction side Ch 8 was calculated. The difference in excitation energy among the strips, E_{diff}, was then defined using Eq. (4.5).

$$E_{\text{diff}} = |E_{x,0} - E_{x,3}| + |E_{x,4} - E_{x,7}| + |E_{x,8} - E_{x,11}| + |E_{x,12} - E_{x,15}| \tag{4.5}$$

Here, $E_{x,i}$ represents the excitation energy calculated using junction side Ch 8 and ohmic side Ch i. For a one-hour run during the beam time, the values of E_{diff} calculated for various beam positions are shown in Fig. 4.2.7(b). In this figure, the magnitude of E_{diff} is plotted along the z-axis, and the beam center position during this run was determined as $(x, y) = (0.20\,\text{mm}, 2.49\,\text{mm})$, where E_{diff} was minimized. Beam position analysis was conducted for a total of 83 runs, and no systematic variations in the beam position were observed during the beam time. Therefore, we determined that the excitation energy deviations were due to alignment errors in the experimental setup. The average values across the 83 runs, $(x_0, y_0) = (0.06\,\mathrm{mm}, 2.28\,\mathrm{mm})$, were adopted as the beam center position for this experiment. Additionally, the standard deviations $(\sigma_x, \sigma_y) = (0.35\,\mathrm{mm}, 0.22\,\mathrm{mm})$ were considered as systematic uncertainties for the detection efficiency of the DSSD. The excitation energy spectra obtained from each strip on the ohmic side after correcting the beam center position are shown in Fig. 4.2.6(b). This correction successfully aligned the excitation energies of the ohmic strips to converge on the discrete energy levels of ^{12}C.

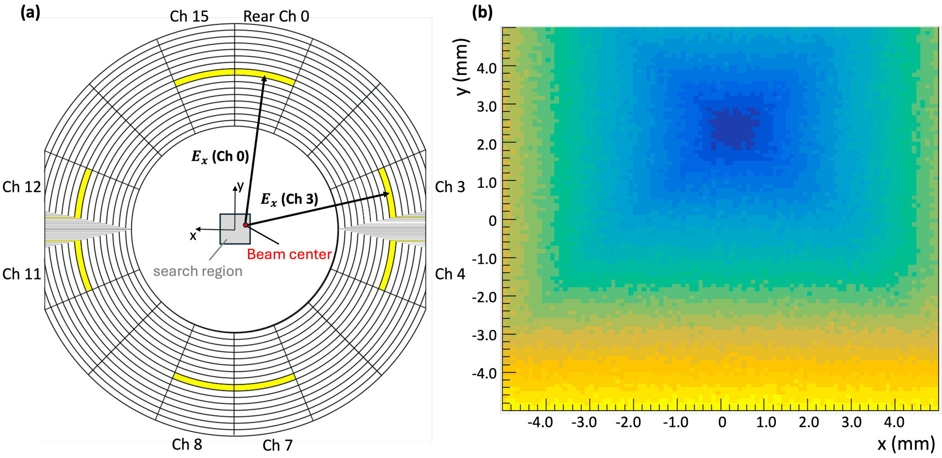

Figure 4.2.7: (a) Schematic view of the DSSD from the upstream side of the beam. (b) Magnitude of E_{diff} for various beam center positions.

4.2.6 Yield for the Hoyle state

The γ decay probability from the Hoyle state of ^{12}C is given by Eq. (4.6). Here, N_{H} represents the number of events where ^{12}C was excited to the Hoyle state, N_γ is the number of events in which the excited ^{12}C emitted two γ rays and decayed to the ground state, ϵ_{Si} is the detection efficiency for coincidence measurement of scattered α particles and recoiled ^{12}C using the DSSD, and ϵ_γ is the detection efficiency for emitted γ rays using ROSPHERE.

$$\frac{\Gamma_\gamma}{\Gamma} = \frac{N_\gamma}{N_{\mathrm{H}}} \frac{1}{\epsilon_{\mathrm{Si}} \cdot \epsilon_\gamma} \tag{4.6}$$

In this section, we determine the total number of events in which ^{12}C is excited to the Hoyle state N_{Hoyle}. Through the previous analysis, the energy and detection position of scattered α particles were accurately determined, and an excitation energy spectrum of ^{12}C was generated. Figure 4.2.8(a) shows the correlation between the excitation energy around $E_x = 7.65$ MeV and A'_{max} for scattered α particles. The peak structure corresponding to the Hoyle state in the red box and several background events are observed. On the lower excitation energy side near $A'_{\mathrm{max}} = 0$, a peak structure corresponding to the excited states of ^{13}C is present (blue box). On the higher excitation energy side, a continuous distribution (yellow box) is visible, which originates from the tail of broad states in the higher excitation energy region of ^{12}C. Additionally, in the $A'_{\mathrm{max}} > 0.1$ region, a continuous distribution of background events due to α particles scattered from the upstream collimator directly entering the DSSD is observed.

Figure 4.2.8(b) shows the A'_{max} distribution for the energy range $E_x =$ 7.4–7.9 MeV obtained during one cycle for the $^{\mathrm{nat}}$C target and an empty target. The histogram for the empty target is scaled so that the peak near $A_{\mathrm{max}} = 0.032$ matches in height. To maximize the yield N_{Hoyle}, it is necessary to count the Hoyle state peak over the widest possible range. However, for $A_{\mathrm{max}} > 0.015$, the background contribution becomes significant, posing a large systematic uncertainty for spectral fitting. To mitigate this issue, events attributed to the Hoyle state were gated in the range $A_{\mathrm{max}} = -0.02$ to 0.015.

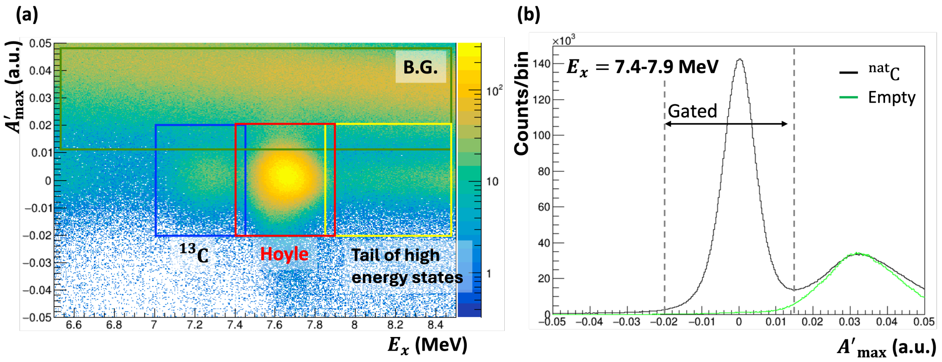

Figure 4.2.8: (a) Correlation between the excitation energy of scattered α particles around $E_x = 7.65$ MeV and A'_{max}. (b) A'_{max} distribution for $E_x = 7.4$–7.9 MeV.

Figure 4.2.9 shows the result of fitting the excitation energy spectrum gated in the range $A_{\rm max} = -0.0$–0.015 for the $^{\rm nat}$C target. The fitting components included a measured spectrum for the ^{13}C target (blue line), the empty target (green line), a Gaussian function for the Hoyle state of ^{12}C (purple line), and a Gaussian function for the broad higher excited state (yellow line). The fitting was performed using two methods:

a. The measured spectra for the ^{13}C and Empty targets were scaled to minimize the reduced chi-square ($\chi^2_{\rm red}$).

b. The spectra were scaled using the beam intensity irradiated on the ^{13}C and Empty targets.

In both cases, all parameters for the two Gaussian functions corresponding to the Hoyle state and the higher excited state were treated as free parameters.

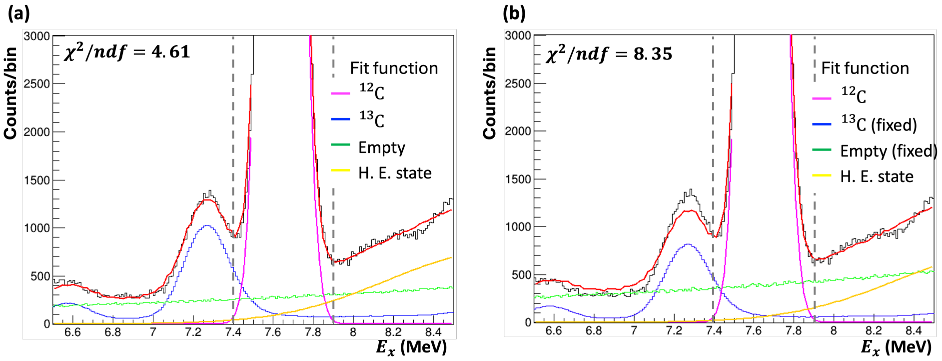

Figure 4.2.9: Result of fitting the excitation energy spectrum for the $^{\rm nat}$C target. The blue, green, purple and yellow line are corresponding the ^{13}C target, empty target, Hoyle state, and the broad higher excited state, respectively.

As a result, a better agreement was observed in Fig. 4.2.9(a), whereas the peak structure from ^{13}C was not reproduced accurately in Fig. 4.2.9(b). As described in Sec. 3.4, data acquisition for one cycle required 7.5 hours in this experiment. During a single cycle, factors such as shifts in the beam spot and fluctuations in $A^{\prime}_{\rm max}$ could have affected the peak structure of ^{13}C. Therefore, method (a), which provided a better fit, was adopted to determine the value of $N_{\rm Hoyle}$. The reason for the slightly larger value of $\chi^2_{\rm red}$ obtained by method (a) was that the gaussian function could not perfectly reproduce the actual peak shape corresponding to the Hoyle state. Hence, the value of $N_{\rm Hoyle}$ was obtained by subtracting the number of events corresponding to the fitted components for ^{13}C, the empty target, and the higher excited state from the total events in the range $E_{\mathrm{x}} = 7.4$–7.9 MeV in Fig. 4.2.9(a). The difference in N_{Hoyle} values obtained from the two fitting methods was treated as a systematic uncertainty$\sigma_{sys.}$ in the spectral fitting for a single data acquisition cycle.

Table 4.2.6 summarizes the results of the same analysis conducted for a total of 15 cycles. Here, $f_{^{13}\mathrm{C}}$ and f_{Empty} are the scaling factors used for the ^{13}C and Empty target spectra in Fig. 4.2.9(a), calculated based on the beam intensity. As a result, the total number of events in which ^{12}C was excited to the Hoyle state N_{Hoyle} was determined to be $N_{\mathrm{Hoyle}} = (7.63 \pm 0.09$ (sys.)) $\times\ 10^6$ counts.

Cycle	Charge (nC)	Yield (counts)	χ^2_{red}	$f_{^{13}\mathrm{C}}$	f_{Empty}	$\sigma_{\mathrm{sys.}}$ (%)
1	29,477	325,985	4.19	1.18	0.69	0.42
2	24,353	267,629	4.21	1.21	0.74	0.50
3	42,190	409,096	4.31	1.03	0.85	0.06
4	49,269	510,669	3.57	1.10	0.78	0.48
5	59,643	633,314	4.61	1.09	0.88	0.52
6	44,159	475,486	4.85	0.97	1.83	0.17
7	46,727	570,247	5.01	1.36	0.89	0.54
8	50,263	564,811	4.48	1.19	0.73	0.68
9	46,020	560,915	4.62	1.21	1.19	1.77
10	52,016	560,385	6.40	1.00	1.04	0.89
11	44,537	523,814	6.95	1.11	1.55	1.49
12	38,611	577,008	6.09	1.38	1.42	2.13
13	50,905	623,510	6.96	1.27	0.78	2.15
14	45,366	542,653	6.34	1.26	1.12	2.72
15	39,486	489,220	4.23	1.39	1.50	1.98
Total	663,022	7,634,742				1.17

Table 4.1: Summary of the results of the spectral fitting conducted for a total of 15 cycles.

To simulate the detection efficiency ϵ_{Si} for the coincidence measurement of scattered α particles and recoiled ^{12}C using the DSSD, the differential cross section for α+^{12}C scattering in this experiment was determined. In nuclear scattering experiments, the differential cross section is given by the following equation:

$$\frac{d\sigma}{d\Omega} = \frac{Y}{N_0 \cdot n \cdot \Delta\Omega} \tag{4.7}$$

where Y is the number of detected particles, N_0 is the number of incident particles on the target, n is the areal density of ^{12}C nuclei in the target, and $\Delta\Omega$ is the solid angle of the detector.

The DSSD used in this experiment can be divided into 256 matrices by combining the strips on the junction and ohmic sides, allowing the number of Hoyle state excitations to be determined for each matrix. The solid angle for each matrix was calculated using its area and the distance between the beam center and the center of each matrix. The total integrated beam charge of 663,022 nC and the thickness of the $^{\mathrm{nat}}$C target of 49 μg/cm^2 were used in the calculations.

Figure 4.2.10 shows the angular distribution of the differential cross section $d\sigma/d\Omega$ in the center-of-mass (CM) frame calculated for each matrix. The red curve represents the result of fitting the differential cross section with a high-order polynomial function, which was used for the simulation of the DSSD detection efficiency described in Sec. 4.4.1. Similar analyses were performed for the ground state and the first excited state of ^{12}C, and their angular distributions in the CM frame were obtained.

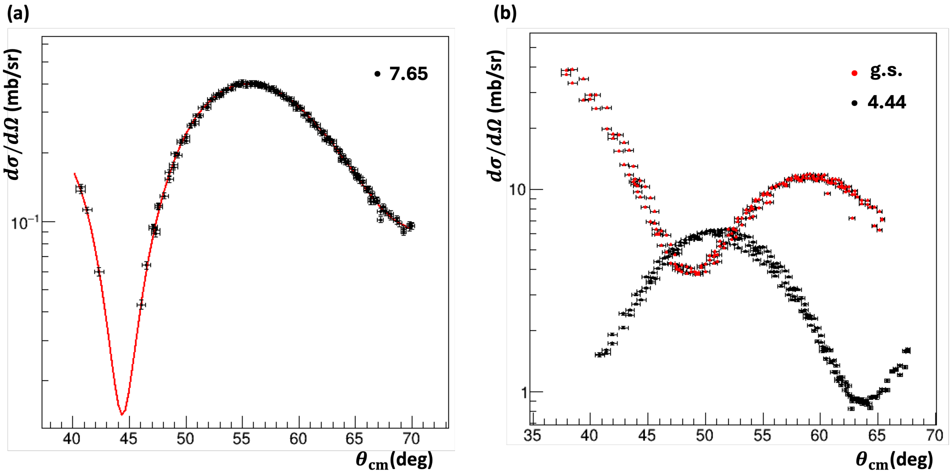

Figure 4.2.10: Differential cross section determined using each matrix of the DSSD for (a) $^{12}\mathrm{C}(\alpha,\alpha')^{12}\mathrm{C}(0_2^+)$ (b) $^{12}\mathrm{C}(\alpha,\alpha')^{12}\mathrm{C}(2_1^+)$ (black points) and $^{12}\mathrm{C}(\alpha,\alpha)^{12}\mathrm{C}$ (red points).

4.3 Data analysis of ROSPHERE

4.3.1 Energy calibration

For the energy calibration of ROSPHERE, a ^{56}Co source was used. ^{56}Co decays to ^{56}Fe via electron capture with a half-life of 77.27 days, emitting γ rays with energies up to 3.6 MeV. This γ–ray source is suitable for energy calibration in the high-energy region. As described in Appendix A, the signal waveforms acquired by the V1730SB were processed using the DPP-PSD firmware, which calculates and outputs the integral value of the waveform. The energy calibration was performed by fitting the peaks of known γ rays from the QDC spectrum to determine the peak centroids and deriving a linear conversion formula between the QDC channels and energy. The gamma-ray energies and intensities from ^{56}Co used for the calibration were obtained from the National Nuclear Data Center (NNDC) [53].

Figure 4.3.1(a) shows the gamma-ray energy spectrum obtained using a $LaBr_3$:Ce detector (ID = 2). The peaks at $E_\gamma = 1.238$, 1.771, and 2.598 MeV were fitted with single gaussian functions, as no nearby gamma-ray peaks were present. However, the peak around 3.2 MeV consisted of multiple γ rays with energies $E_\gamma = 3.202$, 3.254, and 3.273 MeV. Therefore, the region was fitted using the sum of three gaussian functions, as shown in Fig. 4.3.1(b). The mean values and heights of the three gaussian peaks were constrained to match the gamma-ray energies and intensity ratios listed in Table 4.2. The same analysis was conducted for all 24 detectors, resulting in an energy resolution for the 3.254 MeV gamma-ray of 0.94% (sigma) for the best detector (ID = 21) and 1.49% (sigma) for the worst detector (ID = 6).

Table 4.2: Gamma-ray energies E_γ and intensity ratios I_γ of ^{56}Co used for the fitting.

E_γ (MeV)	I_γ (%)
1.238	66.46
1.771	15.41
2.598	16.97
3.202	3.209
3.254	7.923
3.273	1.876

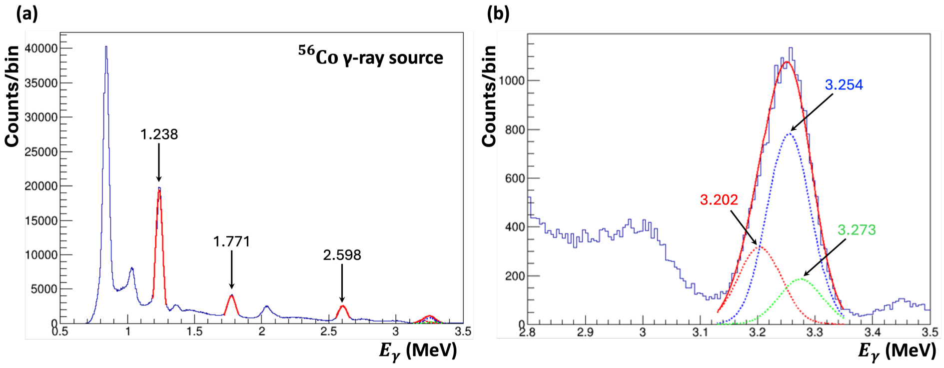

Figure 4.3.1: (a) Gamma-ray energy spectrum of ^{56}Co obtained with LaBr$_3$:Ce detector (ID = 2) and (b) Magnified view around 3.2 MeV.

4.3.2 Correction of Doppler effect

In this experiment, as illustrated in Fig. 4.3.2, a triple coincidence measurement of scattered α particles, recoiled ^{12}C, and γ rays was performed. Since the recoiled ^{12}C has momentum, the energy of the γ rays emitted from ^{12}C is shifted due to the doppler effect. Therefore, an analysis was conducted to correct for the energy shift caused by the Doppler effect.

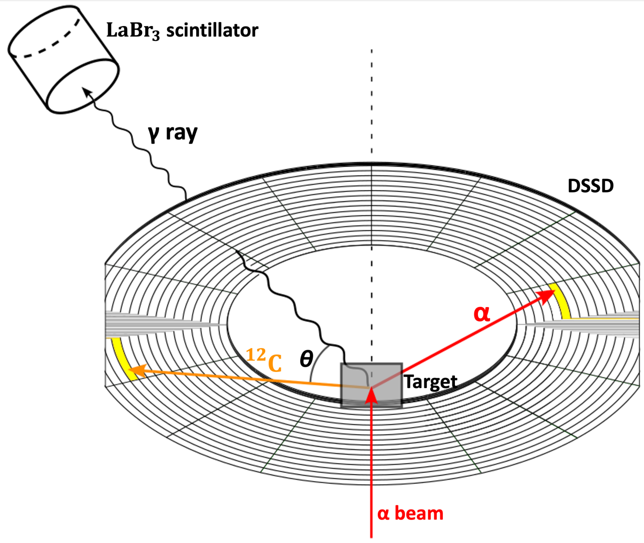

Figure 4.3.2: Schematic view of the α+^{12}C+γ triple-coincidence measurement method.

Consider the case where a γ ray is emitted in the zx plane from a ^{12}C nucleus moving along the z-axis with velocity v. Let E'_γ be the energy of the γ ray in the rest frame of ^{12}C and θ be the angle between the z-axis and the emitted γ ray. The four-momentum of the γ ray in the rest frame can be expressed as $p'^{\mu} = \left(\frac{E'_\gamma}{c}, \frac{E'_\gamma}{c}\cos\theta, \frac{E'_\gamma}{c}\sin\theta, 0\right)$. The energy component of the four-momentum after a Lorentz transformation is given by $p^0 = \gamma\left(p'^0 - \frac{v}{c}p'^1\right)$, where γ is the Lorentz factor. Therefore, the energy of the γ ray in the laboratory frame, E_γ, is described by the following equation:

$$E_\gamma = \gamma E'_\gamma\left(1 - \frac{v}{c}\cos\theta\right). \tag{4.8}$$

Since the emission of γ rays from the Hoyle state of ^{12}C is rare, the 4.44-MeV γ ray emitted from the first excited state of ^{12}C was used to evaluate the Doppler shift correction. The first excited state of ^{12}C was identified based on the A'_{max} parameter, as shown in Fig. 4.2.4. A coincidence window of 60 ns between ^{12}C and the γ rays was set to select the coincident γ rays.

Figure 4.3.3 shows the correlation between the angle θ and the γ ray energy E_γ for the 4.44-MeV γ ray emitted from the first excited state of ^{12}C before and after applying the correction described by Eq. (4.8). After the correction, the energy resolution for the 4.44 MeV absorption peak was evaluated for a single run. The best detector (ID = 21) achieved an energy resolution of 0.82% (sigma), the worst detector (ID = 6) achieved 1.35% (sigma), and the overall energy resolution was 0.97% (sigma).

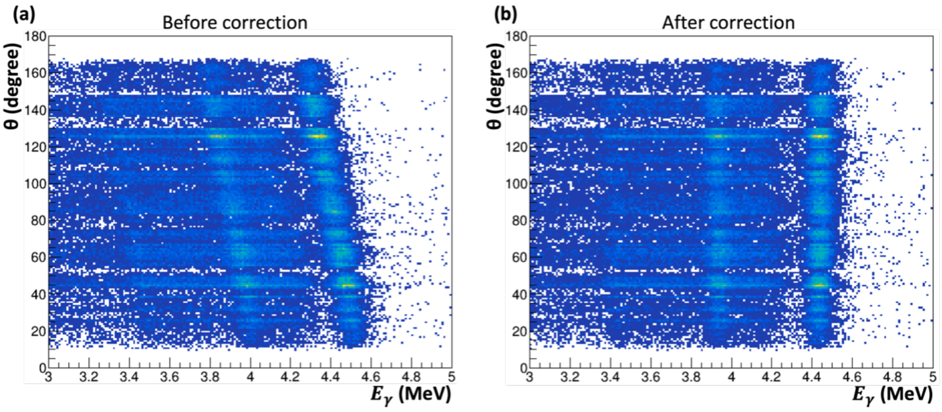

Figure 4.3.3: Angular dependence of the γ-ray energy (a) before and (b) after the doppler shift correction.

4.3.3 Correction of gain shift

Figure 4.3.4(a) shows the time variation of the energy spectrum for the 4.44-MeV γ ray emitted from the first excited state of ^{12}C over a 48-hour period from May 26 to May 27, 2022. The vertical axis represents the total number of triggered entries, which is approximately proportional to the elapsed time. In both days, the γ-ray energy reached its maximum in the morning and its minimum in the evening, which is considered to be caused by temperature-dependent variations in the scintillator's light emission characteristics. To correct for this effect, the linear correlation between the peak ADC and energy obtained in Sec. 4.3.1 was adjusted by scaling the linear coefficient for each run to ensure that the mean value of the full absorption peak corresponded to 4.44 MeV. At this time, it was assumed that no significant energy shifts occurred within each run.

After the gain shift correction, the time dependence of the γ-ray energy was corrected, as shown in Fig. 4.3.4(b).

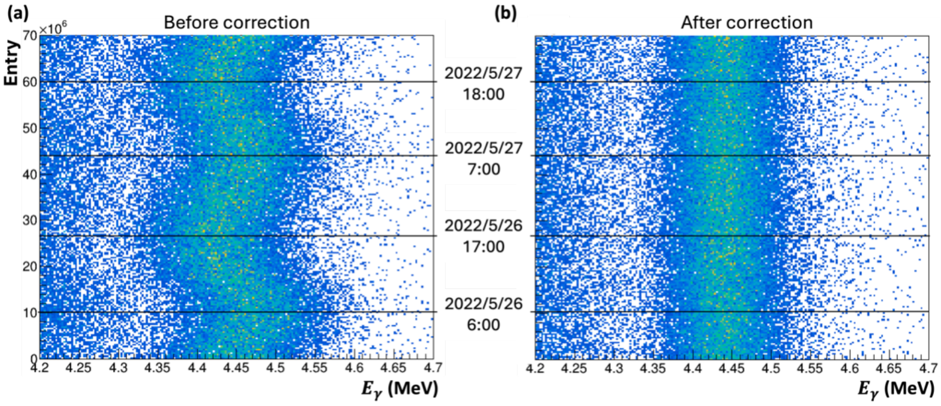

Figure 4.3.4: Time dependence of the γ-ray energy (a) before and (b) after gain correction.

Based on this analysis, the all γ-ray spectrum for the 4.44-MeV γ ray emitted from the first excited state of ^{12}C was constructed for the entire experiment. The energy resolution for the 4.44 MeV peak was determined to be 0.94% (sigma). This result is consistent with the energy resolution for the 4.44 MeV peak determined in a single run in Sec. 4.3.2, indicating that the gain shift correction was successfully applied during the beam time.

4.4 α+^{12}C coincidence

In this section, the selection of coincidence events between scattered α particles and recoiled ^{12}C is described to determine the number of γ-decay events from the Hoyle state N_γ, and the detection efficiency of the DSSD ϵ_{Si}. To eliminate background events originating from the 3α decay of the Hoyle state, kinematic and timing conditions were applied. The detection efficiency under these conditions was determined using Monte Carlo (MC) simulations.

4.4.1 MC simulation

To determine the simultaneous detection efficiency ϵ_{Si} for scattered α particles and recoiled ^{12}C with the DSSD, a MC simulation was performed. The implemented process was described in four steps below. The parameters used in the simulation are summarized in Table 4.3.

Step 1: α beam irradiation

In this step, the process leading up to the scattering of the α beam within the ^{12}C target was calculated. Initially, a 25 MeV α beam with a certain energy and angular spread was defined just before the target. The initial position on the incident plane was determined to reproduce the spot size observed with the viewer shown in Fig. 3.4.1. The α beam penetrated the target while experiencing energy loss and straggling effects at a certain point, and scattered to the ^{12}C. The depth of the scattering point within the target was assumed to be uniformly distributed. The values for straggling and energy loss in the target were calculated using the physical calculator of LISE++ [54]. First, the energy loss of α particles in a 49 µg/cm^2 $^{\mathrm{nat}}$C target was obtained for each incident energy, and a fitted formula was derived. Next, considering that the range of the particle within the target varies depending on the scattering point and scattering angle, the actual energy loss values were calculated by scaling the fitted formula.

Step 2: α+^{12}C scattering on the target

In this step, the kinematic calculations for the α+^{12}C scattering at the scattering point within the target were performed. The four-momentum of the α beam obtained in Step 1 was given as the initial value, and the four-momentum of the scattered α particle and the recoil ^{12}C excited to the Hoyle state were analytically calculated for a certain scattering angle in the center-of-mass (CM) frame. At this time, the scattering angle in the CM frame was determined based on a weighted random distribution to reproduce the angular distribution of the differential cross section shown in Fig. 4.2.10.

Step 3(a): γ decay of the Hoyle state

In this step, the process in which the recoil ^{12}C excited to the Hoyle state undergoes γ decay and exits the target was calculated. The four-momentum of ^{12}C obtained in Step 2 was given as the initial value, and the decay process was calculated, where two γ rays of 3.21 MeV and 4.44 MeV were sequentially emitted, leading ^{12}C to its ground state. At this time, it was assumed that the two γ rays were emitted isotropically in the rest frame of ^{12}C. Furthermore, the ^{12}C penetrated the target while experiencing energy loss and straggling, and the four-momentum of ^{12}C at the point where it exited the target was determined.

Step 3(b): 3α decay of the Hoyle state

In this step, the process in which the Hoyle state decays into three α particles and exits the target was calculated. The Hoyle state is allowed to decay through two mechanisms: the sequential-decay process, where an α particle is emitted, leading to the ground state of ^{8}Be, followed by the decay of ^{8}Be into two α particles, and the direct-decay process, where three α particles are emitted simultaneously. However, since the direct-decay process is extremely rare with a reported branching ratio of $< 0.043\%$ [49–51], only the sequential-decay process was considered in this simulation. The four-momentum of ^{12}C obtained in Step 2 was given as the initial value, and both decay steps were assumed to occur isotropically in the center-of-mass (CM) frame. Furthermore, the three α particles penetrated the target while experiencing energy loss and straggling, and the four-momentum of the particles at the point of exiting the target was determined.

Step 4: α and ^{12}C detection on the DSSD

In this step, the process of detecting the α and ^{12}C emitted from the target by the DSSD was calculated. The DSSD was defined 40 mm downstream from the target and positioned considering the beam-center shift relative to the center of the Si detector, as described in Sec. 4.2.5. Using the four-momentum of each particle emitted from the target, the hit position and energy on the DSSD were determined. At this time, due to the beam-center shift relative to the center of the DSSD described in Sec. 4.2.5, the center of the $16 \times 16 = 256$ pixels of the DSSD was taken as the particle detection position, and the emission angle for each pixel was determined. The detected energy on the DSSD was determined considering the energy resolution of the DSSD to reproduce the actual experimental conditions. However, since a thin layer of aluminum was evaporated on both sides of the DSSD as electrodes, the charge generated by the particle in the Al layer was not collected, making the Al electrode a dead layer. As described in Sec. 4.4.2, the thickness of the dead layer was evaluated, and the energy loss within the dead layer was subtracted from the detected energy.

Table 4.3: Parameters used in the MC simulation

Beam energy	25.0 MeV
Beam energy spread	0.025 MeV
Beam angular spread	0.57 deg.
X-axis spread of beam spot	0.6 mm
Y-axis spread of beam spot	0.4 mm
X-axis offset of beam spot	0.20 mm
Y-axis offset of beam spot	2.49 mm
Distance between target	40 mm
Thickness of Al layer	0.55 µm
Energy resolution	0.9%

4.4.2 Dead layer

In the DSSD used in this experiment, the dead layers consist of a 0.50 µm (nominal value) Al electrode for signal readout and a P-type impurity B^{+} layer implanted on the junction side. Since the particles were incident from the ohmic side in this experiment, the energy loss while passing through the Al electrode on the ohmic side could not detected. Therefore, the thickness of the dead layer t_d was varied in the simulation, and the dead layer thickness was determined by comparing with experimental data. The coincidence events between scattered α particles and the first excited state of ^{12}C were used for the comparison between experiment and simulation.

Figure 4.4.1 shows the distribution of the total detected energy $E_{\text{total}} = E_\alpha + E_{^{12}\text{C}}$ (MeV). Since the beam energy in this experiment was 25.0 MeV, the expected value should be $E_{\text{total}} = 25.0 - 4.44 = 20.56$ MeV. However, due to the energy loss in the dead layer on the ohmic side and the energy loss in the $^{\text{nat}}$C target, the observed E_{total} value decreased. The spread in E_{total} mainly originates from the angular resolution and the energy resolution R_E of the DSSD. Among the total 15 data acquisition cycles, (a) Cycle 2 with the highest E_{total} value and (b) Cycle 8 with the lowest E_{total} value were compared with the simulation. The values of t_d and R_E were determined by minimizing the reduced chi-square value. The red points in the figure represent the simulated data used for the fitting.

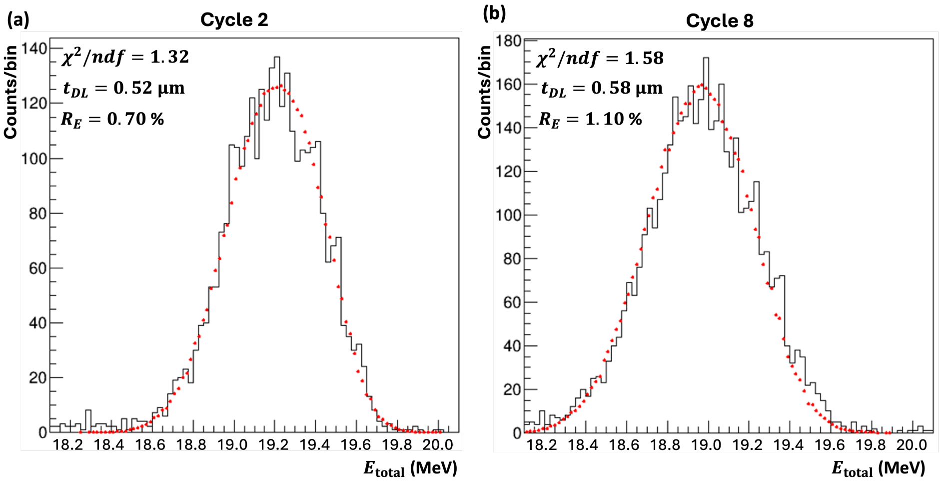

Figure 4.4.1: Distribution of E_{total} in (a) Cycle 2 and (b) Cycle 8. The red points represent the results of spectrum fitting using simulation data.

As a result of the fitting, t_d was determined to be 0.52–0.58 μm, which was systematically larger than the nominal value of 0.50 μm. This discrepancy could be due to insufficient bias voltage applied to the DSSD, possibly leaving an undepleted region near the Ohmic side. In such a case, variations in the leakage current of the DSSD during the beam time could affect the effective voltage applied to the DSSD, causing the mean value of E_{total} to change cycle by cycle, making it difficult to determine the actual dead layer thickness. Therefore, in this experiment, the actual dead layer thickness was evaluated using the mean and standard deviation of t_d determined for each cycle, resulting in $t_d = 0.550 \pm 0.025$ µm. The error in t_d represents a systematic error and was considered as a systematic uncertainty when evaluating the detection efficiency in Sec. 4.4.4.

4.4.3 Event selection

When the Hoyle state of ^{12}C undergoes γ decay (^{12}C event), a clear kinematic correlation can be observed between the scattered α particle and recoiled ^{12}C. On the other hand, when the Hoyle state decays into three α particles (3α event), the decay α particles are detected over a wide area of the DSSD. To eliminate background events originating from this 3α decay, kinematic and timing conditions between the scattered α particle and ^{12}C were applied to select the ^{12}C events.

Time correlation between α and ^{12}C

First, among the particles detected in coincidence with the scattered α particle, only 1–1 events were used for the analysis as candidate events for the ^{12}C event. Figure 4.4.2 shows the correlation between the detection times t_α and $t_{^{12}\mathrm{C}}$ for the scattered α particle and the candidate ^{12}C events. The time difference between the scattered α particle and the ^{12}C or decay α particles is typically less than 10 ns at a typical energies. However, the actual distribution of $t_{^{12}\mathrm{C}}$ ranged widely from 0 ns to 50 ns.

As described in Appendix A, the particle detection time in the DSSD was obtained using a TTF filter, where the time walk due to slew effects was already corrected, and no energy dependence on $t_{^{12}\mathrm{C}}$ was observed. However, a moving average of 32 samples (64 ns) was applied during the preprocessing for the TTF filter, and this large number of samples may have degraded the timing resolution. Therefore, to avoid missing true ^{12}C coincidence events, the events within the red frame in the figure were selected. Additionally, to estimate the number of accidental ^{12}C coincidence events, the number of events within the black frame was counted and considered in the analysis described in Sec. 4.4.3.

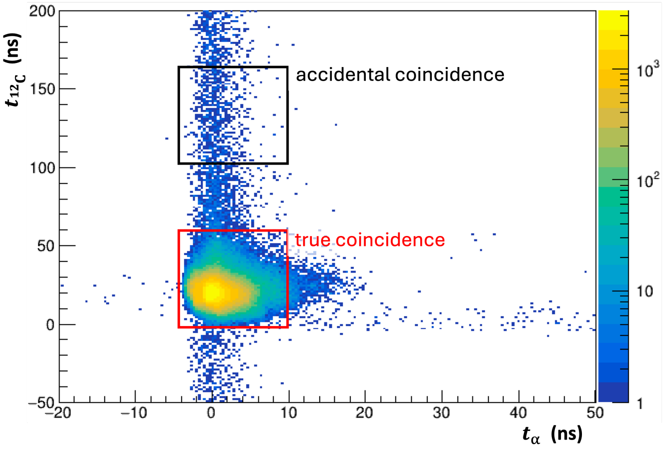

Figure 4.4.2: Correlation between detection times of the scattered α particle and ^{12}C

Angular correlation between α and ^{12}C

Figure 4.4.3 shows the correlation of the polar angle θ between the scattered α particle and (a) ^{12}C or (b) decay α particles obtained using the simulation. The ^{12}C events exhibit a clear correlation, while the decay α events are widely distributed across the entire DSSD area. To remove this background, events within the black dashed line region shown in the figure were selected. Additionally, ^{12}C events located outside the region correspond to cases where ^{12}C particles entered areas of the DSSD dedicated to signal readout, as illustrated in Fig. 3.2.3. Since the emission angles of the detected particles could not be accurately determined for these events, they were excluded from the analysis.

Figure 4.4.4 shows the difference in azimuthal angle ϕ between the scattered α particle and ^{12}C or decay α particles, obtained from the simulation. Since the scattered α particle and the recoil ^{12}C should be detected on the same plane, a structure around $\phi = 180°$ is expected for the ^{12}C events. However, due to the beam center being shifted relative to the center of the Si detector in this experiment, peak structures were also observed near $\phi = 165°$ and $195°$. Therefore, a gate condition of $165° < \phi < 205°$ indicated by the black dashed lines was applied to include these peaks.

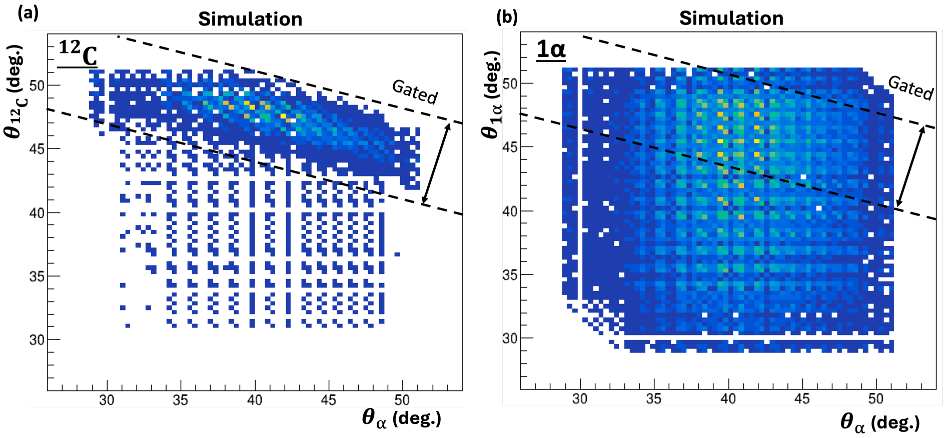

Figure 4.4.3: Correlation of the polar angle θ between the scattered α particle and (a) ^{12}C and (b) decay α particles.

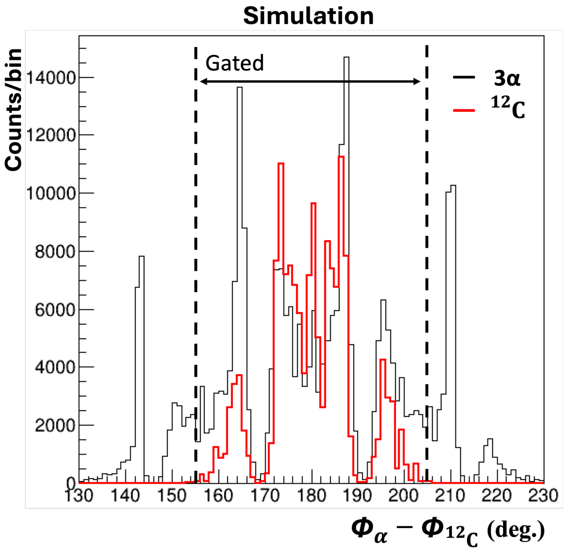

Figure 4.4.4: Difference in the azimuthal angle ϕ between the scattered α particle and ^{12}C or decay α particles.

Energy correlation between α and ^{12}C

Figure 4.4.5(a) shows the energy correlation between the scattered α particle and ^{12}C obtained from simulations, represented by red points. The energy correlation between the scattered α particle and one of the decay α particles from the 3α events is shown by the black points. In the low-energy region of ^{12}C, the ^{12}C events are buried under the overwhelming background from 3α events. Furthermore, in this energy region, it was not possible to discriminate between ^{12}C and α particles using PSD, making the identification of low-energy ^{12}C events infeasible. Therefore, to ensure the detected particle is ^{12}C, a gate was applied to the events within the black dashed region shown in the figure, selecting only α+^{12}C coincidence events.

Figure 4.4.5(b) shows the energy correlation between the scattered α particle (K_α) and the recoil particle (K_r) from the experimentally measured coincidence events. As in Fig. 4.4.5(a), the gate condition determined from the simulation is indicated by the black dashed lines. While a significant number of background events from 3α decay are observed in the low-energy region, a continuous distribution of events was also observed within the gate.

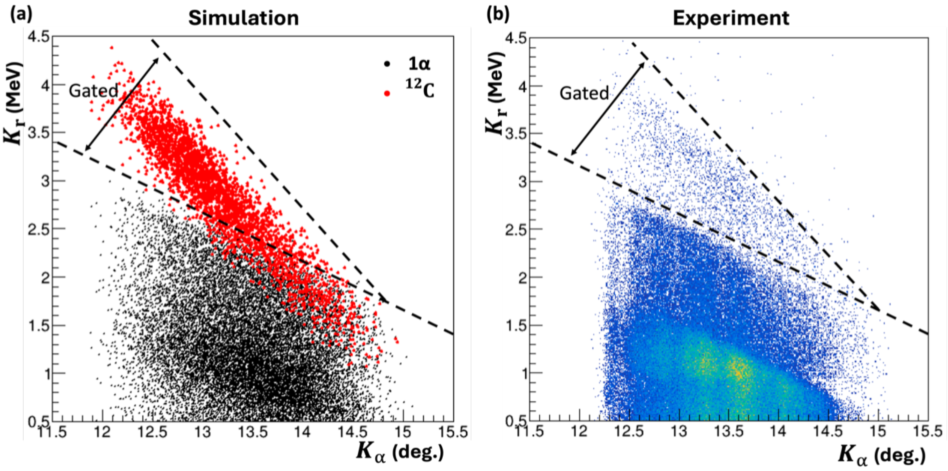

Figure 4.4.5: Energy correlation between the scattered α particle and the recoil particle for (a) simulation. and (b) experiment.

When ^{12}C undergoes sequential 3α decay, the relative momentum between the two α particles emitted from ^{8}Be becomes extremely small. As a result, multiple particles can enter the same pixel of the DSSD (multi-α events), and the sum of the energies of multiple α particles is detected. The probabilities for two and three α particles entering the same pixel were determined in the simulation to be 3×10^{-3} and 6×10^{-6}, respectively. The probability of a two-α event is an order of magnitude higher than the γ decay probability of ^{12}C.

Figure 4.4.6 shows the energy correlation between the scattered α particle and the two α particles emitted from ^{8}Be obtained from the simulation. The two-α events are distributed within the gate condition used to distinguish between single α and ^{12}C particles, indicating that this gate condition cannot completely eliminate two-α events.

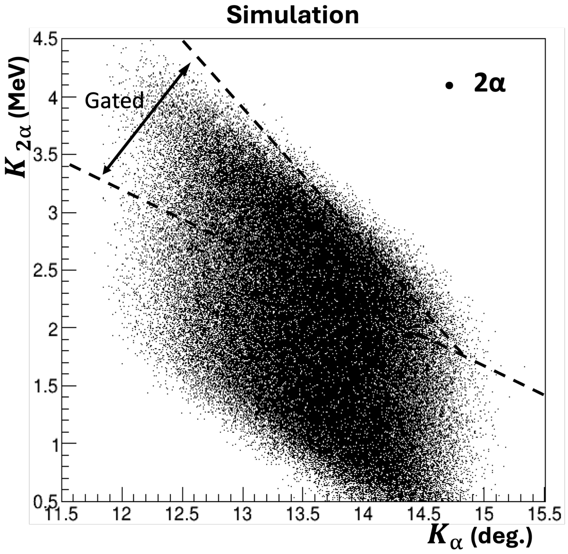

Figure 4.4.6: Energy correlation between the scattered α particle and two α particles from ^{8}Be in the simulation.

Background subtraction

By applying the kinematic conditions determined in Sec. 4.4.3 to the experimental data, candidate events for the ^{12}C events were selected. Figure 4.4.7(a) shows the correlation between the excitation energy of ^{12}C and A'_{max} for the candidate ^{12}C events. Within the red box in the figure, corresponding to the region E_x = 7.40–7.90 MeV and A'_{max} = -0.025–0.025, a total of 1986 candidate ^{12}C events were observed. Additionally, a structure attributed to ^{13}C was observed on the low excitation energy side (blue box), while a broader tail structure (yellow box) was visible on the high excitation energy side. Moreover, a structure due to multi-α events was observed in the region of larger A'_{max} values. Since these three types of background could not be removed using kinematic conditions alone, the background contribution within the red box was determined using spectrum fitting.

Multi-α events can not be separated from ^{12}C events using the energy conditions determined in Sec. 4.4.3. However, it may be possible to distinguish between ^{12}C events and multi-α events using the waveform of the output signals from the DSSD. When the detected energy is similar, the energy of individual α particles in a multi-α event is lower than the energy of ^{12}C in a ^{12}C event. Since the characteristics of the DSSD output waveform vary depending on the particle energy, the signal waveform when two α particles hit the DSSD may differ from the signal waveform when a single ^{12}C hits. Figure 4.4.7(b) shows the correlation between the detected energy and A'_{max} for E_x = 7.40–7.90 MeV. On the high-energy side, ^{12}C and multi-α events are completely separated. However, as the energy decreases, the difference in A'_{max} diminishes, and below 2.8 MeV, no clear separation in A'_{max} is observed.

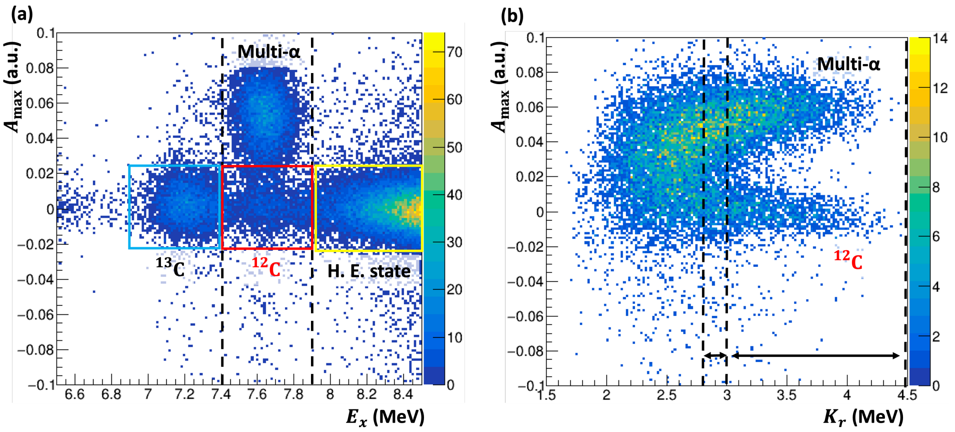

Figure 4.4.7: (a) Correlation between the excitation energy of ^{12}C and A'_{max}, and (b) correlation between the detected energy and A'_{max} for E_x = 7.40–7.90 MeV.

Therefore, spectral fitting was performed for recoil particle energies $K_{\text{r}} \geq$ 2.8 MeV to estimate the background contribution from multi-α events. Figure 4.4.8 shows the results of spectral fitting of the A'_{max} distribution for (a) $3.0 \leq K_{\text{r}} < 4.5$ MeV and (b) $2.8 \leq K_{\text{r}} < 3.0$ MeV. Here, the ^{12}C events were fitted with a Gaussian distribution shown by the purple line, while the distribution function for the multi-α background was fitted with an exponential distribution represented by the black line. However, since the actual background distribution is unknown, not only an exponential model but also linear and quadratic functions were used for fitting. The mean and standard deviation of the background contribution were estimated from the results of these fits. As a result of the analysis, the number of multi-α background events within the red box in Fig. 4.4.7(a) was estimated to be 241 ± 16 (sta.) $\pm$ 39 (sys.) counts.

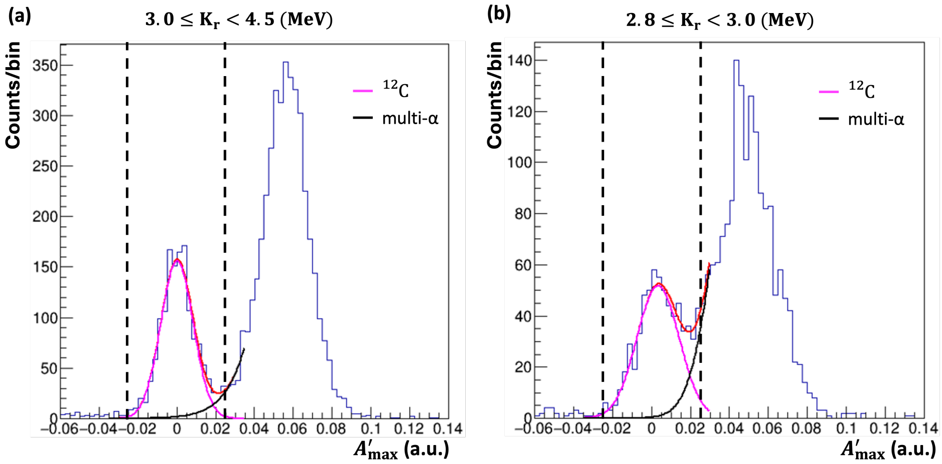

Figure 4.4.8: Distribution of A'_{max} and the fitting results for (a) $3.0 \leq K_{\mathrm{r}} < 4.5$ MeV and (b) $2.8 \leq K_{\mathrm{r}} < 3.0$ MeV.

Next, the background contribution from ^{13}C and the tail of the high excitation energy states of ^{12}C was evaluated. Figure 4.4.9 shows the excitation energy distribution of ^{12}C for $A'_{\mathrm{max}} = -0.025$ to 0.025 in (a) $3.0 \leq K_{\mathrm{r}} < 4.5$ MeV and (b) $2.8 \leq K_{\mathrm{r}} < 3.0$ MeV. At this time, the number of background events from accidental coincidences was subtracted from the spectrum. The fitting functions used were the experimental spectrum measured with a ^{13}C target (blue), a Gaussian function corresponding to the Hoyle state (purple), and a broader Gaussian function corresponding to higher excited states (yellow). The sum of these three fitting functions is shown as the red line. To minimize the reduced chi-square value (χ^2_{red}), the scaling factor for the experimental spectrum obtained with the ^{13}C target and the parameters (centroids, widths, and heights) of the two Gaussian functions for the high-excitation states were optimized.

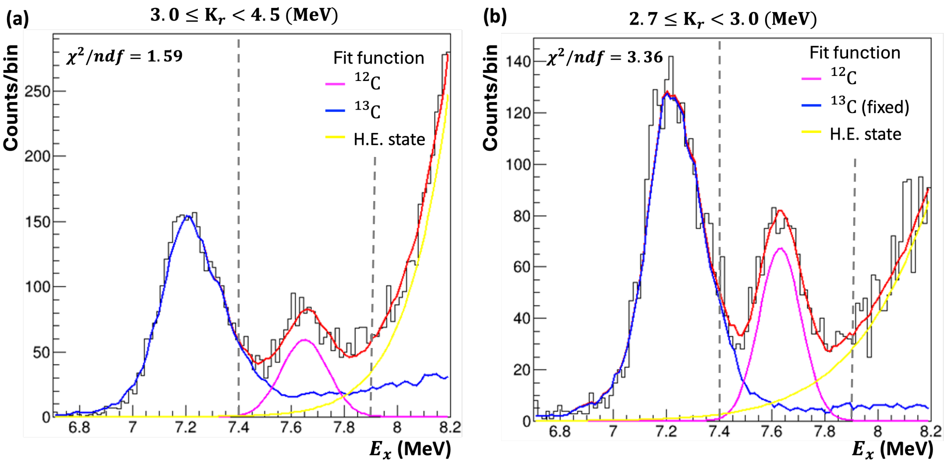

Figure 4.4.9: Excitation energy distribution of ^{12}C fitted using spectrum fitting for (a) $K_\mathrm{r} \geq 3.0$ MeV and (b) $2.8 \leq K_\mathrm{r} < 3.0$ MeV.

As a result of the fitting, the number of background events from ^{13}C and the high-excitation state tails within the red box in Figure 4.4.7(a) was determined to be 656 ± 26 (sta.) and 359 ± 19 (sta.) events, respectively. Therefore, the total background contribution from ^{13}C and the high-excitation states in the red box of Fig. 4.4.7(a) was determined to be 1015 ± 32 (sta.) counts.

Based on these results, after subtracting the three background components, the yield of ^{12}C events in the red box of Fig. 4.4.7(a) was determined to be: $Y = 730 \pm 57$ (sta.) $\pm$ 39 (sys.) counts.

4.4.4 γ–decay probability determined with the α+^{12}C coincidence events

Coincidence detection efficiency of the α+^{12}C pair with DSSD

By applying the kinematic conditions determined in Sec. 4.4.3 to the simulation, the coincidence detection efficiency of the α+^{12}C pair ϵ_{Si} was determined. The error in ϵ_{Si} was evaluated using the systematic uncertainty of the dead layer.

Using the obtained ϵ_{Si}, the γ decay probability Γ_γ/Γ of the Hoyle state was determined using the particle coincidence method. The parameters used for the calculation of Γ_γ/Γ are summarized in Table 4.4.4. In this analysis, the coincidence detection efficiency significantly decreased due to the exclusion of background 3α events. Moreover, the value of t_d introduced a significant uncertainty in both the coincidence detection efficiency and Γ_γ/Γ.

The obtained value of $\Gamma_\gamma/\Gamma = 4.30(52) \times 10^{-4}$ supports the previous study [1]. However, the large uncertainty prevented the exclusion of either result with sufficient confidence.

ϵ_{Si}	Y_{total} (Counts)	Y_{H} (Counts)	Γ_γ/Γ (10^{-4})
0.219 ± 0.020 (sys.)	7,634,742	730	4.30 ± 0.34 (sta.) $\pm$ 0.40 (sys.)

Table 4.4: The obtained Γ_γ/Γ and parameters used for its calculation.

4.5 α+^{12}C+γ coincidence method

In this section, the yield of triple coincidence events was determined by selecting γ-ray coincidence events with ROSPHERE for the α+^{12}C particle coincidence events. The response of ROSPHERE to γ rays was simulated using Geant4, and the detection efficiency of ROSPHERE was determined from both experimental data and simulations. Using the obtained yield and detection efficiency, the γ decay probability of the Hoyle state was determined with the triple coincidence method.

4.5.1 Simulation with Geant4

To determine the γ-ray detection efficiency ϵ_γ in this experiment, the response of ROSPHERE to γ rays was simulated using Geant4 [48]. Geant4 is a software framework designed to simulate particle transport through matter. It mainly consists of the following three components. ”PrimaryGeneratorAction” defines the generation method of primary particles. ”DetectorConstruction” defines the geometry and materials used for the detectors. ”PhysicsList” defines the physical processes of particles interacting with matter. The structure of the Geant4 simulation used in this calculation is described below.

PrimaryGeneratorAction

To simulate the γ rays emitted from the Hoyle state, single-energy γ rays of 4.44 MeV and 3.21 MeV were defined as the primary particles. A total of N_H events were generated for each γ-ray energy, with isotropic emission from the center of the target.

DetectorConstruction

In this experiment, it was necessary to account for the attenuation of γ rays caused by the scattering chamber placed inside ROSPHERE. Therefore, ROSPHERE, the scattering chamber, the target ladder, the DSSD and its readout board, and the web camera were defined in the simulation. However, the flat cables connecting the DSSD readout board to the feedthrough were excluded from the simulation since their exact positions could not be determined during the experiment. The flat cables contribute approximately one-tenth the material thickness and one-fifth the solid angle compared to the SUS chamber, making their effect negligible in the simulation.

The shapes of all objects were managed using 3D CAD software, and CADMesh was used to import CAD files into the Geant4 geometry. CADMesh is a library that allows the direct import of complex models created in 3D CAD software into Geant4 geometries.

The elements used for each object were retrieved using the G4NistManager class, which references standard elements defined in the NIST database [55]. When a compound was used for a component, it was defined by combining the elements with the appropriate composition ratios. Table 4.5.1 shows the density and composition ratios of the compounds used for each object.

Object	Compound	Density (g/cm^3)	Composition ratio
ROSPHERE	$LaBr_3$(Ce)	5.08	La 24.9, Br 74.6%, Ce, 0.5%
ROSPHERE	$CeBr_3$	5.10	Ce 25%, Br 75%
ROSPHERE	BGO	7.13	Bi 21.1%, Ge 15.8%, O 21.1%
Chamber	SUS	8.00	Fe 73.66%, Cr 18.20%, Ni 8.10%, C 0.04%
PCB board	FR4	1.85	C 23.0%, O 38.5%, H 27.5%, Si 11.0%

Table 4.5: density and composition ratios of the compounds used for each object

PhysicsList

To simulate the electromagnetic interactions between γ rays and matter, the "PenelopeEMPhysics" model was used, which handles the transport of electrons, positrons, and photons. Geant4 provides three models for electromagnetic interactions: "PenelopeEMPhysics", "EmStandardPhysics", and "EmLivermorePhysics". Previous studies have performed γ-ray detection simulations using these models with $LaBr_3$(Ce) and $CeBr_3$ detectors, reporting minimal model dependence in the detection efficiency in the MeV energy region [56, 57]. In the PenelopeEMPhysics model, the physical processes for γ rays, electrons, and positrons are defined as follows:

1. γ ray : Photo electric effect, Compton scattering, Pair production
2. electron : Ionisation, Universal fluctuation, Bremsstrahlung
3. Positron : Ionisation, Universal fluctuation, Bremsstrahlung, Annihilation

Here, the "Universal fluctuation" refers to the statistical fluctuation in the energy loss of charged particles as they pass through a material.

Event generation

In Geant4, when a generated particle moves through the simulation space, its path is divided into multiple short segments called steps. Information such as the particle's position, momentum, and interactions is recorded at each step. Therefore, the energy deposited by a particle in the scintillator is calculated as the sum of the energy losses over all steps within the scintillator.

Figure 4.5.1(a) shows the expected energy spectrum for 4.44-MeV γ rays detected by ROSPHERE, represented by the black line. In this energy region, the cross-section for pair production is relatively large, and the resulting positron annihilation produces 511 keV annihilation γ rays that may escape the detector, leading to the formation of single (double) escape peaks. Since these annihilation γ rays are mostly absorbed by the BGO detectors surrounding the scintillator, the single (double) escape events can be excluded by using the BGO detectors. However, in this experiment, the detection threshold of the BGO detectors was set around 0.8 MeV, which prevented this exclusion. Since the simulation did not account for the energy resolution of the LaBr3(Ce) and CeBr3 detectors, a Gaussian energy resolution function $R(E_\gamma) = \Delta E_\gamma / E_\gamma$ was manually applied to the events, and the energy spectrum obtained after applying the resolution is shown by the red line in Fig. 4.5.1(a). The energy resolution was determined to follow the relationship $R(E_\gamma) \propto 1/\sqrt{E}$. In subsequent analyses, the experimental γ-ray spectrum will be fitted using a simulated spectrum with appropriately evaluated energy resolution to determine the yield of the γ rays.

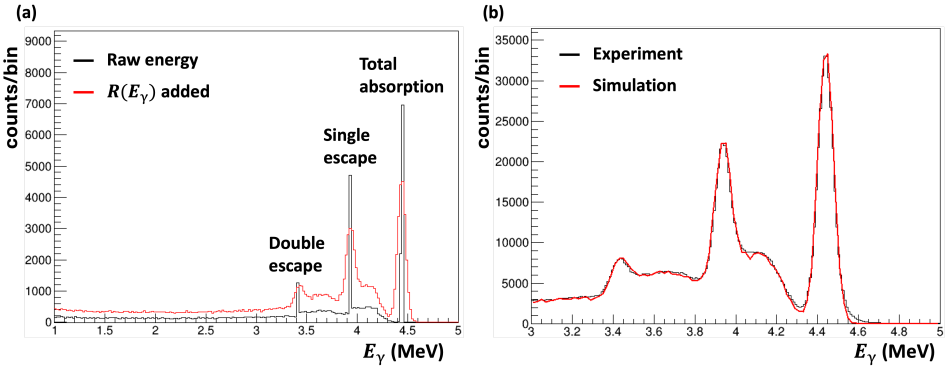

Figure 4.5.1: (a) Simulated energy spectrum for 4.44-MeV γ rays detected by ROSPHERE (black line) and after applying energy resolution (red line). (b) Comparison between the experimental (black line) and simulated (red line) 4.44-MeV γ-ray spectra.

Figure 4.5.1(b) shows the 4.44-MeV γ-ray spectrum from the first excited state of ^{12}C obtained from the analysis described in Sec. 4.3.3, represented by the black line. For comparison, a simulated spectrum with an energy resolution of 0.94% (sigma) for the 4.44-MeV γ rays was created. The results of a fitting by this spectrum with height as a free parameter are shown by the red lines. The three peak structures and the continuous distribution corresponding to Compton scattering are well reproduced. However, a systematic deviation can be observed in the low-energy tail of the total-absorption peak. This discrepancy is likely due to the limitations in fully replicating the experimental conditions in the simulation. Therefore, this deviation was considered as a systematic uncertainty in the detection efficiency for subsequent analyses.

4.5.2 Detection efficiency of γ ray

The detection efficiency ϵ_γ for 4.44-MeV γ rays in ROSPHERE was determined from both experimental data and simulations. Since the decay of the Hoyle state proceeds as $0_2^+ \to 2_1^+ \to 0_1^+$, the first emitted 3.21 MeV γ ray is emitted isotropically relative to the beam axis. The subsequently emitted 4.44-MeV γ ray is correlated with the emission angle of the 3.21 MeV γ ray. However, due to the isotropic nature of the 3.21 MeV emission, the angular distribution of the 4.44-MeV γ ray relative to the beam axis also becomes isotropic.

Figure 4.5.2(a) shows the total-absorption efficiency $\epsilon_{\gamma,\mathrm{sim.}}$ for 4.44-MeV γ rays obtained from the simulation for each of the 24 detectors. ROSPHERE consists of four or five detectors positioned at $\theta = 37^\circ$ (+A), 70° (+B), 90° (C), 110° (−B), and 143° (−A) relative to the beam axis. The variation in detection efficiency among detectors is primarily due to differences in the distance from the target to the scintillator (see Table 3.2.3 for the distances). However, even for detectors placed at the same distance, slight variations in detection efficiency were observed due to the attenuation of γ rays by objects inside ROSPHERE. The simulated total-absorption efficiency for 4.44-MeV γ rays in ROSPHERE was evaluated by summing the detection efficiencies of all detectors, resulting in $\epsilon_{\gamma,\mathrm{sim.}} = 2.65\%$.

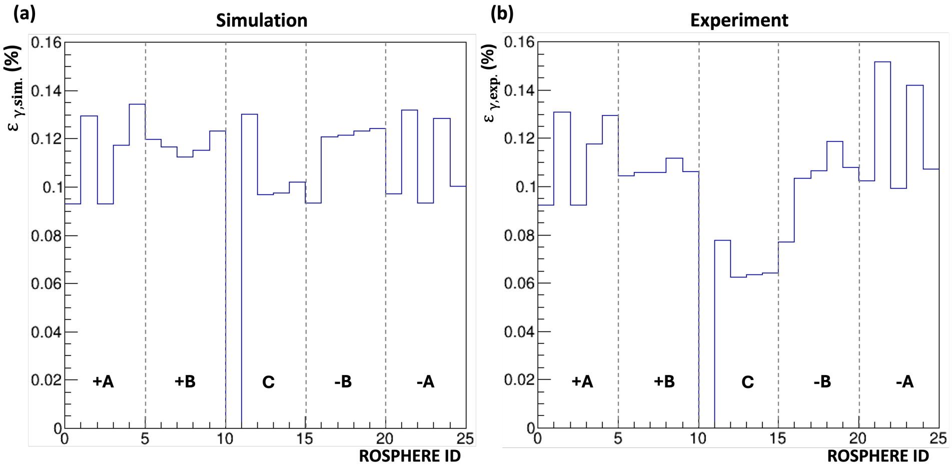

Figure 4.5.2: Total-absorption efficiency for the 4.44-MeV γ rays obtained for each of the 24 detectors. (a) Simulation. (b) Experiment.

Next, to estimate the detection efficiency of ROSPHERE $\epsilon_{\gamma,\mathrm{exp.}}$ from the experimental data, the decay events from the first excited state of ^{12}C obtained from the analysis described in Sec. 4.3.3 were used. Figure 4.5.1(b) shows the total-absorption efficiency for 4.44-MeV γ rays obtained for each of the 24 detectors. Compared to the simulation results, the individual variations caused by the setup are consistent. However, the total-absorption efficiency for Group C, located at $\theta = 90^\circ$, is lower than expected. This discrepancy arises from the magnetic quantum number distribution in the 2_1^+ state, which is excited via α inelastic scattering, leading to a non-isotropic angular distribution of the γ rays emitted from the $E2$ transition. It has been reported in previous studies [34, 58] that the angular distribution of γ rays emitted by the $E2$ transition can be well described by the angular distribution function $W_\gamma(\theta)$ given by Eq. (4.9).

$$W_\gamma(\theta_{\text{lab}}) = 1 + A_2 P_2(\cos\theta) + A_4 P_4(\cos\theta) \tag{4.9}$$

Here, A_i represents the coefficients of the i-th order Legendre polynomial $P_i(\cos\theta)$, describing the anisotropy of the angular distribution, and θ denotes the emission angle of the γ rays relative to the beam axis. The angular distribution $W_\gamma(\theta)$ is normalized so that the average intensity equals 1. Therefore, a scaling parameter "k" was introduced, and $kW_\gamma(\theta)$ was used as the fitting function.

To properly evaluate the effect of the angular distribution due to the $E2$ transition, it is necessary to remove the effects of individual detector efficiency variations caused by the experimental setup. Therefore, to extract the effect of the angular distribution, the ratio of detection efficiencies between the experimental data and the simulation ($\epsilon_{\gamma,\text{exp.}}/\epsilon_{\gamma,\text{sim.}}$) was calculated. Figure 4.5.3 shows (a) the ratio $\epsilon_{\gamma,\text{exp.}}/\epsilon_{\gamma,\text{sim.}}$ for each of the 24 detectors and (b) the correlation between $\epsilon_{\gamma,\text{exp.}}/\epsilon_{\gamma,\text{sim.}}$ and the angle θ. This scatter plot was fitted using the function $kW_\gamma(\theta_{\text{lab}})$, where $W_\gamma(\theta)$ describes the angular distribution.

The result of the fitting, shown by the red line in Fig. 4.5.3(b), determined the angular distribution of γ rays emitted from the first excited state of ^{12}C as :

$$W_\gamma(\theta_{\text{lab}}) = 1 + 0.077(58) \times P_2(\cos\theta) - 0.621(12) \times P_4(\cos\theta) \tag{4.10}$$

The residuals between the measured $\epsilon_{\gamma,\text{exp.}}/\epsilon_{\gamma,\text{sim.}}$ and the fitted function for each detector represent the individual detector variations that were not reproduced in the simulation. Therefore, the standard deviation of these residuals, $\sigma = 0.04$, was considered as the systematic uncertainty in the detection efficiency.

$$W_\gamma(\theta_{\mathrm{lab}}) = 1 + 0.077(58) \times P_2(\cos\theta) - 0.621(12) \times P_4(\cos\theta) \tag{4.11}$$

By considering this angular distribution of the emitted γ rays, the detection efficiency of each detector for isotropically emitted γ rays from the Hoyle state was evaluated. The total-absorption efficiency for the entire ROSPHERE detector system was determined to be $\epsilon_{\gamma,\mathrm{exp.}} = 2.41 \pm 0.09\%$. Additionally, the ratio of detection efficiencies between the experimental data and the simulation was determined to be $\epsilon_{\gamma,\mathrm{exp.}}/\epsilon_{\gamma,\mathrm{sim.}} = 0.91 \pm 0.03$.

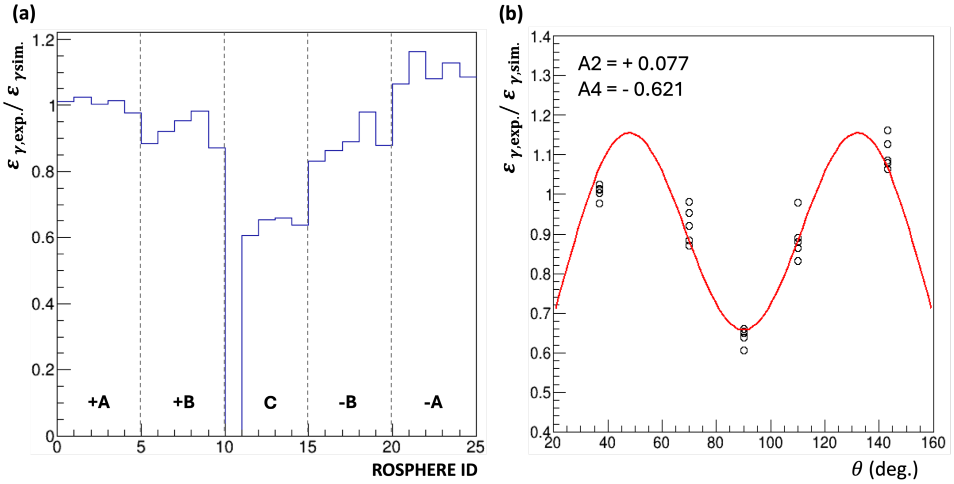

Figure 4.5.3: (a) Ratio of detection efficiencies $\epsilon_{\gamma,\mathrm{exp.}}/\epsilon_{\gamma,\mathrm{sim.}}$ for each of the 24 detectors, and (b) correlation between $\epsilon_{\gamma,\mathrm{exp.}}/\epsilon_{\gamma,\mathrm{sim.}}$ and the angle θ.

4.5.3 Event selection for triple-coincidence events

In the particle-coincidence method described in Sec. 4.4.3, background events from the 3α decay were suppressed by applying energy conditions on the recoil particles, selecting candidate events for the γ decay of the Hoyle state. However, under these conditions, the uncertainty in the thickness of the dead layer on the DSSD surface introduced significant errors in determining the γ-decay probability. Additionally, background events from the excited states of ^{13}C could not be kinematically eliminated, further contributing to the uncertainty in the yield of the α+^{12}C coincidence events. On the other hand, since neither of these background sources emits γ rays, they can be removed by requiring a γ-ray coincidence.

Therefore, in the analysis of triple-coincidence events, no energy restriction, indicated in Fig. 4.4.5, were applied to the recoil particles. Among the events where the Hoyle state was excited, those satisfying the angular correlation conditions of the scattered and recoil particles shown in Fig. 4.4.3 and 4.4.4 and where a γ ray was detected by ROSPHERE were selected as candidate γ decay events.

Time correlation between α and γ

Figure 4.5.4(a) shows the time difference spectrum $t_\gamma - t_\alpha$ between the γ rays detected by ROSPHERE and the scattered α particles for the candidate γ decay events from the Hoyle state. A sharp peak corresponding to true coincidence events was observed between the two dashed lines, while a continuous distribution from accidental coincidence events was seen in the other regions. The region marked by the black arrows was defined as "true events", and the region marked by the blue arrows as "accidental events". The γ-ray spectra for both were compared in Fig. 4.5.4(b). The accidental event spectrum was scaled to account for the time window used for the true events. In the true event spectrum, both the total-absorption and single escape peaks of the 4.44 MeV and 3.21 MeV γ rays were observed. In contrast, the accidental event spectrum showed a continuous background distribution with a peak at 1.44 MeV, attributed to the self-decay of ^{138}La.

Background estimation

By applying the α+^{12}C+γ triple-coincidence condition, the background events from the 3α decay of the Hoyle state and the excited states of ^{13}C were effectively eliminated. Figure 4.5.5(a) shows the energy correlation between the scattered α particle and the recoil particle coincident with a γ ray in the energy range $2.6 \leq E_\gamma \leq 4.6$ MeV. Compared with Fig. 4.4.5, the single-α events originating from the continuous distribution of 3α decay, previously observed inside the black box, were no longer present. On

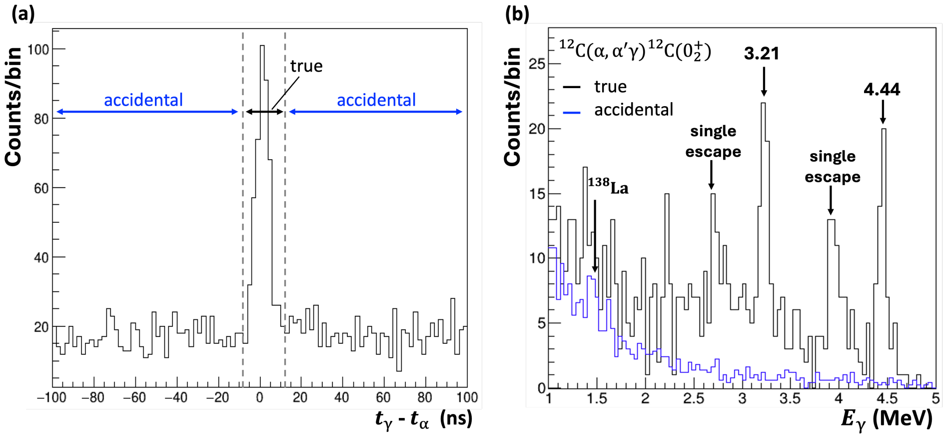

Figure 4.5.4: (a) Time difference $t_\gamma - t_\alpha$ between γ rays and scattered α particles. (b) γ-ray energy spectra for true and accidental events.

the other hand, within the purple box, events corresponding to the excited states of ^{16}O (E_x = 8.87, 9.59 MeV) emitting γ rays and being detected as triple-coincidence events were observed. These events were completely removed by applying a gate to the region indicated by the red line in the figure.

Figure 4.5.5(b) shows the excitation energy spectrum of the triple-coincidence events after applying the gating condition from Fig. 4.5.5(a). The red line represents the spectrum obtained using the $^{\mathrm{nat}}$C target, while the black line corresponds to the spectrum obtained using the ^{13}C target. Compared to Fig. 4.4.7, a clear peak for the Hoyle state is observed with a significantly improved signal-to-noise ratio (S/N). Using the spectrum obtained with the ^{13}C target, it was determined that 6 background events originating from ^{13}C were present in the E_x = 7.4–7.9 MeV region. These background events were subtracted from the number of triple-coincidence events obtained in the following analysis.

Yield of triple-coincidence events

To determine the yield of triple-coincidence events, the γ-ray spectrum was created after subtracting accidental events, and it was fitted using the simulated γ-ray spectrum. In the simulation, as shown in Table 4.2.6, it was assumed that all Hoyle states, corresponding to the total number of excited events N_H, underwent γ decay and generated N_H isotropically emitted 4.44

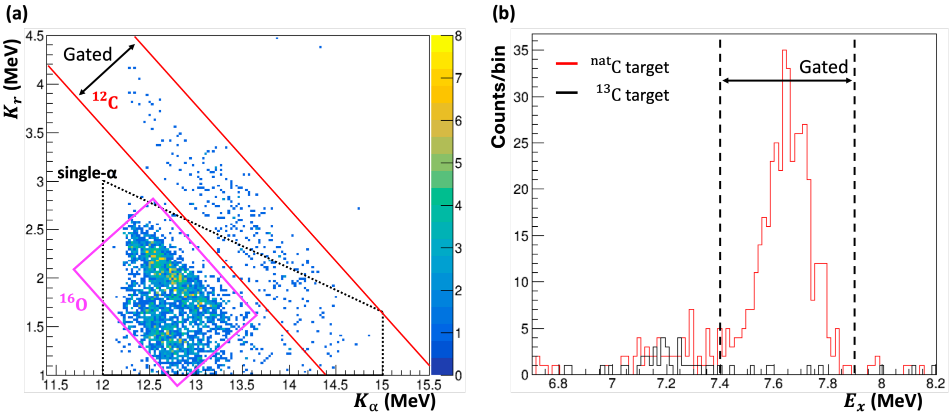

Figure 4.5.5: (a) Energy correlation between the scattered α particle and the recoil particle coincident with a γ ray of $E_\gamma \geq 2.6$ MeV. (b) Excitation energy spectrum of the triple-coincidence events.

MeV and 3.21 MeV γ rays, respectively. Therefore, the scaling factor of the simulated γ-ray spectrum is proportional to the γ decay probability of the Hoyle state.

Since the statistics of the γ rays in the triple-coincidence events were limited, and the uncertainty in each bin was assumed to follow a Poisson distribution, the maximum likelihood method was used for the optimization. The definition and detailed fitting procedure using the maximum likelihood method are described in Appendix B.

Figure 4.5.6(a) shows the experimental data and the fitted simulated spectrum, represented by black and red lines, respectively. The simulated spectrum includes both the 4.44 MeV and 3.21 MeV γ rays. The fit was performed within the energy range of $E_\gamma = 2.6$–4.6 MeV, indicated by the shaded gray region. The log-likelihood function $\log L$ was calculated while varying the scaling factor f of the simulated data. The results are shown in Fig. 4.5.6(b). By fitting this distribution with a quadratic function (red line), the scaling factor that maximized the log-likelihood function was determined to be $f = 3.08 \times 10^4$ with a statistical uncertainty of 0.17×10^4.

Particle-coincidence efficiency with DSSD

The particle-coincidence efficiency in the triple-coincidence analysis was re-evaluated. As discussed in Sec. 4.4.3, the same angular correlation con-

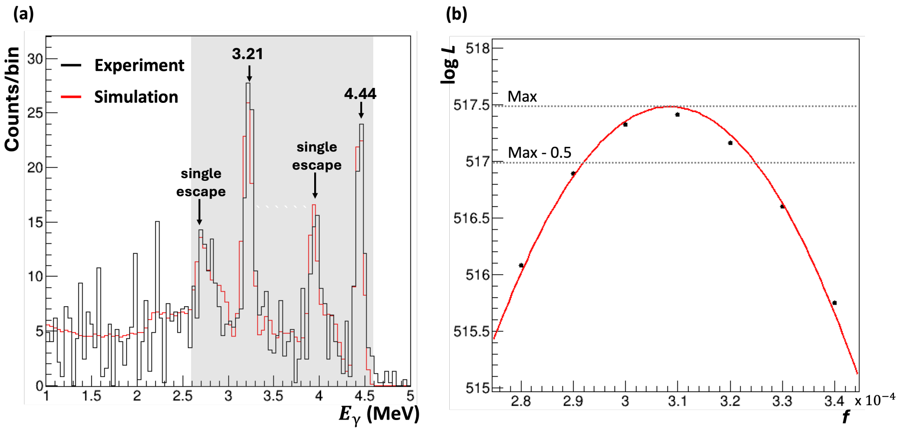

Figure 4.5.6: (a) γ-ray energy spectrum from the experimental data and the fitted simulation. (b) Log-likelihood function $\log L$ as a function of the scaling factor f.

ditions between the scattered α particle and the recoil particle, as shown in Figures 4.4.3 and 4.4.4, were applied. However, in the triple-coincidence method, since the detection requires a coincidence with a γ ray, the scattered α particle and ^{12}C are not distinguished on the DSSD. Therefore, by applying the gate condition shown by the red line in Figure 4.5.5(a), ^{12}C particles with energies as low as 1.0 MeV could be detected.

A simulation was conducted considering these two gating conditions, and the detection efficiency was determined to be $\epsilon_{\mathrm{Si}} = 0.846$.

While the variation in dead layer thickness introduced significant systematic uncertainty in the detection efficiency in the particle-coincidence method, it had no impact in the triple-coincidence method due to the broader energy acceptance for ^{12}C.

4.5.4 γ-decay probability with triple-coincidence

Based on the above analysis, the γ-decay probability Γ_γ/Γ of the Hoyle state was estimated using the triple-coincidence method. The γ-decay probability of the Hoyle state is given by Eq. (4.6). On the other hand, the scaling factor f determined in Fig. 4.5.6 is expressed as :

$$f = \frac{N_\gamma}{N_H} \times \frac{1}{\epsilon_{\gamma,\mathrm{sim.}}} \tag{4.12}$$

Therefore, the γ-decay probability Γ_γ/Γ can be rewritten using f as shown in Eq. (4.13).

$$\frac{\Gamma_\gamma}{\Gamma} = f \times \frac{1}{\epsilon_{\mathrm{Si}} \cdot \epsilon_{\gamma,\mathrm{exp.}}/\epsilon_{\gamma,\mathrm{sim.}}} \tag{4.13}$$

Here, the previously determined values $\epsilon_{\gamma,\mathrm{exp.}}/\epsilon_{\gamma,\mathrm{sim.}} = 0.91 \pm 0.03$ (sys.) and $\epsilon_{\mathrm{Si}} = 0.846$ were used. The maximum likelihood fitting was performed for five different energy regions, and the scaling factor f and the ratio Γ_γ/Γ were determined. Table 4.5.4 summarizes the parameters used in the calculation of Γ_γ/Γ.

Fitting region (MeV)	f (10^{-4})	Γ_γ/Γ (10^{-4})
4.2–4.6	2.99 ± 0.35 (sta.)	3.89 ± 0.46 (sta.) $\pm\, 0.16$ (sys.)
3.8–4.6	3.07 ± 0.30 (sta.)	3.99 ± 0.39 (sta.) $\pm\, 0.16$ (sys.)
3.4–4.6	3.08 ± 0.27 (sta.)	4.00 ± 0.35 (sta.) $\pm\, 0.16$ (sys.)
3.0–4.6	3.13 ± 0.21 (sta.)	4.11 ± 0.27 (sta.) $\pm\, 0.16$ (sys.)
2.6–4.6	3.08 ± 0.17 (sta.)	4.00 ± 0.22 (sta.) $\pm\, 0.16$ (sys.)

Table 4.6: The obtained Γ_γ/Γ and the parameters used for its calculation.

As a result of the analysis, Γ_γ/Γ was estimated in five energy regions, and it was found that the values remained consistent across these regions. This consistency is attributed to the good agreement between the model function generated in the simulation used for the maximum likelihood method and the actual spectrum. In this experiment, as shown in Fig. 4.5.1, the spectrum of the 4.44-MeV γ ray from the first excited state of ^{12}C was well reproduced by the simulation. Additionally, as shown in Fig. 4.5.6, the shape of the spectrum containing the 4.44 MeV and 3.21 MeV γ rays in a 1:1 ratio was also reasonably reproduced.

The variation in the values of Γ_γ/Γ across the energy regions is attributed to the shape of the fitting function. Therefore, the variance in the Γ_γ/Γ values among the different energy regions was considered as a systematic uncertainty.

Based on the results of this analysis, the γ decay probability in this experiment was determined using the data from the most statistically significant energy region of $E_\gamma = 2.6$–4.6 MeV as $\Gamma_\gamma/\Gamma = 4.00(27) \times 10^{-4}$.

Chapter 5

Discussion

In this study, a new method combining a DSSD and a large LaBr3 detector array was adopted to solve the puzzle on the γ-decay probability of the Hoyle state. This method enabled the $\alpha + ^{12}\mathrm{C} + \gamma$ triple coincidence measurement, and successfully determined the γ-decay probability of the Hoyle state as $\Gamma_\gamma/\Gamma = 4.00(27) \times 10^{-4}$. The triple coincidence measurement could resolve discrepancies among results obtained by conventional methods measuring either the surviving ^{12}C or de-excitation γ rays. During the same period as our measurement, several research groups conducted re-measurements of the γ-decay probability [4–7], and some of their results have already been published. This chapter discusses the puzzle on the basis of the recent re-measurements including this work.

5.1 Recent results

Kibédi *et al.* pointed out that the ^{12}C detection method might be affected by a significant amount of backgrounds originating from the 3α decay of ^{12}C. Several experiments including this work with different methods were immediately conducted to verify the result, and the Γ_γ/Γ values were reported as summarized in Fig. 5.1.1. Below, an overview of each experiment and its results are presented.

5.1.1 ^{12}C-Detection Method

As described in Sec. 1.4, the ^{12}C-detection method involves simultaneous detection of the scattered beam particles and the ^{12}C nucleus surviving after

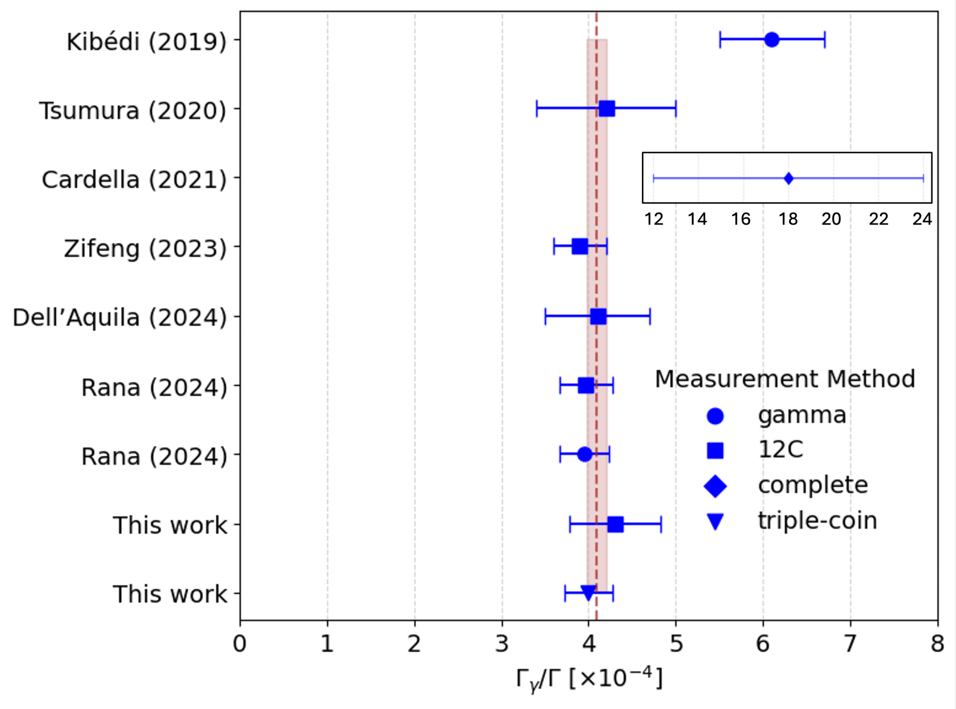

Figure 5.1.1: Summary of the γ-decay probability values reported after the study by Kibédi *et al.*

the γ-ray emission. The $\Gamma_{\text{rad}}/\Gamma$ value is estimated from the yield ratio of the scattered particle to the surviving ^{12}C nucleus. This method has been widely used in previous measurements due to its high detection efficiency achieved by detecting only charged particles with Si detectors. However, a difficulty of this method is huge backgrounds caused by 3α-decay events of ^{12}C and neutron emission events from ^{13}C contaminants in $^{\text{nat}}$C target. Recently, four research groups employed this method to determine Γ_γ/Γ.

Tsumura *et al.* (2020) [3]

In Ref. [3], Tsumura *et al.* measured inelastic scattering of protons and ^{12}C under inverse kinematic conditions, and reported the radiative-decay probability of the Hoyle state as well as those of the 1_1^+ and 3_1^- states for the first time since the work by Kibedi *et al.* [2]. A ^{12}C beam accelerated by the AVF cyclotron at Research Center for Nulcear Physics, Osaka University was irradiated onto a thin solid hydrogen target developed by the authors, and the recoil protons were detected with a DSSD-GAGG telescope. The PID of the recoil protons was performed using the E–ΔE method. The excitation-energy spectrum of ^{12}C was constructed from energies and angles of the recoil protons. ^{12}C after the γ decay of the Hoyle state was momentum-analyzed by the Grand Raiden (GR) spectrometer, and detected with the focal-plane detector, which consisted of the two multiwire-drift chambers (MWDCs) and two plastic scintillators (PS1, PS2). Because a large number of α particles also reached the focal plane, the plastic scintillators were designed to discriminate ^{12}C from α particles by anti-coincidence between them. Namely, the thickness of PS1 was optimized so that ^{12}C stopped at PS1 but α particles penetrated PS1 and hit PS2. The accidental coincidence events were eliminated by utilizing the kinematical correlation between ^{12}C and recoil proton.

As a result, the yield of the recoil protons exciting the Hoyle state was estimated to be $2.06(3) \times 10^7$, while that of the coincidence events between the surviving ^{12}C and recoil proton was 957(79). The α+^{12}C detection efficiency for this experiment was estimated via MC calculations to be 0.109(19), resulting in the radiative-decay probability of $\Gamma_{\text{rad}}/\Gamma = 4.3(8) \times 10^{-4}$, which corresponds to the γ-decay probability of $\Gamma_\gamma/\Gamma = 4.2(8) \times 10^{-4}$. The accuracy of the radiative- and γ-decay probabilities was limited by significant systematic uncertainty in the detection efficiency. This arose from the small angular and momentum acceptances for the ^{12}C and α-particle pair, as the experimental setup was optimized for the 3^-_1 state rather than the Hoyle state.

Luo *et al.* (2023) [5]

Luo *et al*. measured inelastic scattering of α particles and ^{12}C under normal kinematic conditions and determined the radiative-decay probability of the Hoyle state [5]. An isotope-enriched ^{12}C target was bombarded by α particles at 40 MeV accelerated by the K150 cyclotron at the Cyclotron Institute in Texas A&M University. The scattered α particles were detected with a DSSD telescope, while the recoil particles were momentum-analyzed by a Multipole–Dipole–Multipole (MDM) spectrometer, and subsequently detected with the Texas Parallel-Plate Avalanche Counter System (TexPPACS) placed downstream.

As a result, the yield of the scattered α particles exciting the Hoyle state was determined to be $1.570(37) \times 10^6$, while that of the coincidence events between the scattered α particle and surviving ^{12}C was 291(21). The α+^{12}C detection efficiency was evaluated as 0.95(3) by MC simulations with Geant4, and its uncertainty was estimated using the experimental data for the ^{12}C(2_1^+). Finally, the radiative-decay probability was determined to be $\Gamma_{\mathrm{rad}}/\Gamma = 4.00(27) \times 10^{-4}$, which corresponds to the γ-decay probability of $\Gamma_{\gamma}/\Gamma = 3.93(34) \times 10^{-4}$. This value was more than 5σ away from the result by Kibedi *et al.* and supported the previous literature value.

Dell'Aquila *et al.* (2024) [6]

Dell'Aquila *et al.* determined the radiative-decay prorbability using a transfer reaction [6] instead of inelastic scatterings employed by Tsumura *et al.* [3] and Luo *et al.* [5]. A deuteron beam at 2.7 MeV accelerated by the CN Van de Graaff accelerator at the IFIN Institute was irradiated onto a melamine ($C_3H_6N_6$) target, and the ^{14}N(d,α)^{12}C reaction was used to populate the Hoyle state. The scattered α particles and recoiled ^{12}C were measured using two double-layer Si detector telescopes. Si detector telescopes placed at backward (90°) and forward angles (64.8°), respectively. The anti-coincidence condition between the two layers in both forward and backward detectors was imposed to eliminate background particles due to other contaminant reactions. Events where the Hoyle state was populated were identified by selecting the energy detected with the backward detector. Thanks to the kinematic correlation between the forward and backward particles, ^{12}C from the radiative decay of the Hoyle state could be energetically distinguished from the 3α decay even without PID in the forward detector.

As a result, the yield of the α particles to populate the Hoyle state at the backward detector was determined to be $1.25(3) \times 10^5$, while that of the coincidence events with the surviving ^{12}C detected by the forward detector was 53.

The experimental setup was designed to achieve a coincidence efficiency of 100%, and thus no systematic uncertainty had to be considered for the efficiency. Finally, the radiative-decay probability was determined to be $\Gamma_{\mathrm{rad}}/\Gamma = 4.1(6) \times 10^{-4}$.

This experiment employed a unique method that imposed strong constraints on the momentum vectors of the α particles and ^{12}C, allowing the complete elimination of α particles from 3α decay without PID. However, the small solid angle of the Si detectors reduced the yield, leading to large statistical uncertainties of 15%.

Rana *et al.* (2024) [7]

Rana *et al.* followed the commonly used method where inelastically scattered proton and recoil ^{12}C were detected under the normal kinematic conditions [7]. A proton beam at 11 MeV accelerated by the K130 cyclotron at the Variable Energy Cyclotron Centre, Kolkata was irradiated onto a $^{\mathrm{nat}}$C target, and the scattered protons were detected with a Si detector telescope placed at backward angles centered at 125°. This telescope consisted of a thin ($\sim 20\,\mu$m) single-sided Si strip detector a ΔE detector and a DSSD with as an E detector. Trigger signals were generated using a ΔE detector, and the protons populating the ground and first excited states of ^{12}C were excluded from the trigger by appropriately setting energy thresholds. The recoil particles were detected with a DSSD placed 25 cm from the target and centered at 18°, and PID was performed using the ToF method.

As a result, yield of the scattered protons exciting the Hoyle state was reported as $4.37(2) \times 10^6$, while that of the coincidence events between the scattered proton and surviving ^{12}C was 1501(39). The $\alpha +^{12}$C detection efficiency was calculated to be 85% through MC simulations, and systematic uncertainty was estimated to be smaller than 1.5% by comparing experimental results for the ground and first excited states of ^{12}C. Finally the radiative-decay probability was determined to be $\Gamma_{\mathrm{rad}}/\Gamma = 3.97(30) \times 10^{-4}$.

5.1.2 γ-Detection Method

As described in Sec. 1.4, the γ-detection method involves simultaneous detection of the scattered particles populating the Hoyle state and two de-excitation γ rays with respective energies of 4.44 and 3.21 MeV. The γ-decay probability is estimated from the yield ratio. In γ-ray detection, the probability of full absorption of γ rays in the MeV energy range is low, making it challenging to increase the yield of γ–γ coincidence events. Moreover, the interaction between γ rays and the scintillator is probabilistic, and the angular correlation between the two γ rays further complicates the accurate determination of the coincidence detection efficiency. For these reasons, only a limited number of studies have reported results using the γ-detection method. However, Kibédi *et al.* reported a 50% larger value of the γ-decay probability than the previous literature value [1] by using this method [2], and this result strongly motivated verification experiments using the same approach. Recently, Rana *et al.* measured the γ-decay probability using this method [7].

Rana *et al.* (2024) [7]

Rana *et al.* reported the γ-detection experiment in the same paper [7] with their the ^{12}C-detection experiment described in the previous section. To detect γ rays, 50 BaF_2 detectors were newly installed around the scattering chamber, and the $^{\mathrm{nat}}$C target was replaced with a thicker one to enhance the yield. Since recoil ^{12}C stopped in the target, ^{12}C could not be detected in this setup. The scattered α particles were detected with the two Si telescopes and each telescope consisted of a thin SSSD and thick DSSD. Trigger signals were generated when one of the SSSDs detected a charged particle. This condition was different from the ^{12}C-detection experiment, which required coincidence between the SSSD and DSSD, because energies of the scattered protons were lower than those in the ^{12}C-detection experiment due to the thick $^{\mathrm{nat}}$C target. Two γ rays were detected by different BaF_2 detectors, and events with a total detected energy near 7.65 MeV were selected.

As a result, the yield of the scattered protons populating the Hoyle state was determined to be $1.93(2) \times 10^9$, while that of the coincidence events between the scattered protons and two γ rays was 665(29) events. This statistics was three times higher than that in Kibédi *et al.* [2].

The simultaneous detection efficiency of the two γ rays was calclated as a product of the detection efficiencies for the 3.21-MeV and 4.44-MeV γ rays to be $2.330(7)\% \times 1.747(7)\% = 0.0407(2)\%$. The angular correlation between the two γ rays emitted from the cascade decay of the Hoyle state was taken into accout by introducing a correction factor. The detection efficiency and the correction factor were estimated using MC simulations with Geant4. The accuracy of the simulation was experimentally verified using the 4.98 MeV state of ^{28}Si. This state undergoes a 100% 0–2–0 cascade decay, allowing the experimental detection efficiency to be determined from the ratio of singles and coincidence events. The difference between the experimental and simulated detection efficiencies was smaller than 1%. Finally the γ-decay probability was determined to be $\Gamma_\gamma/\Gamma = 3.95(28) \times 10^{-4}$.

5.1.3 Complete Detection Method

The complete detection method involves the simultaneous detection of the scattered beam particles, recoiled ^{12}C, and the two emitted γ rays. This method combines two conventional detection methods, and provides a direct approach to resolving the possible systematic bias due to the measurement method noted by Kibédi *et al.* This method can significantly suppress background levels by detecting all the four particles emitted from the two-body reaction populating the Hoyle state. However, this method is statistically challenging due to low detection efficiency for two γ rays and use of thin targets for detecting low-energy charged particles. Therefore, no attempt at implementing the coplete detection method had been reported. Recently, using this method, Caldera *et al.* measured the γ-decay probability of the Hoyle state [4].

Cardella *et al.* (2021) [4]

Cardella *et al.* addressed the issue of extremely low yields by using the large solid-angle charged-particle and γ-ray detector CHIMERA. CHIMERA consists of 1,192 Si-CsI(Tl) telescopes covering 94% of the 4π solid angle. A-64 MeV α beam accelerated by the Superconducting Cyclotron at INFN-LNS in Catania was irradiated onto a $^{\mathrm{nat}}$C target placed at the center of CHIMERA. Charged particles were identified using the E–ΔE method and the ToF method.

The yield of the Hoyle state was determined from the number of the events in which the scattered α particle and the decay 3α particles from the Hoyle state were detected in coincidence. The production of the Hoyle state was identified by the invariant mass of the 3α particles. The detection efficiency for the decay 3α particles was evaluated by the MC simulation.

To select the quadruple coincidence events between the scattered α particle, the two γ rays, and the surviving ^{12}C, event selection based on the missing energy ($Q_{\mathrm{ME}} = E_{\alpha} + E_{^{12}\mathrm{C}} - E_{\mathrm{beam}}$) and the γ-ray energies was employed. By requiring $Q_{\mathrm{ME}} \sim 7.65$ MeV and detection of two γ rays at 4.44 and 3.21 MeV, the yield of the quadruple coincidence events was determined to be 12.0(38).

The energy resolution of the CsI(Tl) detectors was approximately 10% for few-MeV γ rays, and full absorption events could not be distinguished from single escape events. The coincidence detection efficiency of the two γ rays was calculated using the single-energy detection efficiencies for the 4.44-MeV and 3.21-MeVγ rays obtained via Geant4 simulations. Since CHIMERA covers nearly the entire 4π solid angle, no angular correlation correction had to applied. The accuracy of the simulations was verified using the first excited state of ^{12}C, and the systematic uncertainty was estimated to be approximately 1%. From these analyses, the γ-decay probability $\Gamma_\gamma = 1.8(6) \times 10^{-3}$ was determined.

5.1.4 Comparison with resent studies

Several experiments using different methods, including this work, were conducted to verify the γ-decay probability. As a result, the γ-decay probability measured by conventional methods converged to the previous literature values. Our results obtained using the ^{12}C-detection method also followed the same value.

On the other hand, the first measurement of quadruple coincidence events was conducted using the large solid-angle detector CHIMERA. The reported γ-decay probability was significantly larger than both the previous literature values and the result by Kibédi *et al.* As a possible explanation for this large γ-decay probability, they suggested the existence of an Efimov state [59] near the Hoyle state with a large γ-ray decay width. However, if this hypothesis were correct, a similar increase in the γ-decay probability should be observed in all other measurements as well. Moreover, It should be noted that the values were possibly overestimated due to the following reasons. In the total γ-energy spectrum of the quadruple coincidence events obtained in this experiment, a sharp peak structure corresponding to accidental coincidences from the 4.44-MeV γ ray was observed. The background correction for accidental coincidences performed in this analysis failed to eliminate the sharp peak structure around 4.44 MeV, but this issue was not addressed in the paper. Therefore, the background subtraction was likely insufficient, leading to an overestimation of the γ-decay probability.

We measured the γ-decay probability using the triple coincedence method. This method involves the simultaneous detection of the scattered beam particle, recoil ^{12}C and one of the emitted γ rays from the Hoyle state. Similar to the complete detection method, this method also provides a direct approach to resolving the systematic bias in the measurement method. However, the triple coincidence measurement is still challenging in similar to the complete detection due to the use of thin targets and low γ detection efficiency, and there have been no successful measurements by using this method. In this experiment, we realized the triple coincidence method by combining the following three techniques.

Charged particle detection with large solid-angle DSSD

We placed a DSSD 40 mm downstream of the target, enabling simultaneous detection of scattered α particles and recoiled ^{12}C nuclei over a large solid angle. This setup allowed us to obtain 7.6×10^6 single events as shown in Table 4.2.6. Taking into account the coincidence detection efficiency of the DSSD, this method achieved the highest yield compared to the recent experiments using the ^{12}C detection method [3, 5–7]. The DSSD is divided into concentric rings, providing high angular resolution for the scattering angle θ of emitted charged particles. This capability enabled the complete kinematic elimination of background events originating from the 2_1^+ state at $E_x = 4.44$ MeV of ^{12}C. Furthermore, the compact measurement system with the DSSD increased the angular acceptance of the γ-ray detection.

Particle identification using the PSD method

In the recent experiments using the ^{12}C detection method, particle identification was performed using the E–ΔE method and the ToF method. In this study, we attempted at particle identification using a novel approach called the PSD method. By acquiring waveforms from the DSSD and calculating the discrimination parameter A_{max}, we successfully identified scattered α particles from protons and ^{12}C. The systematic uncertainty in spectral fitting for single events after particle identification was approximately 1%, comparable to experiments that employed the E–ΔE method. On the other hand, the PSD method could not distinguish between low-energy α particles and ^{12}C. To discriminate between this α particles and ^{12}C, the high-energy condition shown in Fig. 4.4.5 was applied. Consequently, as described in 4.4.3, the detection efficiency of the DSSD significantly decreased, which make it difficult to accurately determine the Γ_γ/Γ value using the ^{12}C detection method. This issue was resolved by taking coincidences with γ rays.

γ-ray detection with ROSPHERE

In this study, we used ROSPHERE to measure γ rays emitted from the Hoyle state with high detection efficiency and energy resolution of $LaBr_3$ detectors. The γ-ray detection efficiency was higher than that of Rana *et al.* [7], and yielded sufficient triple coincidence event. A similar study by Cardella *et al.* achieved even higher γ-ray detection efficiency using CsI(Tl) detectors. However, the energy resolution was oas low as 10%, which resulted in large systematic uncertainties and compromised the reliability of the experimental results. The background yield for triple coincidence events was determined through the analysis in Sec. 4.5.3. Despite presence of significant background from α particles originating due to accidental coincidence with 3α decay, an excellent S/N ratio was achieved, as shown in Fig. 4.5.4 (b). This can be attributed to the use of a DC beam in this study. In contrast, the experiment by Cardella *et al.* employed an RF beam, and γ-decay events were difficult to identify because they were buried in a large accidental background.

5.2 Conclusion

Various measurement approaches have been employed to solve the puzzle of the γ-decay probability of the Hoyle state. In studies utilizing the ^{12}C-detection method [3,5–7], background events originating from 3α decay were properly handled in each experiment, and all these studies yielded results consistent with the previous literature value adapted in Ref. [1], but contradicts the new value by Kibedi et al [2]. Similarly, studies employing the γ-detection method [7] followed the analysis method of Kibédi *et al.*, also supporting the previous literature value. Furthermore, a measurement combining these two methods was attempted [4], but the evaluation of the background was ambiguous and the reliability of the data remained in doubt. In contrast, our study achieved high yields and low background levels using a novel approach, which yielded results supporting the previous literature value.

Triple coincidence method represents a direct approach to resolving the systematic bias in the measurement method. Therefore, we concluded that the puzzle on the γ-decay probability of the Hoyle state is now finally solved, and the previous literature value can be reliably used in the study of nucleosynthesis in the universe.

Chapter 6

Summary

In this thesis, the γ-decay probability of the Hoyle state has been measured using the $\alpha +^{12}$ C + γ triple-coincidence measurement. The aim of this research was to solve the recently reported discrepancy in the γ-decay probability of the Hoyle state. We populated the Hoyle state in ^{12}C by the α+^{12}C scattering using an α particle beam at $E_{\text{beam}} = 25$ MeV at the tandem accelerator facility of IFIN-HH, and emitted charged particles were detected by a DSSD and γ rays by the ROSPHERE LaBr$_3$ detector array [?]. The charged particle detection with a large solid-angle DSSD and particle identification using the PSD method increased the experimental yield. Furthermore, γ-ray detection with ROSPHERE suppressed significant background from α particles originating due to accidental coincidence with 3α decay, achieving an excellent signal-to-noise ratio. This method enabled high yields and low background levels, and successfully determined the γ-decay probability of the Hoyle state as $\Gamma_\gamma/\Gamma = 4.00(27) \times 10^{-4}$.

Various measurement have been employed to solve the puzzle of the γ-decay probability of the Hoyle state [3–7], and all these studies excepted Ref. [4] yielded results consistent with the previous literature value adapted in Ref. [1], but contradicts the new value by Kibedi *et al.* [2]. Moreover, our measurement using a novel approach also yielded results supporting the previous literature value. Therefore, we concluded that the puzzle on the γ-decay probability of the Hoyle state is now finally solved, and the previous literature value can be reliably used in the study of nucleosynthesis in the universe.

Chapter 7

Acknowledgement

I would like to express my sincere thanks to all those who have supported and guided me throughout this research.

First and foremost, I would like to extend my deepest appreciation to Prof. T. Kawabata, who has guided me over the past seven years, from my undergraduate studies to the completion of my master's and doctoral programs. He respected my ideas and provided an environment where I could conduct my research freely and comfortably. He also offered many valuable and precise suggestions during data analysis and paper writing. I am truly grateful for the significant amount of time he dedicated to me despite his busy schedule, and I deeply appreciate his kindness.

Next, I would like to thank all the collaborators who supported the execution of this experiment. I am particularly grateful to Prof. T. Furuno, who supported me on-site during a five-week experiment in Romania. As this was my first overseas research experience, his presence was incredibly reassuring. He also provided many valuable comments and suggestions on the analysis, alongside Prof. T. Kawabata, which greatly improved the quality of the research. Additionally, I would like to thank Mr. P.-A. Söderström, Mr. S. Aogaki, and the researchers at ELI-NP and IFIN-HH for their technical and administrative support during the experiments. I am especially thankful for their prompt assistance in resolving issues during the beam time.

Furthermore, I would like to express my gratitude to all the members of our research group, both past and present, who have supported me throughout my research life. I am thankful to Prof. Adachi and Mr. Okamoto for their help with experimental preparations and measurements. I am also

grateful to Mr. M. Murata, Mr. K. Inaba, Mr. Y. Fujikawa, Mr. T. Doi, Mr. S. Tsuji, Ms. K. Himi, Mr. Y. Honda, Mr. S. Sakajo, Mr. Y. Lin, Mr. T. Okamura, and Mr. H. Shimojo for their support and advice in various aspects of my research. My seven years of academic life have been fulfilling and meaningful thanks to all of you.

Finally, I would like to express my heartfelt gratitude to my family for their unwavering support. Without their encouragement and support , I would not have been able to complete this research.

Once again, I sincerely thank everyone who has supported and contributed to this research.

Appendix A

Setting of digitizer

In this experiment, a CAEN V1730SB 500 MS/s flash digitizer was used to acquire all data. The V1730SB is equipped with an FPGA that allows users to select and write firmware tailored to their objectives, enabling various types of digital pulse processing (DPP). Six V1730SB units with DPP-PHA firmware were installed for the Si detectors, while four V1730SB units with DPP-PSD firmware were used for ROSPHERE. This appendix describes the specifications of each firmware and the settings applied in this experiment.

A.1 DPP-PHA firmware

The DPP-PHA (Pulse Height Analysis) firmware is designed for real-time analysis optimized for measuring the energy of input signals. By applying two programmable filters to the input signal, it can extract both energy and timing information in real-time. Figure A.1.1 shows a schematic of the signal processing flow in the DPP-PHA firmware.

To extract energy information from the input signal, a trapezoidal filter was applied. The trapezoidal filter can be described using the input signal $x[n]$, the output signal $V_{\mathrm{out}}[n]$, the filter length L, and the delay sample count M, as shown in the following equation:

$$V_{\mathrm{out}}[n] = \frac{1}{L}\sum_{i=0}^{L-1} x[n-i] - \frac{1}{L}\sum_{i=0}^{L-1} x[n-i-M] \tag{A.1}$$

By appropriately setting the filter length L and the number of the delay sample M, the input pulse was converted into a trapezoidal signal with an amplitude proportional to the pulse height (energy), as shown by the green signal in Fig. A.1.1. The average of multiple samples within the flat-top region of this output signal was taken as the peakADC value.

However, in this analysis, a FIR filter was applied to the acquired waveform to implement a CR-RC^n circuit in software and extract the pulse height of the output waveform. Using the FIR filter yielded better energy resolution compared to the trapezoidal filter. Further details on the FIR filtering process are described in Sec. 2.4.

To extract timing information from the input signal, a Trigger and Timing Filter (TTF) was applied. The TTF, shown as the red signal in Fig. A.1.1, performs the second derivative of the input signal. To prevent false triggering caused by high-frequency noise, the input signal was smoothed using a moving average filter over 32 samples before applying the TTF. The output signal of the TTF is bipolar, similar to a CFD, and its zero-crossing point is independent of signal amplitude. Therefore, the detection time (Time tag) was determined as the time of the first zero-crossing point after the TTF output exceeded a preset threshold. The threshold was set to avoid false triggering caused by noise.

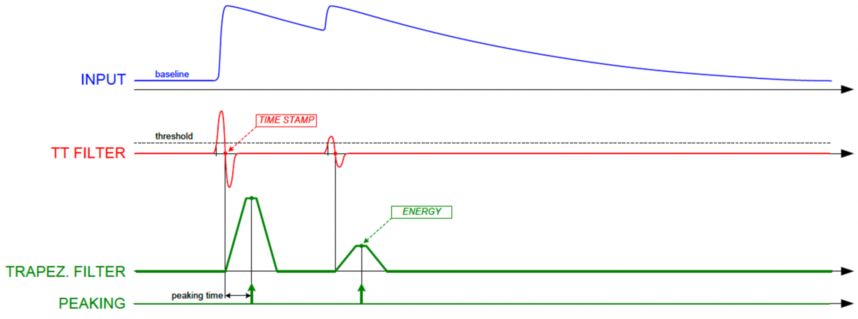

Figure A.1.1: Signal processing schematic of the DPP-PHA firmware. Reproduced from Fig. 4.4 of ref. [60].

A.2 DPP-PSD firmware

The DPP-PSD (Pulse Shape Discrimination) firmware is designed for analyzing the shape of input signals to identify different types of radiation or particles. The DPP-PSD firmware can calculate both the total and delayed partial integrals of the waveform, making it widely used for neutron-γ discrimination with organic scintillator detectors. Figure A.2.1 shows a schematic of the signal processing in the DPP-PSD firmware.

As indicated by the green line in Fig. A.2.1, two types of gates (long gate and short gate) were applied to the detector's output signal. The total integral and the delayed partial integral of the waveform were calculated before and after the trigger.

The trigger timing was determined by implementing a classical CFD method on a digital signal. The input signal was attenuated by a constant fraction f, inverted, and delayed by a fixed time d, before being summed with the original signal. Since the output signal is bipolar, the zero-crossing point was used both as the start time for the long and short gates and as the particle detection time (Time tag).

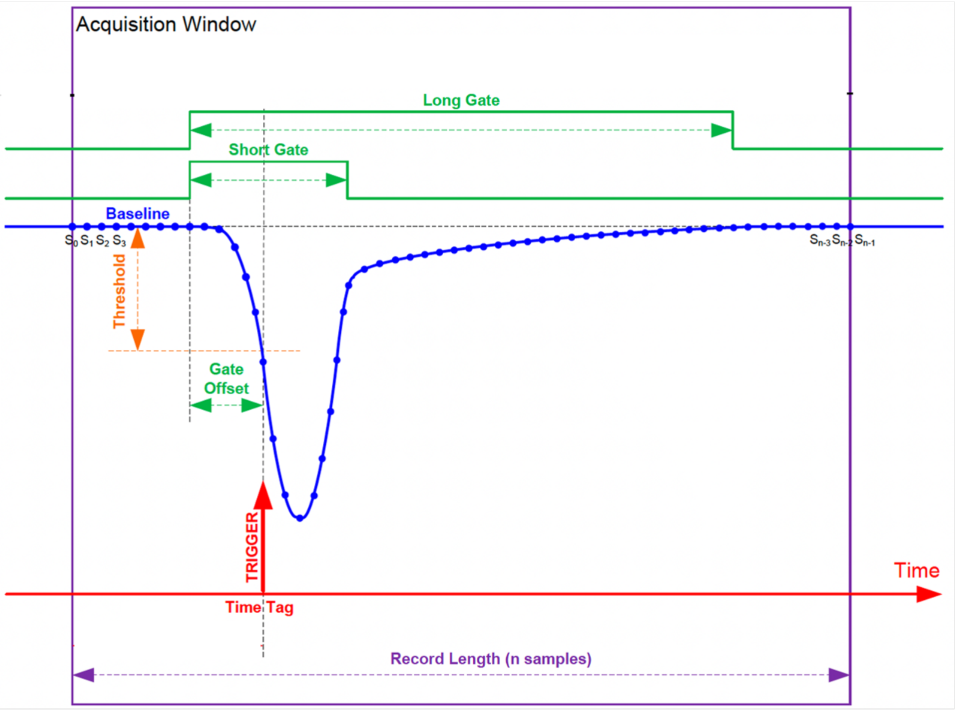

Figure A.2.1: Signal processing schematic of the DPP-PSD firmware. Reproduced from Fig. 2.6 of ref. [60].

Appendix B

Maximum Likelihood Method

B.1 Definition of the Likelihood Function

Let the observed data be denoted by $x_1, x_2, \ldots, x_n$, and assume these data points follow a probability distribution $f(x_i;\theta)$ characterized by the parameter θ. If each data point is independently obtained, the likelihood function $L(\theta)$ for the entire dataset is defined as :

$$L(\theta) = \prod_{i=1}^{n} f(x_i;\theta) \tag{B.1}$$

The likelihood function $L(\theta)$ is a function of the parameter θ and represents the probability of obtaining the observed data given the parameter θ.

B.1.1 Log-Likelihood Function

Since the likelihood function becomes complex to compute as the number of data points increases, the log-likelihood function $\log L(\theta)$ is often used to simplify calculations. The log-likelihood function is expressed as :

$$\log L(\theta) = \sum_{i=1}^{n} \log f(x_i;\theta) \tag{B.2}$$

B.1.2 Derivation of the Maximum Likelihood Estimator

The maximum likelihood estimator $\hat{\theta}$ is obtained by maximizing the log-likelihood function $\log L(\theta)$ with respect to the parameter θ. Specifically, $\hat{\theta}$ satisfies the condition:

$$\left.\frac{\partial \log L(\theta)}{\partial \theta}\right|_{\theta=\hat{\theta}} = 0 \tag{B.3}$$

Solving this equation provides the parameter estimate $\hat{\theta}$.

B.1.3 Error Estimation of Parameters

The statistical error of the parameter $\hat{\theta}$ obtained by the maximum likelihood method can be evaluated using the inverse of the Fisher information $I(\theta)$. The Fisher information is defined as :

$$I(\theta) = -E\left[\frac{\partial^2 \log L(\theta)}{\partial \theta^2}\right] \tag{B.4}$$

The variance of the parameter error σ^2 is then calculated as :

$$\sigma^2 = I(\hat{\theta})^{-1} \tag{B.5}$$

When the log-likelihood function can be approximated by a quadratic function of the form:

$$\log L(\theta) = -a(\theta - \hat{\theta})^2 + C \tag{B.6}$$

it follows that at the maximum likelihood estimate $\hat{\theta}$:

$$\log L(\hat{\theta}) = C \tag{B.7}$$

and at one standard deviation from the estimate:

$$\log L(\hat{\theta} \pm \sigma) = C - \frac{1}{2} \tag{B.8}$$

Therefore, the points where $\log L(\theta)$ decreases by 0.5 from its maximum value correspond to the $\pm 1\sigma$ error range.

Bibliography

[1] J. Kelley, J. Purcell, and C. Sheu, Energy levels of light nuclei A=12, Nuclear Physics A **968**, 71 (2017).

[2] T. Kibédi, B. Alshahrani, A. E. Stuchbery, A. C. Larsen, A. Görgen, S. Siem, M. Guttormsen, F. Giacoppo, A. I. Morales, E. Sahin, G. M. Tveten, F. L. B. Garrote, L. C. Campo, T. K. Eriksen, M. Klintefjord, S. Maharramova, H.-T. Nyhus, T. G. Tornyi, T. Renstrøm, and W. Paulsen, Radiative width of the Hoyle state from γ-ray spectroscopy, Phys. Rev. Lett. **125**, 182701 (2020).

[3] M. Tsumura, T. Kawabata, Y. Takahashi, S. Adachi, H. Akimune, S. Ashikaga, T. Baba, Y. Fujikawa, H. Fujimura, H. Fujioka, T. Furuno, T. Hashimoto, T. Harada, M. Ichikawa, K. Inaba, Y. Ishii, N. Itagaki, M. Itoh, C. Iwamoto, N. Kobayashi, A. Koshikawa, S. Kubono, Y. Maeda, Y. Matsuda, S. Matsumoto, K. Miki, T. Morimoto, M. Murata, T. Nanamura, I. Ou, S. Sakaguchi, A. Sakaue, M. Sferrazza, K. N. Suzuki, T. Takeda, A. Tamii, K. Watanabe, Y. N. Watanabe, H. P. Yoshida, and J. Zenihiro, First experimental determination of the radiative-decay probability of the 3^- state in ^{12}C for estimating the triple alpha reaction rate in high temperature environments, Physics Letters B **817**, 136283 (2021).

[4] G. Cardella, F. Favela, N. S. Martorana, L. Acosta, A. Camaiani, E. De Filippo, N. Gelli, E. Geraci, B. Gnoffo, C. Guazzoni, G. Immè, D. J. Marín-Lámbarri, G. Lanzalone, I. Lombardo, L. Lo Monaco, C. Maiolino, A. Nannini, A. Pagano, E. V. Pagano, M. Papa, S. Pirrone, G. Politi, E. Pollacco, L. Quattrocchi, F. Risitano, F. Rizzo, P. Russotto, V. L. Sicari, D. Santonocito, A. Trifirò, and M. Trimarchi, Inves-

tigating γ-ray decay of excited ^{12}C levels with a multifold coincidence analysis, Phys. Rev. C **104**, 064315 (2021).

[5] Z. Luo, M. Barbui, J. Bishop, G. Chubarian, V. Z. Goldberg, E. Harris, E. Koshchiy, C. E. Parker, M. Roosa, A. Saastamoinen, D. P. Scriven, and G. V. Rogachev, Radiative decay branching ratio of the Hoyle state, Phys. Rev. C **109**, 025801 (2024).

[6] D. Dell'Aquila, I. Lombardo, L. Redigolo, M. Vigilante, F. Angelini, L. Baldesi, S. Barlini, A. Best, A. Camaiani, G. Casini, C. Ciampi, M. Cicerchia, M. D'Andrea, J. Diklić, D. Fabris, B. G. Servin, A. Gottardo, F. Gramegna, G. Imbriani, T. Marchi, A. Massara, D. Mengoni, A. Ordine, L. Palada, G. Pasquali, S. Piantelli, E. Pilotto, D. Rapagnani, M. Sigmund, N. Soić, A. Stefanini, D. Stramaccioni, D. Tagnani, I. Tišma, S. Valdré, G. Verde, and N. Vukman, Clarifying the radiative decay of the Hoyle state with charged-particle spectroscopy, Scientific Reports **14**, Article 68415 (2024).

[7] T. Rana, D. Pandit, S. Manna, S. Kundu, K. Banerjee, A. Sen, R. Pandey, G. Mukherjee, T. Ghosh, S. Nayak, R. Shil, P. Karmakar, K. Atreya, K. Rani, D. Paul, R. Santra, A. Sultana, S. Basu, S. Pal, S. Sadhukhan, D. Mondal, S. Mukhopadhyay, S. Bhattacharya, S. Pal, P. Pant, P. Roy, S. M. Ali, S. Mondal, A. De, B. Dey, R. Datta, S. Bhattacharya, and C. Bhattacharya, New measurement of the Hoyle state radiative transition width, Physics Letters B **859**, 139083 (2024).

[8] I. J. Thompson and F. M. Nunes, *Nuclear Reactions for Astrophysics: Principles, Calculation and Applications of Low-Energy Reactions* (Cambridge University Press 2009).

[9] R. A. Alpher, H. Bethe, and G. Gamow, The origin of chemical elements, Phys. Rev. **73**, 803 (1948).

[10] LIGO Scientific Collaboration and Virgo Collaboration, GW170817: Observation of gravitational waves from a binary neutron star inspiral, Phys. Rev. Lett. **119**, 161101 (2017).

[11] F. Käppeler, R. Gallino, S. Bisterzo, and W. Aoki, The *s* process: Nuclear physics, stellar models, and observations, Rev. Mod. Phys. **83**, 157 (2011).

[12] E. E. Salpeter, Nuclear reactions in stars without hydrogen., apj **115**, 326 (1952).

[13] S. Wanajo, H.-T. Janka, and S. Kubono, Uncertainties in the νp-process: Supernova Dynamics Versus Nuclear Physics, The Astrophysical Journal **729**, 46 (2011), `1004.4487`.

[14] D. N. F. Dunbar, R. E. Pixley, W. A. Wenzel, and W. Whaling, The 7.68-MeV state in C^{12}, Phys. Rev. **92**, 649 (1953).

[15] F. Hoyle, On Nuclear Reactions Occuring in Very Hot Stars. 1. The Synthesis of Elements from Carbon to Nickel, Astrophys. J. Suppl. **1**, 121 (1954).

[16] S. G., Who discovered the Hoyle level, Acta Polytechnica CTU Proceedings **2**, 311–320 (2015).

[17] H. A. Bethe, Energy production in stars, Phys. Rev. **55**, 434 (1939).

[18] E. M. Burbidge, G. R. Burbidge, W. A. Fowler, and F. Hoyle, Synthesis of the elements in stars, Rev. Mod. Phys. **29**, 547 (1957).

[19] L. E. Beghian, H. H. Halban, T. Husain, and L. G. Sanders, Energy levels of C^{12} from the $Be^9(\alpha, n)C^{12}$ reaction, Phys. Rev. **90**, 1129 (1953).

[20] J. H. Fregeau and R. Hofstadter, High-energy electron scattering and nuclear structure determinations. iii. carbon-12 nucleus, Phys. Rev. **99**, 1503 (1955).

[21] C. H. Millar and A. G. W. Cameron, Photo-alpha reactions in nuclear emulsions, Canadian Journal of Physics **31**, 723 (1953), `https://doi.org/10.1139/p53-068`.

[22] C. Iliadis, *Nuclear Physics of Stars* (John Wiley & Sons, Ltd 2015).

[23] K. Nomoto, F. K. Thielemann, and S. Miyaji, The triple alpha reaction at low temperatures in accreting white dwarfs and neutron stars, aap **149**, 239 (1985).

[24] D. E. Alburger, Gamma-ray decay of the 7.66-MeV level of C^{12}, Phys. Rev. **124**, 193 (1961).

[25] P. Seeger and R. Kavanagh, Electromagnetic decay of the second excited state of C^{12}, Nuclear Physics **46**, 577 (1963).

[26] I. Hall and N. Tanner, The radiative decay of the 7.66 MeV level of C^{12}, Nuclear Physics **53**, 673 (1964).

[27] D. Chamberlin, D. Bodansky, W. W. Jacobs, and D. L. Oberg, Electromagnetic decay of the 7.65-MeV state of ^{12}C, Phys. Rev. C **9**, 69 (1974).

[28] C. N. Davids, R. C. Pardo, and A. W. Obst, Radiative deexcitation of the 7.655-MeV state of ^{12}C, Phys. Rev. C **11**, 2063 (1975).

[29] H. B. Mak, H. C. Evans, G. T. Ewan, A. B. McDonald, and T. K. Alexander, Radiative decay of the second excited state of ^{12}C, Phys. Rev. C **12**, 1158 (1975).

[30] R. Markham, S. M. Austin, and M. Shahabuddin, A measurement of $\Gamma_{\mathrm{rad}}/\Gamma$ for the 7.654 MeV state of ^{12}C and the rate of the stellar 3α reaction, Nuclear Physics A **270**, 489 (1976).

[31] A. W. Obst and W. J. Braithwaite, Measurement of the radiative branching ratio for the 7.65-MeV state in ^{12}C using the cascade gamma decays, Phys. Rev. C **13**, 2033 (1976).

[32] A. W. Obst, T. B. Grandy, and J. L. Weil, Reaction $^{9}\mathrm{Be}(\alpha, n)^{12}\mathrm{C}$ from 1.7 to 6.4 MeV, Phys. Rev. C **5**, 738 (1972).

[33] R. Robertson, R. Warner, and S. M. Austin, Measurement of the internal pair emission branch of the 7.654-MeV state of C^{12}, and the rate of the stellar triple-α reaction, Physical Review C **15**, 1072 – 1079 (1977).

[34] D. E. Alburger, Pair decay of the 7.65-MeV level of C^{12}, Physical Review C **16**, 2394 – 2400 (1977).

[35] H. L. Crannell and T. A. Griffy, Determination of radiative transition widths of excited states in C^{12}, Phys. Rev. **136**, B1580 (1964).

[36] F. Gudden and P. Strehl, Anregung des 7.66 MeV-niveaus in kohlenstoff-12 durch unelastische elektronenstreuung, Zeitschrift für Physik **185**, 111 – 122 (1965).

[37] H. Crannell, T. Griffy, L. Suelzle, and M. Yearian, A determination of the transition widths of some excited states in ^{12}C, Nuclear Physics A **90**, 152 (1967).

[38] P. Strehl, Study of 0^+–0^+ transitions in ^{12}C, ^{24}Mg, ^{28}Si, ^{32}S and ^{40}Ca by inelastic electron scattering, Zeitschrift für Physik **234**, 416 – 442 (1970).

[39] M. Chernykh, H. Feldmeier, T. Neff, P. von Neumann-Cosel, and A. Richter, Pair decay width of the Hoyle state and its role for stellar carbon production, Phys. Rev. Lett. **105**, 022501 (2010).

[40] T. K. Eriksen, T. Kibédi, M. W. Reed, A. E. Stuchbery, K. J. Cook, A. Akber, B. Alshahrani, A. A. Avaa, K. Banerjee, A. C. Berriman, L. T. Bezzina, L. Bignell, J. Buete, I. P. Carter, B. J. Coombes, J. T. H. Dowie, M. Dasgupta, L. J. Evitts, A. B. Garnsworthy, M. S. M. Gerathy, T. J. Gray, D. J. Hinde, T. H. Hoang, S. S. Hota, E. Ideguchi, P. Jones, G. J. Lane, B. P. McCormick, A. J. Mitchell, N. Palalani, T. Palazzo, M. Ripper, E. C. Simpson, J. Smallcombe, B. M. A. Swinton-Bland, T. Tanaka, T. G. Tornyi, and M. O. de Vries, Improved precision on the experimental E0 decay branching ratio of the Hoyle state, Phys. Rev. C **102**, 024320 (2020).

[41] J. Dueñas, D. Mengoni, V. Parkar, R. Berjillos, M. Assie, D. Beaumel, A. Sánchez-Benítez, and I. Martel, Identification of light particles by means of pulse shape analysis with silicon detector at low energy, Nuclear Instruments and Methods in Physics Research Section A: Accelerators, Spectrometers, Detectors and Associated Equipment **676**, 70 (2012).

[42] M. Assié, B. L. Crom, B. Genolini, M. Chabot, D. Mengoni, J. A. Dueñas, S. Ancelin, D. Beaumel, Y. Blumenfeld, N. de Séréville, J.-J. Dormard, T. Faul, J. Guillot, A. Jallat, V. L. Ven, I. Martel, E. Rauly, D. Suzuki, and A.-S. Torrento, Characterization of light particles (z $\leq$ 2) discrimination performances by pulse shape analysis techniques with high-granularity silicon detector, The European Physical Journal A **51**, Article 11 (2015).

[43] G. Pastore, D. Gruyer, P. Ottanelli, N. Le Neindre, G. Pasquali, R. Alba, S. Barlini, M. Bini, E. Bonnet, B. Borderie, R. Bougault, M. Bruno, G. Casini, A. Chbihi, D. Dell'Aquila, J. Dueñas, D. Fabris, L. Francalanza, J. Frankland, F. Gramegna, M. Henri, A. Kordyasz, T. Kozik, I. Lombardo, O. Lopez, L. Morelli, A. Olmi, M. Pârlog, S. Piantelli, G. Poggi, D. Santonocito, A. Stefanini, S. Valdré, G. Verde, E. Vient, and M. Vigilante, Isotopic identification using pulse shape analysis of current signals from silicon detectors: Recent results from the FAZIA collaboration, Nuclear Instruments and Methods in Physics Research Section A: Accelerators, Spectrometers, Detectors and Associated Equipment **860**, 42 (2017).

[44] J. Flores, I. Martel, R. Jiménez, J. Galán, and P. Salmerón, Application of neural networks to digital pulse shape analysis for an array of silicon strip detectors, Nuclear Instruments and Methods in Physics Research Section A: Accelerators, Spectrometers, Detectors and Associated Equipment **830**, 287 (2016).

[45] Digital Filter Design Services, Digital filter design services, `http://dsp.jpn.org/dfdesign/fir/` (2024).

[46] IFIN-HH, Ifin-hh website, `https://www.nipne.ro` (2024).

[47] S. Aogaki, D. Balabanski, R. Borcea, P. Constantin, C. Costache, M. Cuciuc, A. Kuşoğlu, C. Mihai, R. Mihai, L. Stan, P.-A. Söderström, D. Testov, A. Turturică, S. Ujeniuc, S. Adachi, F. Camera, G. Ciocan, F. Crespi, N. Florea, Y. Fujikawa, T. Furuno, E. Gamba, R. Guţoiu, T. Kawabata, N. Mărginean, B. Million, C. Neacsu, D. Nichita, R. Niina, S. Okamoto, H. Pai, A. Pappalardo, K. Sakanashi, A. Tamii, C. Ur, and O. Wieland, A setup for high-energy γ-ray spectroscopy with the ELI-NP large-volume LaBr3:Ce and CeBr3 detectors at the 9 MV tandem accelerator at IFIN-HH, Nuclear Instruments and Methods in Physics Research Section A: Accelerators, Spectrometers, Detectors and Associated Equipment **1056**, 168628 (2023).

[48] Geant4 Collaboration, Geant4 Web Site (2024).

[49] M. Itoh, S. Ando, T. Aoki, H. Arikawa, S. Ezure, K. Harada, T. Hayamizu, T. Inoue, T. Ishikawa, K. Kato, H. Kawamura,

Y. Sakemi, and A. Uchiyama, Further improvement of the upper limit on the direct 3α decay from the Hoyle state in ^{12}C, Phys. Rev. Lett. **113**, 102501 (2014).

[50] R. Smith, M. Gai, M. W. Ahmed, M. Freer, H. O. U. Fynbo, D. Schweitzer, and S. R. Stern, Stringent upper limit on the direct 3α decay of the Hoyle state in ^{12}C, Phys. Rev. C **101**, 021302 (2020).

[51] J. Bishop, G. V. Rogachev, S. Ahn, E. Aboud, M. Barbui, A. Bosh, C. Hunt, H. Jayatissa, E. Koshchiy, R. Malecek, S. T. Marley, E. C. Pollacco, C. D. Pruitt, B. T. Roeder, A. Saastamoinen, L. G. Sobotka, and S. Upadhyayula, Almost medium-free measurement of the Hoyle state direct-decay component with a TPC, Phys. Rev. C **102**, 041303 (2020).

[52] Y. Fujikawa, T. Kawabata, S. Adachi, S. Enyo, T. Furuno, Y. Hijikata, K. Himi, K. Hirose, Y. Honda, K. Inaba, H. Makii, K. Miyamoto, M. Murata, K. Nishio, S. Okamoto, R. Orlandi, K. Sakanashi, F. Suzaki, S. Tsuji, K. Yahiro, and J. Zenihiro, Search for the 6α condensed state in ^{24}Mg using the ^{12}C+^{12}C scattering, Physics Letters B **848**, 138384 (2024).

[53] National Nuclear Data Center, National nuclear data center web site (2024).

[54] LISE++ Development Team, Lise++ website, `https://lise.frib.msu.edu/lise.html` (2024).

[55] National Institute of Standards and Technology (NIST), NIST Standard Reference Database (SRD), `https://www.nist.gov/srd` (2024).

[56] M. M. Hasan, T. Vidmar, J. Rutten, L. Verheyen, J. Camps, and M. Huysmans, Optimization and validation of a LaBr3(Ce) detector model for use in monte carlo simulations, Applied Radiation and Isotopes **174**, 109790 (2021).

[57] E. Picado, M. Carmona-Gallardo, J. Cal-González, L. Fraile, H. Mach, J. Udías, and V. Vedia, Efficiency measurement and monte carlo simulations of a CeBr3 scintillator, Applied Radiation and Isotopes **120**, 71 (2017).

[58] T. K. Eriksen, Investigation of the Hoyle state in ^{12}C and the related triple alpha reaction rate, PhD thesis, Australian National University (2018).

[59] V. Efimov, Energy levels arising from resonant two-body forces in a three-body system, Physics Letters B **33**, 563 (1970).

[60] *User Manual UM5960: CoMPASS - Multiparametric DAQ Software for Physics Applications*, Rev. 18 edition (2022), accessed: 2024-01-08.